

# **X-ray diffraction based characterization of ageing behaviour of precipitation hardenable steels**

*by*

**S. MAHADEVAN**

**(Enrolment No: ENGG02200804019)**

**Indira Gandhi Centre for Atomic Research, Kalpakkam**

*A thesis submitted to the*

*Board of Studies in Engineering Sciences*

*In partial fulfillment of requirements*

*for the Degree of*

**DOCTOR OF PHILOSOPHY**

*of*

**HOMI BHABHA NATIONAL INSTITUTE**



**August, 2015**




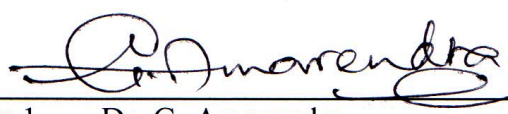
# Homi Bhabha National Institute


## Recommendations of the Viva Voce Committee


As members of the Viva Voce Board, we certify that we have read the dissertation prepared by **S. Mahadevan** entitled “**X-ray diffraction based characterization of ageing behaviour of precipitation hardenable steels**” and recommend that it may be accepted as fulfilling the thesis requirement for the award of Degree of Doctor of Philosophy.

  
Chairman – Dr. A. K. Bhaduri  
Date: 12/4/2016

  
Guide/Convener – Dr. T. Jayakumar  
Date: 12 April 2016

  
Member 1 – Dr. G. Amarendra  
Date: April 12, 2016

  
Member 2 – Dr. B. P. C. Rao  
Date: 12/4/2016

  
External Examiner  
Date: April 12, 2016

Final approval and acceptance of this dissertation is contingent upon the candidate's submission of the final copies of the dissertation to HBNI.

Date:

Place: Kalpakkam

## CERTIFICATE

I hereby certify that I have read this dissertation prepared under my direction and recommend that it may be accepted as fulfilling the dissertation requirement.



**(T. Jayakumar)**

Date: 12 April 2016

Place: Kalpakkam

## STATEMENT BY AUTHOR

This dissertation has been submitted in partial fulfillment of requirements for an advanced degree at Homi Bhabha National Institute (HBNI) and is deposited in the Library to be made available to borrowers under rules of the HBNI.

Brief quotations from this dissertation are allowable without special permission, provided that accurate acknowledgement of the source is made. Requests for permission for extended quotation from or reproduction of this manuscript in whole or in part may be granted by the Competent Authority of HBNI when in his or her judgment the proposed use of the material is in the interests of scholarship. In all other instances, however, permission must be obtained from the author.

Date: 12.4.16

Place: Kalpakkam



(S. Mahadevan)

## DECLARATION

I, hereby declare that the investigation presented in the thesis entitled “**X-ray diffraction based characterization of ageing behaviour of precipitation hardenable steels**” submitted to **Homi Bhabha National Institute (HBNI)**, Mumbai, India, for the award of **Doctor of Philosophy in Engineering Sciences** is the record of work carried out by me under the guidance of **Dr. T. Jayakumar**, Visiting Professor, Metallurgical and Materials Engineering Department, National Institute of Technology, Warangal-506004 and former Director, Metallurgy and Materials Group, Indira Gandhi Centre for Atomic Research, Kalpakkam-603102. The work is original and has not been submitted earlier as a whole or in part for a degree/diploma at this or any other Institution / University.

Date: 12.4.16

Place: Kalpakkam



(S. Mahadevan)

## List of publications arising from the thesis

### Journals

#### *Published*

- 1) Precipitation induced changes in microstrain and its relation with hardness and tempering parameter in 17-4 PH stainless steel  
**S. Mahadevan**, R. Manojkumar, T. Jayakumar, C.R. Das and B.P.C. Rao  
*Metallurgical and Materials Transactions A*, 47A, (2016) DOI:10.1007/s11661-016-3440-8
- 2) Size distribution of magnetic iron oxide nanoparticles using Warren-Averbach XRD analysis  
**S. Mahadevan**, S. P. Behera, G. Gnanaprakash, T. Jayakumar, J. Philip and B.P.C. Rao  
*Journal of Physics and Chemistry of Solids*, 73 (2012) 867-872.  
<http://dx.doi.org/10.1016/j.jpcs.2012.02.017>
- 3) X-ray diffraction profile analysis for characterizing isothermal aging behavior of M250 grade Maraging steel  
**S. Mahadevan**, T. Jayakumar, B.P.C. Rao, Anish Kumar, K.V. Rajkumar and Baldev Raj  
*Metallurgical and Materials Transactions A*, 39A, (2008) pp. 1978-1984.

#### *Communicated*

- 1) An approach based on microstrain, crystallite size, precipitate fraction and precipitate radius for understanding the strengthening of 17-4 PH steel  
**S. Mahadevan**, T. Jayakumar, B.P.C. Rao  
Under review with *Metallurgical and Materials Transactions A*
- 2) Comparison of different XRD peak profile analysis methods to study the ageing behaviour of 17-4 PH stainless steel  
R. Manojkumar, **S. Mahadevan**, B.P.C. Rao and T. Jayakumar  
Under review with *Z. Kristallogr.*

#### *Under preparation*

- 1) Strengthening mechanisms in M250 grade maraging steel studied from X-ray profile analysis  
S. Mahadevan, T. Jayakumar, B.P.C. Rao  
To be submitted

## Conference Presentations

- 1) A comparative study of broadening observed in aged 17-4 PH steel by modified Williamson Hall approach and Stephen's model  
R. Manojkumar, S. Mahadevan, B. P. C. Rao and T. Jayakumar  
1st International Conference on Scattering & Diffraction Technique for Material Characterization (ICSDTMC2013) NIT, Rourkela, Orissa-769008, 13-15 December, 2013.
- 2) Modified Williamson-Hall approach for characterizing ageing behaviour of 17-4 PH Stainless Steel  
S. Mahadevan, R. Manojkumar, B.P.C. Rao & T. Jayakumar  
24th AGM of Materials Research Society of India – MRSI-2013, Kalpakkam, Feb 11-13, 2013.
- 3) XRD profile analysis for characterization of cobalt ferrite nanoparticles  
S. Mahadevan, S. Ayyappan, John Philip, B.P.C. Rao and T. Jayakumar  
National Conference on Recent advances in Magnetic Materials and Applications - 2010 at Thiagarajar College of Engineering, Madurai during 20th-21st January 2010-.p9



*Solely dedicated to my beloved parents and family*



## **ACKNOWLEDGEMENTS**

I owe my deep sense of gratitude to my research supervisor and mentor **Dr. T. Jayakumar**, Visiting Professor, National Institute of Technology, Warangal-506004 and former Director, Metallurgy and Materials Group (MMG), Indira Gandhi Centre for Atomic Research (IGCAR) for his guidance, encouragement, whole hearted support and patience during the research work. The valuable discussions we had and the inspiration he provided brought the thesis to the level it has reached. I admire and thank him for critically and promptly going through the draft of my thesis and research papers every time during the past.

I express my sincere gratitude to **Dr. B. P. C. Rao**, Head, Non Destructive Evaluation Division (NDED), MMG, IGCAR and member of my Doctoral Committee for his whole hearted support and guidance. The suggestions and the timely reminders provided by him made this thesis possible in the allotted time. My sincere thanks are due to my Doctoral Committee Chairman **Dr. A. K. Bhaduri**, and member **Dr. G. Amarendra** for regularly evaluating the progress of the research work and giving many useful suggestions.

I am grateful to former Director of IGCAR, **Dr. Baldev Raj** for initiating me in to this work. I also thank former Director of IGCAR, **Shri. S. C. Chetal** and present Director, **Dr. P. R. Vasudeva Rao** for providing me the encouragement to pursue this work.

I would like to extend my heartfelt thanks to **Dr. K. V. Rajkumar** for sharing the M250 grade maraging steel samples for this work. The time he spent in going through a few of the chapters and his useful suggestions has helped in improving the clarity. I would like to acknowledge the contributions of **Dr. C. R. Das**, MTD in acquiring the SEM images. The motivation he provided during the work and the useful discussions we had during the preparation of the manuscript has been very important. Similarly, the contributions and help rendered by **Ms. Aarthi Ganesan** in acquiring the XRD spectra of 17-4 PH samples during her project work at IGCAR is gratefully remembered and the documentation she carried out is acknowledged. My colleague, **Shri. Manoj Kumar Raja's** contribution in carrying out some of the profile refinements is worth mentioning. **Shri. Arun Kumar** is remembered for all the small contributions he has made.

I would like to thank **Shri. B. V. Naidu** for the time he has spent in maintaining the diffractometer without which this work would not be possible. The backup facilities he provided made me comfortable. His team members, **C. Karunanidhi, T. Krishnan** and the entire *operation team at RML* provided all the facilities to run the diffractometer without a hitch.

I take this opportunity to thank **Dr. Govind Kumar Sharma** from the bottom of my heart for providing me all the necessary help in a timely and friendly way during the work. I would like to thank **Dr. S. Thirunavukkarasu** for critically going through few chapters of the thesis and for his useful suggestions. I would like to remember my friend and critic **Shri. S. Shyam Sundar**, RRCAT, who with his questions made me think further.

Finally, I would like to thank **Dr. Sanjay Rai**, RRCAT for the training he provided me in diffraction, **Shri. S. P. Behera**, BARC for his contributions during the implementation of Warren Averbach approach. Similarly, thanks are due to **SIRD**, especially, **Shri. A. Rangarajan** for all his help in getting some of the references, **Dr. K. Laha, Dr. Anish Kumar, Dr. C. Ravishankar, Dr. G. Raghavan, faculty of HBNI, Shri. Kalyan Phani, Shri. C. N. Venkiteswaran, Smt. Indira Logu, Smt. Revathi Anbuselvam, colleagues of NDED, class mates during the course work and bus mates** for all their little contributions during the thesis work.

I remember my late father **Shri. M. Sailam**, who wished me to do the thesis work long back and my mother **Smt. S. Gomathi** for her patience and prayers. Finally, I express my sincere and heartfelt thanks and appreciation to my wife **Anandhi** for her love, commitment and the sacrifices she made to make this achievement a reality. It is also my duty to put on record the love and affection shown by my daughter **Manjushri** and son **Gautam**. They understood my needs during the last year and motivated me wholeheartedly at home and spared me from their requirements during the thesis.

Above all, the grace of **Almighty** who granted me the wisdom, health and strength to undertake and complete this research work is acknowledged.

# **CONTENTS**

<b>CONTENTS</b>	<b>1</b>
<b>ABSTRACT</b>	<b>I</b>
<b>LIST OF FIGURES</b>	<b>III</b>
<b>LIST OF TABLES</b>	<b>VI</b>
<b>SYMBOLS</b>	<b>VII</b>
<b>ABBREVIATIONS</b>	<b>VIII</b>
<b>1 INTRODUCTION</b>	<b>1</b>
<b>1.1 X-ray diffraction line profile analysis</b>	<b>2</b>
<b>1.2 Influence of microstructural features on profile broadening</b>	<b>3</b>
<b>1.3 Developments in analyzing profile broadening</b>	<b>5</b>
<b>1.4 Changes in lattice parameter – implications</b>	<b>7</b>
<b>1.5 Precipitation hardenable steels</b>	<b>10</b>
1.5.1 Studies on precipitation hardenable 17-4 PH steel	10
1.5.2 Studies on M250 grade maraging steel	12
<b>1.6 XRD/LPA to study ageing behaviour</b>	<b>14</b>
<b>1.7 Motivation and objectives of the thesis</b>	<b>15</b>
<b>2 LITERATURE SURVEY</b>	<b>20</b>
<b>2.1 Preamble</b>	<b>20</b>
<b>2.2 Basics of X-ray diffraction</b>	<b>20</b>

<b>2.3</b>	<b>Factors influencing profile broadening</b>	<b>21</b>
<b>2.4</b>	<b>Profile functions in X-ray diffraction profile analysis</b>	<b>23</b>
<b>2.5</b>	<b>Metrics in profile fitting</b>	<b>25</b>
<b>2.6</b>	<b>Microstructural causes of profile broadening</b>	<b>27</b>
2.6.1	Crystallite size	27
2.6.2	Microstrain	28
<b>2.7</b>	<b>Approaches in separating the size-strain effects</b>	<b>30</b>
2.7.1	Williamson-Hall approach	30
2.7.2	Warren-Averbach method	31
2.7.3	Other approaches	34
<b>2.8</b>	<b>Modified approaches for separating the size-strain effects</b>	<b>35</b>
2.8.1	Modified Williamson-Hall (mWH) approach	36
2.8.2	Modified Warren-Averbach (mWA) method	37
<b>2.9</b>	<b>Application of XRDLP in materials</b>	<b>38</b>
2.9.1	Studies using WH and WA approaches	38
2.9.2	Studies using modified WH and WA approaches	39
2.9.3	Implications	41
<b>3</b>	<b>EXPERIMENTAL METHODS</b>	<b>42</b>
<b>3.1</b>	<b>Sample details</b>	<b>42</b>
3.1.1	17-4 PH steel	42
3.1.2	M250 grade maraging steel	43
<b>3.2</b>	<b>Hardness measurements</b>	<b>43</b>

<b>3.3 X-ray diffraction measurements</b>	<b>44</b>
3.3.1 Details of diffractometer	44
3.3.2 Experimental conditions used for XRD data acquisition	44
3.3.3 Analysis of diffraction data	44
<b>3.4 SEM investigations</b>	<b>45</b>
<b>4 STUDIES ON AGEING BEHAVIOUR OF 17-4 PH STEEL</b>	<b>46</b>
<b>4.1 Hardness changes on ageing</b>	<b>46</b>
4.1.1 Precipitation kinetics in the age hardening regime	47
4.1.2 Precipitation kinetics in the overaged regime	49
4.1.3 Variation of hardness with tempering parameter	50
<b>4.2 XRD analysis and SEM investigations</b>	<b>52</b>
4.2.1 Size-strain analysis in 17-4 PH steel	53
4.2.1.1 Ageing for 0.5 h	55
4.2.1.2 Ageing for 1 h	57
4.2.1.3 Ageing for 3 h	61
4.2.2 Influence of coherency strain on hardness	61
4.2.3 Variation of microstrain with tempering parameter	63
<b>4.3 Determination of precipitate fraction</b>	<b>64</b>
4.3.1 From changes in lattice parameter	64
4.3.2 From hardness measurements	68
4.3.3 Comparison of precipitate fractions	69

<b>4.4</b>	<b>Precipitation strengthening of 17-4 PH steel</b>	<b>71</b>
4.4.1	Strengthening in Fe-Cu alloys	71
4.4.2	Strengthening studies in other alloys	72
4.4.3	Strengthening mechanisms	73
4.4.3.1	<i>Coherency strengthening</i>	73
4.4.3.2	<i>Modulus strengthening</i>	74
<b>4.5</b>	<b>Estimation of radius of precipitates</b>	<b>74</b>
<b>4.6</b>	<b>Estimation of strengthening contributions</b>	<b>76</b>
4.6.1	Discussions on the estimated constants	81
<b>4.7</b>	<b>Summary</b>	<b>83</b>
<b>5</b>	<b>AGEING BEHAVIOUR OF M250 GRADE MARAGING STEEL</b>	<b>85</b>
<b>5.1</b>	<b>Precipitation kinetics from hardness</b>	<b>85</b>
<b>5.2</b>	<b>XRD studies in maraging steel</b>	<b>86</b>
5.2.1	Modified WH approach	88
5.2.1.1	<i>Changes in microstrain on ageing</i>	89
5.2.1.2	<i>Microstrain for precipitation kinetics</i>	90
5.2.1.3	<i>Crystallite size changes on ageing</i>	91
5.2.2	Modified WA analysis	92
5.2.2.1	<i>Dislocation parameters derived from mWA analysis</i>	93
5.2.2.2	<i>Mean square strain as a function of column length</i>	97
5.2.3	Comparison of the strain estimated by mWH and mWA methods	98
5.2.4	Precipitation fraction from lattice changes	100
<b>5.3</b>	<b>Precipitate radius from activation energy</b>	<b>104</b>



<b>5.4</b>	<b>Strengthening in M250 grade maraging steel</b>	<b>107</b>
5.4.1	Order strengthening	108
5.4.2	Hardness and Yield strength	108
5.4.3	Estimation of strengthening contributions	109
5.4.4	Discussions on estimated constants	113
<b>5.5</b>	<b>Summary</b>	<b>115</b>
<b>6</b>	<b>CONCLUSIONS AND FUTURE SCOPE</b>	<b>117</b>
<b>6.1</b>	<b>Conclusions</b>	<b>117</b>
<b>6.2</b>	<b>Future scope</b>	<b>119</b>
	<b>REFERENCES</b>	<b>121</b>



## ABSTRACT

*This study is intended to demonstrate the applicability of using the parameters derived from analysis of X-ray diffraction (XRD) profiles for characterizing the ageing behaviour of two precipitate strengthened alloys, viz., 17-4 PH steel and M250 grade maraging steel. These two materials, under solutionized condition, are known to have high dislocation density. On ageing, hardness increases due to precipitation. While coherent precipitates increase the microstrain in the matrix, annihilation of dislocations reduces the microstrain.*

*The XRD peak profile broadens, when the crystallite size is small or when the material contains lattice defects. When the crystallite shape or strain is anisotropic, the broadening does not change linearly with diffraction angle. To account for the anisotropic strain broadening, Ungár and Borbély proposed a modified Williamson-Hall (mWH) plot and a modified Warren-Averbach (mWA) analysis, which are based on the contrast caused by dislocations to profile broadening. These two approaches are used for estimating the changes in microstrain and crystallite size variation due to precipitation and microstructural changes that occur during ageing of these two steels. An approach is proposed to determine the precipitate fraction from changes in lattice parameter by using the atomic volume occupied by each of the alloying elements. The precipitate fraction estimated by this approach is compared with that obtained from changes in hardness.*

*In 17-4 PH steel, the changes in crystallite size were found to be consistent with the microstructural investigations carried out with scanning electron microscope. The Avrami exponent and the activation energy for the precipitation process have been determined from hardness measurements and they are found to compare well with published literature. The changes in hardness in the overaged regime and microstrain in the incoherent regime have been uniquely linked with the tempering parameter which links*

*the temperature and duration of ageing. In maraging steel, the root mean square strain as a function of column length has been evaluated from modified WA analysis. The changes in microstrain at shorter column lengths are linked to dislocation annihilation behaviour. The similarity of the long range strain with the microstrain estimated from the modified WH approach shows the effect of precipitates.*

*The increase in strength on ageing of 17-4 PH steel has been attributed to the coherency strengthening arising from the Cu precipitates and the modulus strengthening arising due to the difference in shear modulus of the precipitates and that of the matrix. In maraging steel, the strengthening has been attributed to the order strengthening which arises due to the formation of  $\text{Ni}_3\text{Ti}$  during initial ageing. The various precipitate strengthening mechanisms are theoretically estimated from experimentally determined microstrain and precipitate fraction along with calculated precipitate radius. The measured hardness is uniquely linked and compared to the precipitate strengthening and grain boundary strengthening contributions using a new 3-dimensional planar equation.*

*The above proposed approach clearly shows that coherency strengthening, modulus strengthening and grain boundary strengthening act in tandem and result in improved strength of 17-4 PH steel. In maraging steel, in addition to coherency and modulus strengthening, order strengthening acts along with grain boundary strengthening to contribute to the observed increase in yield strength. The Hall-Petch constant determined from the planar fit is in agreement with literature. This study clearly shows that the parameters estimated from XRD profile analysis, like lattice parameter, microstrain, crystallite size and dislocation density can be used to understand the microstructural changes that occurs during ageing and enables in-depth understanding of the strengthening behaviour of these two precipitation hardenable steels.*

## LIST OF FIGURES

Fig. 1.1 Quality of the assumptions made to handle the size-strain contribution to broadening [22].....	7
Fig. 1.2 Change in lattice parameter of maraging steel due to precipitation of $\text{Ni}_3\text{Ti}$ , $\text{Ni}_3\text{Mo}$ and $\text{Fe}_2\text{Mo}$ [26] .....	9
Fig. 1.3 Variation of lattice parameter, microstrain and crystallite size with post heat treatment [33].....	15
Fig. 2.1. Typical representation of columns with 5 unit cells are shown in particles with different sizes and shapes .....	33
Fig. 2.2. (a) Williamson-Hall plot and (b) modified WH plot for Pb 15 wt% Bi alloy [20]. .....	40
Fig. 4.1. Variation of hardness with ageing temperature of 17-4 PH samples isochronally aged for durations of 0.5, 1 and 3 h .....	47
Fig. 4.2. Fit of the Avrami equation using normalized hardness <sup>3/2</sup> (the Avrami equation is conventionally fitted on a time scale in seconds, hence the legends show the ageing duration in h).....	48
Fig. 4.3. Variation of change in overaged hardness with ageing time .....	50
Fig. 4.4. Variation of hardness with tempering parameter.....	52
Fig. 4.5. X-ray diffractograms of 17-4PH samples aged for 0.5 h at 380 and 480 °C along with solution annealed sample.....	53
Fig. 4.6. (a) WH plot and (b) modified WH plot for the samples heat treated for 0.5 h at 380 and 480 °C (the axis in units of $\text{\AA}^{-1}$ ).....	54
Fig. 4.7. Variation of (a) normalized mean square strain and (b) crystallite size with temperature in isochronally aged samples of 17-4 PH SS for different durations of 0.5, 1 and 3 h. ....	55
Fig. 4.8. SEM images of samples aged for 1 h at different temperatures along with solution annealed sample.....	59
Fig. 4.9. Variation of Hardness with $\alpha^{3/2}$ .....	63
Fig. 4.10. Variation of mean square strain with tempering parameter.....	64
Fig. 4.11. Variation of lattice parameter of (a) Fe-Cu bcc alloys with Cu concentration and (b) Fe-Ni bcc alloys with Ni concentration based on ICDD data (The legends indicate the Powder diffraction file available from ICDD) .....	66
Fig. 4.12. Estimated precipitate fraction (from lattice parameter changes) as a function of ageing time at different temperatures .....	68

Fig. 4.13. Variation of precipitate fraction estimated from Hardness <sup>1.5</sup> with ageing duration at different temperatures .....	69
Fig. 4.14. Variation of hardness with coherency + modulus strengthening (precipitate fraction estimated from changes in lattice dimensions) .....	78
Fig. 4.15. Variation of hardness with coherency + modulus strengthening (precipitate fraction estimated from changes in hardness) .....	78
Fig. 4.16. Linking hardness with the strengthening mechanisms based on eqn. 4.7, x axis in (Pa) and y axis in ( $m^{-1/2}$ ) (precipitate fraction estimated from changes in lattice) .....	80
Fig. 4.17. Linking hardness with the strengthening mechanisms based on eqn. 4.7, x axis in (Pa) and y axis in ( $m^{-1/2}$ ) (precipitate fraction estimated from changes in hardness) .....	81
Fig. 4.18. The plan view of the iso-hardness contours corresponding to the strengthening from the precipitates and grain boundaries .....	82
Fig. 5.1 (a) Variation of hardness with ageing time (h) and b) Fraction of precipitates transformed with ageing time (s) (legends indicate the ageing time in h) .....	86
Fig. 5.2 XRD spectra of solution annealed M250 samples along with 0.25, 70 and 100 h aged samples .....	87
Fig. 5.3 (a) WH plot (b) modified WH plot for samples heat treated at 482 °C for 0.25, 10 and 100 h .....	88
Fig. 5.4 Variation of normalized mean square strain with ageing time .....	90
Fig. 5.5 Plot of $\ln A(L)$ vs. $K^2 \bar{C}$ of 1 h sample at L values of 10, 30, 50, 70 and 100 Å .....	93
Fig. 5.6 Variation of dislocation density and relative beta parameter [139] with ageing duration (SA indicates solution annealed condition) .....	95
Fig. 5.7 Variation of $\langle \epsilon^2(L) \rangle$ as a function of column length L a) for solutionized and 3 h aged sample b) 10 and 40 h aged sample .....	98
Fig. 5.8 Variation of strain estimated from $P_0$ based on modified WA analysis and normalized mean square strain $\alpha$ estimated from mWH analysis with ageing duration .....	100
Fig. 5.9 Variation of lattice parameter of Fe-Ti bcc alloys with Ti concentration (The legends indicate the Powder diffraction file available from ICDD) .....	101
Fig. 5.10 (a) Calculated variation of lattice parameter for different types ( $Ni_3Ti$ , $Ni_3Mo$ and $Fe_2Mo$ ) of precipitates (b) Measured variation of lattice parameter with ageing time .....	103

Fig. 5.11 Variation of precipitate fraction estimated from changes in lattice parameter (blue dots) and from hardness changes (black filled square) .....	104
Fig. 5.12 Variation of converted yield strength (from hardness) with coherency + modulus + order strengthening.....	111
Fig. 5.13 Variation of yield strength with precipitate strengthening and dislocation strengthening based on eqn. 5.7. x and z axis in (Pa), y axis in ( $\text{m}^{-1}$ ) .....	113
Fig. 5.14 Variation of observed vs. theoretical values of $\Delta\tau$ during ageing of Co-Ni-Cr superalloy, $\Delta$ (using 2.16) indicate order strengthening estimated based on eqn. 5.4 in p.108, while $\circ$ (using 2.16) indicate coherency strengthening estimated based on eqn. 4.4 in p.73 (Figure 9 of Chaturvedi et al. [155]).....	114

## LIST OF TABLES

Table 1.1 Effect of various sources of strain on XRD peaks [12]	5
Table 3.1 Chemical composition of 17-4 PH steel in wt. %	42
Table 3.2 Heat treatment details of 17-4 PH steel	43
Table 3.3 Chemical composition of M250 grade maraging steel (wt. %)	43
Table 4.1 Volume of major alloying elements present in 17-4 PH steel	67
Table 4.2 Precipitate fraction determined from the two approaches and their difference	70
Table 4.3 Estimated radius of precipitates, normalized mean square strain ( $\alpha$ ), crystallite size and Hardness at different ageing conditions	75
Table 5.1 Changes in crystallite size estimated from the intercept of mWH plot shown in Fig. 5.3 along with the correlation coefficient	92
Table 5.2 Variation of the various parameters determined from modified WA approach with ageing duration is shown below	94
Table 5.3 Estimated radius of precipitates and normalized mean square strain under different ageing conditions	106
Table 5.4 Values of hardness, converted yield strength and measured yield strength under different ageing conditions	109



## SYMBOLS

$2\theta$	diffraction angle
$\alpha$	normalized mean square strain (microstrain)
$\beta_{\text{fwhm}}$	Width of the XRD profile at half the maximum intensity
$\beta_{\text{I}}$	Integral width
$\delta$	lattice misfit
$\varepsilon$	misfit strain
$\varepsilon_{\text{max}}$	upper bound of microstrain
$\varepsilon_{\text{rms}}$	root mean square microstrain
$\langle \varepsilon_{\text{L}}^2 \rangle$	mean-square strain
$\eta$	Cauchy content of the pV function
$1-\eta$	Gaussian content of the pV function
$\lambda$	wavelength of X-ray
$\rho$	dislocation density
$a$	Lattice parameter
$b$	modulus of the Burgers vector
$d_{hkl}$	interplanar spacing of $(hkl)$ plane
$f$	precipitate fraction
$g, K$	Diffraction vector ( $2\sin\theta/\lambda$ )
$n$	Avrami exponent
$r$	radius of the precipitate
$t$	ageing time
$A(L)$	Fourier coefficient of XRD profile as a function of column length $L$
$A^{\text{S}}(L)$	size Fourier coefficient
$A^{\text{D}}(L)$	strain Fourier coefficient (or distortion coefficient)
$\bar{C}$	average contrast factor of dislocations
$D'$	atomic diffusion coefficient
$G$	Shear modulus
$H$	Hardness
$L_{\text{s}}$ or $L_{\text{area}}$	area weighted mean column length
$L_{\text{v}}$	volume weighted mean column length
$P$	Larson-Miller parameter or tempering parameter
$R$	critical precipitate radius
$R_{\text{e}}$	outer cut-off radius of dislocations
$R_{\text{wp}}$	measure of fit between observed and calculated profiles (eqn. 2.6)
$T$	Temperature
$V$	volume of a unit cell
$YS$	Yield Strength

## ABBREVIATIONS

<i>apb</i>	anti phase boundary
bcc	body centred cubic
fcc	face centred cubic
FWHM	full width at half maximum
mWA	modified Warren-Averbach
mWH	modified Williamson-Hall
pV	pseudo-Voigt
PH	Precipitation Hardened
PSF	Profile shape functions
SA	solution annealed
SEM	Scanning Electron Microscope
TEM	Transmission Electron Microscope
WA	Warren-Averbach
WH	Williamson-Hall
WPPM	Whole Profile Pattern Modelling
WPPF	Whole Profile Pattern Fitting
XRD	X-ray diffraction
XRDLPA	X-ray diffraction line profile analysis

# Chapter - 1

## 1 Introduction

The first X-ray diffraction (XRD) pattern recorded by Friedrich, Knipping and Max Von Laue from zinc blende in early 1912 showed the wave nature of X-rays. William Henry Bragg and his son William Lawrence Bragg explained the observed reflection of X-rays by crystals in a particular direction and proposed the Bragg's law in 1913 [1]. This law explained the direction of coherently scattered radiation from all the atoms arranged in a lattice, thus producing diffracted beams. They identified the structure of ZnS to be face centred cubic. In the following two years, they determined the structure of many crystals, notable among them being diamond. In 1916, Debye and Scherrer showed that powder samples also diffracted X-rays [2]. Since then, X-ray diffraction has been playing a critical role in materials research and development because many materials and minerals are not available in single crystal form. Although the technique is termed "powder diffraction", any polycrystalline specimen and powders may be studied using this technique. The following are the major applications of XRD technique:

- Crystal structure determination by estimation of unit cell metrics, i.e. size and shape of the unit cell of any crystalline material from peak positions and intensities.
- Qualitative identification of the phases present in a material using the peak position and intensities of a powder pattern, as a fingerprint of the phase.
- Quantitative analysis of the concentration of each phase present in a multiphase material.

- Determination of full orientation distribution functions that describe the crystalline orientation in polycrystalline materials.
- Assessment of surface residual stresses in components.
- Determination of microstructural features of a polycrystalline material like crystallite size, microstrain within crystallites and defect densities from XRD profile broadening.

## **1.1 X-ray diffraction line profile analysis**

In order to evaluate the above mentioned microstructural parameters, it is essential to obtain the XRD profile parameters like peak position, width and shape. The peak width of XRD profile is influenced by two important factors, namely the contributions from the instrument and from the specimen. The instrumental factor includes wavelength distribution and geometric aberration. The specimen factor arises from the microstructural features of the material. Hence, it is essential to deconvolute the specimen related profile from measured profile. The specimen-related profile is believed to be mainly a convolution of strain-related and size-related profiles. To separate the size and strain components, certain analytical profile functions are fitted to the observed profile within the structure refinement tools based on Rietveld method [3]. The whole-pattern least-squares fitting method developed by Rietveld was extended by Young et al. in 1977 for use with X-ray powder diffractometer data to refine structure parameters [4]. This approach is called the top-down approach [5] or Whole Profile Pattern Fitting (WPPF) [6] or line-profile decomposition [7]. This fitting approach yields the characteristics of the peaks, namely, peak position, full width at half maximum (FWHM), integral breadth and the Fourier coefficients of the profiles. The information thus obtained can be used to derive the microstructural features based on the relevant model of size-strain separation

which is appropriate to the system under study. The results can also be compared with results from different models available for size-strain separation and also with other analytical techniques.

Another approach is called the bottom-up approach [5] wherein XRD profiles are calculated based on microstructural features like crystallite size/shape and its distribution, and based on the various models of strain which depend on lattice defects. The calculated data is thus compared with experimental data and this is called as Whole Profile Pattern Modelling (WPPM) [6] or line-profile synthesis [7] or Multiple Whole Profile (MWP) fitting [8]. However the challenge in this method is to model the profiles using theory that is relevant to the system under study. The analysis of the XRD line profiles or peak profiles to obtain the microstructural parameters of the specimen by both the above approaches is generally known as XRD line profile analysis, and is well known as XRDLPA or as Diffraction peak profile analysis (DPPA).

## **1.2 Influence of microstructural features on profile broadening**

The XRD peak profile broadens when the particle size is small or when the material contains lattice defects. Broadening of XRD line profiles due to small crystallite size was first recognized by Scherrer (1918) [9]. However, the broadening of individual peaks in a powder pattern is produced by small domains diffracting incoherently with respect to one another and by strain within the domains. Strain broadening is due to the displacement of the atoms in the lattice from their ideal positions in the lattice. Strain can be from point defects, linear defects like dislocations, planar defects like stacking/twin faults and volume defects causing misfits between coherent precipitates and the matrix. The strain fields in each of the above cases decays differently with respect to the distance from the defect ( $r$ ) as a function of  $1/r^2$ , or  $1/r$  as in the case of point and line defects. Due to the reciprocity

of the Fourier space (diffraction pattern) with real space of the crystal, the diffraction/scattering effects of  $1/r^2$  dependent term would be observed far away from the Bragg reflections in diffracted pattern and this is called as Huang scattering. Similarly, linear defects cause long range strain fields and their diffraction effects cluster around the Bragg reflections and cause broadening. The strain fields of planar defects are homogeneous and space independent causing the peaks to shift. However, these defects are bound by partial dislocations leading to peak broadening and asymmetry. Volume defects when they are very small would be equivalent to point defects, but as they grow, would have misfit dislocations causing long range strain fields, leading to peak broadening, similar to that of dislocations [10].

The effect of volume misfit between finely dispersed misfitting inclusions and the matrix on the strain fields has been considered by Berkum et al. [11]. In this study, they assumed that all crystallites of the matrix are spherical and of uniform size with spherical shaped precipitate at the centre. They increased the radius of the precipitate to increase the volume fraction of the precipitates. This approach was applied to model the broadening of XRD peaks in AlSi alloys with different compositions of Si, ranging from 2 to 16 wt%. The strain fields that are existent in this alloy are due to the large difference in thermal expansion between Si precipitates and Al matrix. The deviation of the experimental profile with simulated profile at higher vol % of Si was attributed to the assumption of uniform size and shape of the inclusions, matrix crystallites and the misfit parameter. The above approach, to the best of the scholar's knowledge has not been applied to study any material system wherein initial precipitation is very fine and precipitate size changes rapidly. It is also known that precipitation occurs at dislocations or at grain boundaries most often than at the centre of the crystallites in the matrix.

Ungár [12] considered the effect of common sources of strain, on the aberrations they cause to XRD peak profiles in the form of peak shift, broadening, asymmetry, anisotropic peak broadening and peak shape. He had shown typical correlation between various aspects of the aberrations caused to XRD profiles and the sources of strain in a tabular form, as shown in Table 1.1. It is also clear from the table that dislocations and planar faults like stacking faults and twinning only cause anisotropic peak broadening in addition to small crystallites. Microstresses cause peak broadening and coherency strains may show some peak asymmetry in addition to broadening.

Table 1.1 Effect of various sources of strain on XRD peaks [12]

Sources of strain	Peak aberrations				
	Peak shift	Peak broadening	Peak asymmetry	Anisotropic peak broadening	Peak shape
Dislocations		+	+	+	+
Stacking faults	+	+	+	+	+
Twinning	+	+	+	+	+
Microstresses		+			
Long-range internal stresses	+		+		
Grain boundaries	+	+			
Sub-boundaries	+	+			
Internal stresses	+				
Coherency strains	+	+	+		
Chemical heterogeneities	+	+	+		
Point defects					+
Precipitates and inclusions			+		+
Crystallite smallness		+		+	+

### 1.3 Developments in analyzing profile broadening

From the deconvoluted specimen related profile, two procedures are widely used for separating the size and strain contributions to XRD profile broadening. The method proposed by Williamson - Hall in 1953 [13] is based on the width of the reflections and assumes that the size dependency is diffraction order independent and strain is order dependent. The second method proposed by Warren – Averbach in 1952 [14] is based on the Fourier-coefficient analysis of multiple orders of same reflection. Herein, the Fourier coefficients of the Bragg reflections are written as a product of size and distortion coefficients, which is diffraction order dependent. The size coefficients can, in principle,

give information on the column length distribution of the diffracting domains based on the column length model of Bertaut (1952) [15]. The distortion coefficients can be solved for determining the mean-square strain  $\langle \epsilon_L^2 \rangle$  as a function of column length.

In 1993, Balzar & Ledbetter [16] proposed the double-Voigt method wherein the Cauchy and Gauss contents of the individual peaks are used to separate the size and strain contributions to broadening. Further, analytical solutions to the Fourier size and strain coefficients have been determined and are used for estimating the surface and volume weighted column length distribution and size of the particles. However, this method depends on the accurate partitioning of Cauchy and Gauss contents of the XRD peak profiles.

The Williamson-Hall (WH) and Warren-Averbach (WA) procedures are valid, if the XRD profile broadening is isotropic in different directions of a crystal. When the crystallite shape or strain is anisotropic, the broadening doesn't change linearly with diffraction angle. To account for the anisotropic strain broadening, Ungár and Borbély [17] proposed a modified Williamson-Hall (mWH) plot and a modified Warren-Averbach (mWA) analysis by using the dislocation model, which is based on the mean square strain of the dislocated crystals. This model has been applied to solve the anisotropic line broadening observed in samples of copper grains deformed by equal channel angular pressing [17], nano crystalline copper formed by inert-gas condensation and hot compaction [18,19], and in cold-worked Pb-Bi alloys of different compositions [20]. In a review of integral breadth methods, Scardi et al. [21] concluded that these methods are beneficial to identify the changes in microstructural features in a series of analogously treated samples. Vermeulen and Delhez [22] made a systematic ranking of the various line profile analysis methods based on the basic assumptions in each of them and ranked the modified Williamson Hall plot and the modified Warren Averbach method better than other methods of analysis



when multiple reflections and anisotropic broadening are considered. The results of their analysis are shown in Fig. 1.1.

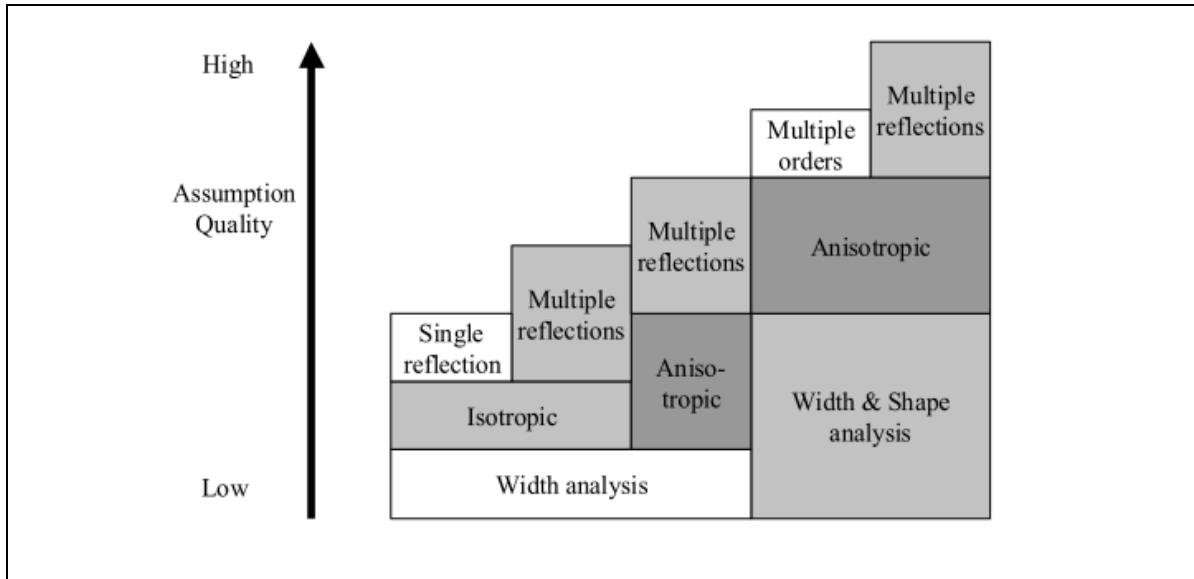


Fig. 1.1 Quality of the assumptions made to handle the size-strain contribution to broadening [22]

## 1.4 Changes in lattice parameter – implications

X-ray diffraction is a well known technique for estimating the lattice structure and lattice dimensions of alloys and compounds. The lattice dimensions depend on the size of the solute and solvent atoms which form the lattice. The size of the atom is either defined based on the distance of closest approach or based on the effective atomic volume of the solute atoms in the solid solution. The distance of closest approach can be estimated from the dimensions of the lattice in the direction of close packing. In fcc structure, the distance of closest approach of these elements is along  $\langle 110 \rangle$  direction and in bcc, it is along  $\langle 111 \rangle$  direction. Matching these length scales gives the lattice dimension of these materials in bcc structure as  $a_{bcc} = \sqrt{2/3} a_{fcc}$ . The size thus obtained is exactly equal to the Goldschmidt radius for fcc and is 3% less for bcc [23]. The atomic volume of an atom is defined as the volume of the unit cell divided by the number of atoms in the cell. In

metallic systems, effective atomic volume of the solute has been calculated by King for many substitutional solid solutions from lattice parameter measurements [24].

The capacity for forming solid solutions in metallic systems is dependent on the differences in the size of the constituent atoms. The atomic size is not a unique value, as it depends on the type of bonding and co-ordination in the particular crystal structure. Hume-Rothery [25] had analyzed the concept of favourable size factors for the formation of solid solutions. He predicted that if the diameter of the solvent and solute lie within a range of  $\pm 14\%$  as the favorable zone for forming solid solutions. It is to be noted that solid solutions may not form even if the elements lie within this size factor. In many binary alloy systems, the size factors have been used to determine the lattice dimensions.

Various elements in different weight percentages are melted together to form different alloys. In an alloy system with  $i$  alloying elements, the volume of a unit cell ( $V$ ) can be determined from

$$V = Z \sum_i \frac{x_i V_i}{100} \quad \text{-- ( 1.1 )}$$

where  $Z$  is the number of atoms per unit cell,  $x_i$  and  $V_i$  are the atom percentage and volume of the  $i^{th}$  element respectively. From the above equation, the volume of unit cell is estimated which can be used to estimate the lattice parameter of an alloy with many elements. However, the alloy under study crystallizes into a crystal structure depending on its stability at room temperature, despite presence of different elements which prefer to be in different crystal structures. When these alloys are aged to form precipitates, the matrix gets depleted of alloying elements, leading to changes in lattice dimension which could be used to quantify the precipitate fraction.

Guo et al. [26] used the volume occupied by different alloying elements based on the data available in literature. They used this data to estimate the changes in lattice parameter due

to precipitation of different intermetallics in maraging steel. Based on the data presented by Guo et al. [26], the changes in lattice parameter due to precipitation of  $\text{Ni}_3(\text{Ti},\text{Mo})$  and  $\text{Fe}_2\text{Mo}$  are shown in Fig. 1.2. Based on this formalism, the authors had estimated the precipitate fraction. However, in their approach, they had not taken into account the change in volume occupied by the element, which depends on the crystal structure (bcc or fcc) in which the element is present in the alloy. Among the major alloying elements present in the steels that are under study, Cu and Ni are normally stable in fcc structure. *In this study, it is proposed to use the crystal structure dependent size for theoretically estimating the precipitate fraction.*

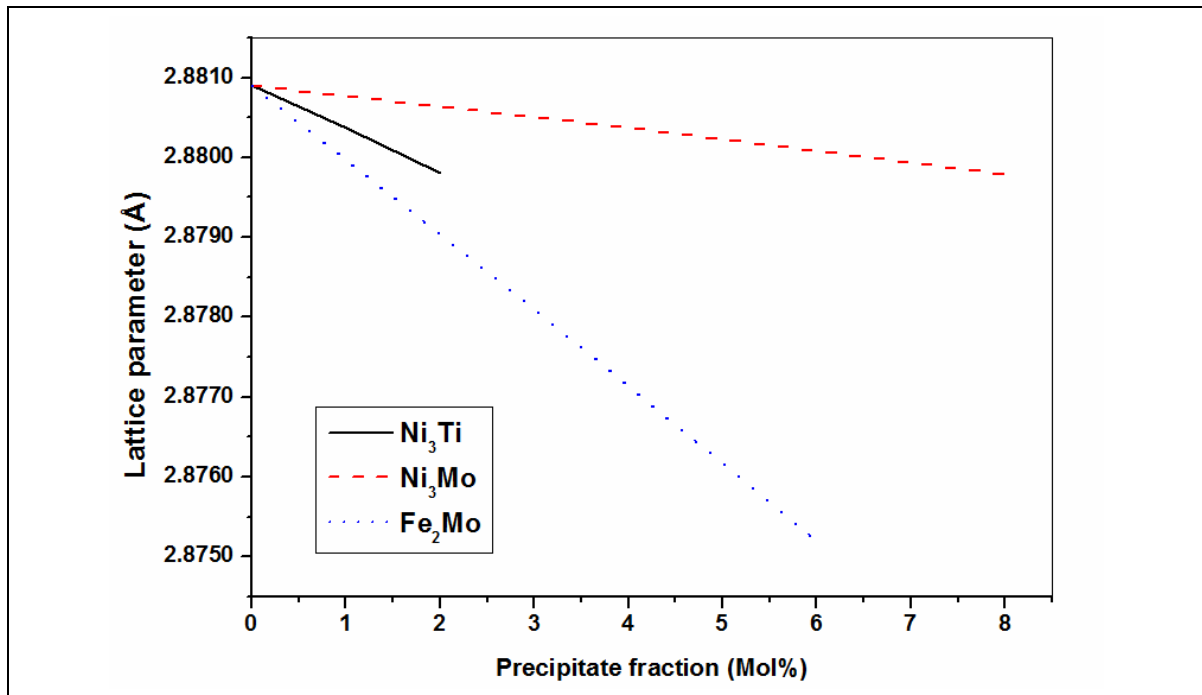


Fig. 1.2 Change in lattice parameter of maraging steel due to precipitation of  $\text{Ni}_3\text{Ti}$ ,  $\text{Ni}_3\text{Mo}$  and  $\text{Fe}_2\text{Mo}$  [26]

The following section would dwell on the two precipitation hardenable materials that would be studied in this thesis with emphasis on understanding the microstructural evolution during ageing of these two steels.

## **1.5 Precipitation hardenable steels**

Precipitation hardened steels are a class of steels wherein the steels gets strengthened on ageing for different durations at different temperatures due to formation of precipitates. The general principle of precipitation hardening is to produce super cooled solid solution from which, on ageing, compounds precipitate. These precipitates nucleate during early stages of ageing and grow in size leading to microstructural changes that result in an improvement of certain properties of these steels. Precipitation hardened stainless steels are widely used as structural materials in chemical and power plants because of their balanced combination of good mechanical properties and adequate corrosion resistance. The precipitation hardenable steels considered in this thesis are 17-4 PH stainless steel where Cu precipitates form and M250 grade maraging steel where intermetallic precipitates form on ageing at appropriate temperatures for sufficient duration. The effect of precipitation in these steels has been studied by evaluating the changes in hardness [27], resistivity [28,29], ultrasonic velocity measurements [30], differential scanning calorimetry [31], X-ray diffraction [32,33] and by dilation experiments [34].

### ***1.5.1 Studies on precipitation hardenable 17-4 PH steel***

The 17-4 PH (precipitation hardening) stainless steel, used for the present study is a martensitic stainless steel containing approximately 3-4 wt.% Cu and is strengthened by the precipitation of highly dispersed copper particles in the martensite matrix. 17-4 PH steel shows excellent wear resistance, corrosion resistance and mechanical properties. This steel is used in different heat treated conditions in nuclear, aerospace, naval and chemical industries where high strength, toughness and good fabrication characteristics are required. The good mechanical properties of this material are achieved by age hardening the solution annealed specimens. Optimum ageing time and temperature combinations are

employed to obtain maximum strength and hardness. However use of lower temperature for shorter time or higher temperature for longer time would respectively lead to under ageing or over ageing conditions with the associated reduction in strength and hardness. This material has been studied extensively by various authors using different material characterization techniques [27,35,36,37,38].

Viswanathan et al. [28] discussed the kinetics of precipitation in 17-4 PH stainless steel using changes in electrical resistivity and microstructures. In solution treated condition, the microstructure of the alloy is found to have parallel lath martensites having high dislocation density. On ageing the alloy at 395, 455 and 499 °C, the resistivity decreased drastically and reached a steady value on prolonged ageing. When the alloy was aged above 500 °C, the resistivity changed at a slower rate with a higher value of final resistivity on prolonged ageing, as compared to the lower temperature heat treatments. On ageing at 599 °C for 1 h, they found an interlath fcc precipitate with ribbon like morphology, in addition to the fine copper rich precipitates. This interlath precipitate was identified as austenite.

Murayama et al. [39] reported that the solution annealed specimen of 17-4 PH stainless steel consists of largely martensite with a small fraction of  $\delta$  ferrite. However, Hsiao et al. [35] found that on solution treatment, the steel produces a uniform matrix, which consists chiefly of lath martensite with micro-twins. A peak hardness (450 Hv) is reported at 480 °C after an hour of ageing and remains constant up to 10 hours of ageing. At 565 °C and 620 °C, the peak hardness attained is relatively lower and the peak hardness occurs at shorter durations. The transmission electron microscopy (TEM) investigations by the authors [35] on specimens aged at 620 °C for 4 h revealed Cu rich precipitates with an average particle size of 30 nm with fcc structure. In addition to the formation of copper rich precipitates, the formation of reversed austenite has also been noticed. The

phenomenon of reversed austenite is suggested to be related with the pre-existing copper particles. Miller and Burke [37] studied the microstructural features of 17-4 PH stainless steel with the help of atom probe field ion microscopy and TEM studies at various stages of heat treatment. By field ion microscopy, they could image precipitates in specimens aged for 0.5 h at 482 °C.

Wang et al. [38] showed that, when the steel is aged at 595 °C, the bulk hardness of the specimen attains its peak value (42.5 HRC) at about 20 min, and then decreases continuously on further ageing. Under peak hardness condition, the TEM studies revealed a microstructure with fine spheroid-shaped copper with fcc crystal structure and fiber-shaped secondary carbides  $M_{23}C_6$ . These precipitates were attributed as the reasons for strengthening of the alloy at this temperature. Bhattacharya et al. [36] studied the age hardening behavior in 17-4 PH steel by using magnetic Barkhausen emission (MBE) technique and inferred that MBE peak heights reduce in presence of copper precipitates on isochronal ageing for 1 hour at 475, 510, 575 and 620 °C and correlated well with hardness.

### ***1.5.2 Studies on M250 grade maraging steel***

M250 grade maraging steel, wherein the term “maraging” is derived from “martensite age hardening” and denotes age hardening of a low-carbon martensite matrix. Carbon, in fact, is an impurity in maraging steels and kept at the lowest possible concentration. The absence of carbon, and the use of intermetallic precipitation to achieve hardening produces several unique characteristics of maraging steels that set them apart from conventional steels. This class of steels has excellent mechanical properties i.e. ultra-high yield strength combined with good fracture toughness [40,41], is used in aircraft, aerospace and nuclear industries. The high strength to weight ratio, good

weldability, ease of machining in the solution annealed condition and dimensional stability during ageing make this material an ideal choice for critical rocket motor casing applications in aerospace industries.

Maraging steels are strengthened by the precipitation of intermetallic compounds at temperatures of about 480 °C. The ageing behaviour of various grades of maraging steels has been extensively studied by various authors [29,30,40,41]. The microstructure of Maraging steel is characterized by high density of dislocations in the solution annealed condition. It has been reported that, depending on the ageing conditions, the steel undergoes systematic microstructural changes. The reported studies revealed that strengthening of the steel occurs due to the combined presence of hexagonal  $\text{Ni}_3(\text{Ti},\text{Mo})$  and  $\text{Fe}_2\text{Mo}$  intermetallic precipitates. During initial ageing, formation of  $\text{Ni}_3\text{Ti}$  takes place rapidly due to fast diffusion of titanium atoms, followed by precipitation of  $\text{Fe}_2\text{Mo}$  phase, which is responsible for the peak strength and for maintaining high strength on prolonged ageing [42]. The intermediate ageing duration (e.g. ~10 to 40 hours at 755 K) is characterized by reversion of austenite accompanied by precipitation of hexagonal  $\text{Fe}_2\text{Mo}$  intermetallic phase along with  $\text{Ni}_3\text{Ti}$ . As precipitation of these intermetallic phases and reversion of austenite have opposite effects on hardening, the overall hardening achieved levels off after reaching a maximum in this regime [29]. The decrease in the hardness, observed at longer ageing durations has been attributed essentially to the formation of reverted austenite rather than due to coarsening of the intermetallic precipitates. The amount of reverted austenite has been reported to increase with increase in the ageing time and temperature [30].

Peters and Cupp [43] studied the precipitation hardening behaviour of this steel and established a correlation between variation of electrical resistivity and microhardness as a

function of ageing time and temperature. The variation of these properties was used to study the kinetics of precipitation by Vasudevan et al [29]. Similarly, kinetics of precipitation in various grades of maraging steel was investigated using differential scanning calorimetry [31], by carrying out hardness measurements in isothermally heat treated specimens [42] and from dilation data acquired during heating and cooling [34]. Sha [44] carried out quantification of age hardening from hardness data in maraging steels and Ni-base superalloys, which followed the classical growth and coarsening theories.

## **1.6 XRD/LPA to study ageing behaviour**

The studies on application of XRD technique to study ageing behaviour dates back to 1938 with the first observation by Preston [45] of two or three weak but sharp satellites in the oscillating crystal photographs of single crystal alloy of aged Aluminium alloy with 4 wt% copper. Around the same time, Guinier [46] observed streaking in X-ray small angle scattering experiments carried out on aged Aluminium alloys and he determined the size of the copper platelets to be in the range of 5-10 nm. This work was instrumental in coining the name GP (Guinier-Preston) zone, which is known to form during the early precipitation process. Kuhn et al. [47] were able to estimate small misfits  $<2 \times 10^{-3}$  that occurs between  $\gamma$  and  $\gamma'$  phases in nickel base alloys using XRD technique. Rai et al. [33] studied the microstructural evolution in Inconel 625 during ageing for large durations up to 500 h at 1123 K. The estimated microstrain and crystallite size from WH approach and lattice parameters are shown in Fig. 1.3. They were able to demonstrate that these three parameters could be used in a complementary way to study precipitation/dissolution of intermetallic precipitates in this alloy. The anisotropic broadening observed was not addressed by these authors.



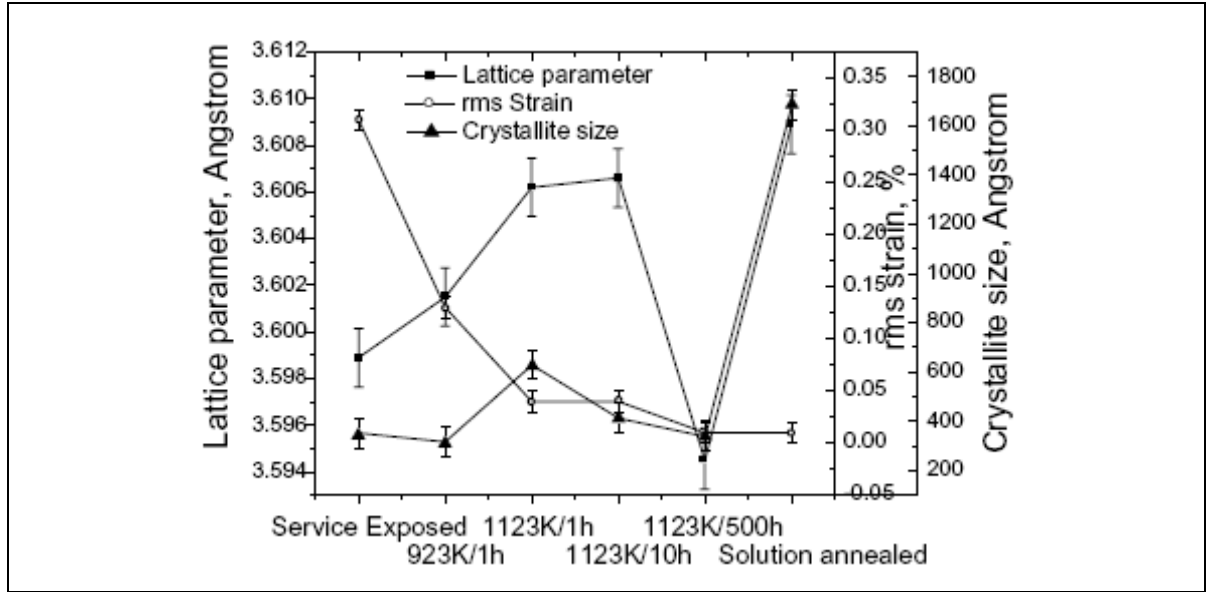


Fig. 1.3 Variation of lattice parameter, microstrain and crystallite size with post heat treatment [33].

Mahadevan et al. [32] had applied the modified WH approach for studying the ageing induced precipitation behaviour of M250 grade maraging steel. The estimated microstrain was used to determine the Avrami exponent of the precipitation process. The study revealed that the anisotropic broadening observed on ageing of this steel could be addressed using the dislocation contrast model. Assuming that the increase in mean square strain arises from precipitation, the kinetics of the precipitation process was also determined by Mahadevan et al. [32]. The application of the modified WH approach, which is based on contrast caused by dislocations has to be applied to other precipitation hardenable systems like 17-4 PH steel and validated. This is necessary since the strain field created by the precipitates which is a volume defect would be different from the strain fields of line defects like dislocations. The modified WA approach for determination of dislocation density was not carried out.

## 1.7 Motivation and objectives of the thesis

Based on the brief introduction presented, it is clear that a study of age hardening behaviour of two precipitation hardenable materials viz., 17-4 PH steel and M250 grade

maraging steel by XRD/LPA would provide an insight into the microstructural evolution. To summarize, these two materials are known to have high dislocation density under solutionized condition. Ageing of these steels results in coherent precipitation with simultaneous reduction in dislocation density due to annihilation of dislocations. On ageing, while annihilation of dislocations reduces microstrain, coherent precipitation of intermetallics in M250 grade maraging steel and Cu in 17-4 PH steel increases microstrain.

- In order to establish XRD profile analysis as a viable tool to characterize the ageing behaviour, it would be worthwhile to apply the parameters derived from XRD/LPA like normalized mean square strain and crystallite size to correlate with the microstructural evolution that takes place during ageing. *Hence, evaluating the changes in microstrain and crystallite size using XRD/LPA would provide an insight into these microstructural changes.*
- *To meet this objective it is essential to develop (in-house) profile analysis tools and implement the mWH and mWA approaches.* While, many WPPM tools are available in the open domain, a suitable model incorporating the microstructural changes during precipitation is not well tested in many metallic systems. Hence, *this thesis work is based on the top-down approach in combination with WPPF.*

Similarly, to evaluate the strengthening due to precipitation, a detailed knowledge of the evolution of precipitate fraction and size of precipitates is required. As the fraction of precipitates formed is small, it would be very difficult to estimate the fraction using conventional quantitative analysis by measuring the intensity of the XRD peaks from the precipitates.

- *Hence, fraction of precipitates formed needs to be evaluated from changes in hardness [43], from which the Avrami exponent can also be determined. As briefed in §1.4, the change in lattice parameter due to precipitation can be used to evaluate the precipitate fraction.*
- *The above approach of determining precipitate fraction is first validated in 17-4 PH stainless steel where Cu precipitates form during early ageing. This approach is also adapted to M250 grade maraging steel where different types of precipitates are known to form.*
- *Finally, the hardness measured at different ageing durations and temperatures need to be linked suitably. In cases where the physical phenomenon driving the kinetics is same, Larson-Miller or tempering parameter [48], which connects the time and temperature of ageing has been used. Hence, an attempt would be made to link hardness with tempering parameter.*

Determination of radius of precipitates especially in early stages requires atom probe or TEM investigations wherein the sampled volume is very small. To estimate the radius of precipitates, the activation energy of the precipitation process is required which can be evaluated from the changes in hardness.

- *Hence, the activation energy for the precipitation process determined from hardness measurements is used along with the diffusion coefficient to theoretically estimate the radius of precipitates. However, this approach of estimating radius of precipitates needs to be validated with well known theoretical models and experimental observations.*

The increase in hardness/strength achieved on ageing is due to the intrinsic strength of the matrix and due to the finely dispersed precipitates in the matrix. The intrinsic strength of

the matrix is due to intrinsic resistance offered by the lattice and to the strengthening effects of atoms that form the solid solution. This is the strength that is achieved in the solutionized condition. Among the two materials chosen, increase in strength of 17-4 PH steel occurs due to the precipitation of fine copper particles. The increase in strength on ageing of Fe-Cu alloys has been analysed in various studies, and attributed to different strengthening mechanisms, like coherency strengthening based on Gerold's model [49] and modulus strengthening arising from the difference in shear modulus of the precipitates with that of the matrix based on Kelly's theory [50] or based on Russel and Brown model [51]. For theoretically determining the various strengthening mechanisms discussed above, the microstrain, radius of precipitates and volume fraction of precipitates are the important variables required.

- *Hence it is proposed to use the microstrain and precipitate fraction estimated from XRD/LPA along with theoretically estimated precipitate radius for estimating the above mentioned strengthening mechanisms. Finally the calculated strength should be correlated with the mechanical property namely hardness.*

Similarly, in Maraging steel, the strength increase has been attributed to intermetallic precipitation of  $\text{Ni}_3\text{Ti}$  during initial ageing, followed by  $\text{Ni}_3\text{Mo}$ . On further ageing,  $\text{Fe}_2\text{Mo}$  precipitates form with simultaneous formation of austenite [32]. Herein, the strengthening has been attributed to the order strengthening which arises during the formation of  $\text{Ni}_3\text{Ti}$  during initial ageing.

- *The contribution of the order strengthening mechanism to hardening of M250 grade maraging steel is to be evaluated along with other strengthening mechanisms. Similar to 17-4 PH steel, the required variables to determine the strengthening are derived from XRD/LPA.*

During ageing, annihilation of dislocations causes substructural changes by modifying the grain size. The increase in strength due to grain size is well related by the Hall-Petch relation.

- *Finally, it is interesting to correlate the observed variation in hardness, by adding the contributions from various strengthening mechanisms along with the grain boundary strengthening in these two precipitation hardenable steels. The grain boundary strengthening is estimated from crystallite size derived from XRD/LPA. Hence, this attempt of correlating the hardness with strengthening mechanisms is unique as most of the parameters are derived from XRD/LPA.*

# Chapter - 2

## 2 Literature survey

### 2.1 Preamble

The introductory chapter provided a glimpse of the developments in the field of XRD/LPA and presented the need for this study. However, the mathematical approach and the basis of various size-strain separation methods were not presented. Hence, for the sake of completeness, this chapter starts by highlighting the basics of diffraction, causes of XRD profile broadening and introduces profile fitting. An exhaustive literature survey of the approaches available for separating the contributions of crystallite size and microstrain to XRD peak profile broadening is presented. The mathematical formalism of the approaches adapted in this thesis is presented in detail. The application of XRD/LPA thus far to study other microstructural changes (non-ageing induced) would be elucidated. These studies are presented to further highlight the importance of the objectives presented in §1.7.

### 2.2 Basics of X-ray diffraction

When X-rays interact with matter, they primarily interact with the electrons in the atoms. When the incident X-rays transfer some of their energy to the electrons, the scattered X-rays have different wavelength than the incident x-rays, which is known as inelastic scattering (Compton Scattering). However, some of the photons are deflected away from their original path much like billiard balls bouncing off one another. If these deflected photons are of the same energy as the incident photons (wavelength does not change), the process is known as elastic scattering (Thompson Scattering) wherein transfer of momentum takes place. When such scattering occurs from a periodic array of atoms, as in a lattice, each of these atoms scatters radiation coherently leading to concerted

constructive interference in specific angles and is called diffraction. Diffraction is essentially, reinforced coherent scattering.

The direction (angle between the incident and the diffracted rays, given as  $2\theta$ ) in which diffraction occurs is linked to the wavelength ( $\lambda$ ) and the interplanar spacing ( $d$ ) by the Bragg's law given by  $2d \sin \theta = n\lambda$  where  $n$  is an integer representing the order of the diffraction peak. Experimentally, the Bragg's law can be applied in two ways. By using X-rays of known wavelength  $\lambda$  and by measuring  $\theta$ , we can determine the spacing  $d$  of various planes in the crystal: which is structure analysis. Alternatively, we can use a crystal with planes of known spacing  $d$ , measure  $\theta$ , and thus determine the wavelength  $\lambda$  of the radiation used: which is X-ray spectroscopy.

A polycrystalline sample or bulk metal is composed of billions of tiny crystallites. When monochromatic X-ray beam interacts with a polycrystalline sample, enhanced intensity is observed at certain angles due to diffraction. During the measurement of the X-ray diffraction pattern, each  $d$ -value is represented by a reflection at the appropriate Bragg angle. This pattern, which is a graph with  $2\theta$  along x-axis and diffracted intensity along y-axis, is analyzed to reveal the nature of the lattice. The x-axis can be converted to  $d$  scale or  $d^* = 1/d = 2\sin\theta/\lambda$  scale such that the data becomes wavelength independent. The multiple peaks in a spectrum may be from a single phase or from multiple phases present in the sample under study. The analysis of peak location leads to an understanding of the crystal structure. However, the peaks obtained are not sharp and some broadening is observed due to various factors.

### **2.3 Factors influencing profile broadening**

The two important factors that influence the peak broadening are instrumental and specimen factors. The instrumental factor includes wavelength distribution and geometric

aberration. The specimen factor includes the defect i.e. crystallite size and microstrain present in the material. Any observed profile  $h(x)$  contains the contribution from instrumental factors  $g(x)$ , the specimen factors  $f(x)$  and the background acquired during the experiment. To obtain microstructural parameters of the specimen, the physically (specimen) broadened profile  $f(x)$  must be extracted from the observed profile  $h(x)$ . Thus, the observed line profile is a convolution of  $g(x)$  and  $f(x)$ :

$$h(x) = g(x) \otimes f(x) + background \quad - - ( 2.1 )$$

The instrumental profile  $g(x)$  is obtained using a standard material, free from defect such that the line broadening in the observed profile is only due to the instrumental factors. From the observed profile, the contribution of line broadening due to specimen  $f(x)$  can be extracted after deconvolution using the instrumental profile  $g(x)$ .

The geometrical properties of the spectrometer modify the diffraction profile in three ways. The profile is rendered asymmetrical, broadened, and shifted in position from its theoretical angle of deviation,  $2\theta$ . The various instrumental factors that influence the diffraction line profile are axial divergence of the beam, X-ray source profile, width of the receiving slit and errors due to flat specimen and displacement of the specimen from the diffractometer axis. The above factors which cause broadening depend on the diffraction angle. The variation of peak width with diffraction angle has been shown to depend on  $\tan\theta$ , and has been represented by a quadratic equation given by [52],

$$FWHM^2(2\theta) = U\tan^2\theta + V\tan\theta + W \quad - - ( 2.2 )$$

where  $FWHM$  denotes full width at half maximum,  $U$ ,  $V$  and  $W$  are the parameters describing the instrumental function. When the profiles from the standard are asymmetric, then the half width at half maximum on the low and high angle sides of the profile is chosen and fitted independently for two sets of  $U$ ,  $V$  and  $W$ . The above equation for



analyzing the angle dependent features of profile broadening is incorporated in to whole pattern fitting structure refinement methods by Young et al. [4] and some corrections were added later [53]. Howard and Snyder adapted the above equation for deconvoluting the instrumental contribution in their code SHADOW [54]. The instrumental parameters are generally ascertained for the instrument under use by using a standard powder specimen like Lanthanum hexaboride (LaB<sub>6</sub>).

The specimen contribution to broadening arises due to the finite size, microstrain arising from lattice imperfections and fault components of a crystal. Hence the intensity profile,  $I_{spec}$  from the specimen (earlier deconvoluted as  $f(x)$  in Eq. 1) is a convolution of the contributions to broadening from crystallite size, microstrain and faulting of the crystallites and is given as [55]

$$I_{spec} = I_{size} \otimes I_{strain} \otimes I_{fault} \quad - - (2.3)$$

Diffraction peaks, when deconvoluted for all non-Bragg components, i.e. background, instrumental contribution etc., bear information about crystallite size, mean-square strain and other microstructural parameters. The deconvoluted profile is usually termed as purely sample-related profile. To determine the size and microstrain components from the observed profile, certain analytical functions are used to fit the profile and to extract the peak position and peak width. On the basis of certain experimental and theoretical evidence, Warren [56] pointed out that Gaussian function can model strain distribution reasonably well and Cauchy function can model domain size variation well.

## 2.4 Profile functions in X-ray diffraction profile analysis

A variety of profile shape functions (PSFs) have been tried or suggested for fitting X-ray powder diffraction profiles. While no simple analytical presentation of the diffraction peak profile exists, it can be approximated by a suitable analytical function. In order to achieve

better fitting, it is essential to look for an analytical function with a shape that can vary between a Lorentzian and Gaussian function. Three such functions are extensively used in profile fitting, i.e., Voigt function, the pseudo-Voigt function and the split Pearson VII function. The Voigt function is the result of an analytical convolution of a Gaussian and a Lorentzian [57]. The split Pearson VII function can vary in shape from a purely Gaussian to Lorentzian function and is given by:

$$I(x) = I_p / \left(1 + x^2 / (ma^2)\right)^m \quad - - (2.4)$$

where,  $a$  and  $m$  are adjustable constants and  $x = 2\theta - 2\theta_p$  and  $2\theta_p$  is the exact Bragg angle. At  $m=1$  and  $m=\infty$ , the function tends to be Lorentzian and Gaussian respectively.

Another function which is often used for fitting XRD profiles is the pseudo-Voigt (pV) function. The pV function is a linear combination of Lorentzian and Gaussian with a mixing parameter ( $\eta$ ) which denotes the Lorentzian content [58]. The pseudo-Voigt function [15] for any profile is given as:

$$pV(x) = I_p [\eta C(x) + (1 - \eta)G(x)] \quad - - (2.5)$$

$$\text{where } C(x) = \frac{1}{1 + x^2}, \quad G(x) = e^{-(\ln 2)x^2}, \quad x = \frac{2\theta - 2\theta_p}{(\Gamma/2)},$$

$2\theta_p$  = peak position or exact Bragg angle

$\Gamma$  = FWHM of the profile

$\eta$  = Cauchy content of the pV function

$(1-\eta)$  = Gaussian content of the pV function and

$I_p$  = Intensity at the  $K\alpha_1$  peak maximum.

A comparison of different PSFs were carried out by Young and Wiles [16] in Rietveld refinements with data sets from different specimens. They showed that most promising results were obtained by using a pseudo-Voigt function and a Pearson type VII function. They stated that these PSFs will yield in Rietveld refinements the best separation of the background and, hence, the best Bragg intensity values and structural parameter results.

The pV function has been used to analyze the X-ray diffraction data from synchrotrons [59]. Recently, Sanchez et al. fitted a pseudo-Voigt function to XRD peaks and proposed an analytical model to determine the size distribution of nano crystalline materials [60]. Prabal Dasgupta [61] has carried out Fourier transform of pseudo-Voigt functions and concluded that if the Cauchy content is more than 0.328, meaningful results can be obtained from the analysis and hence pseudo-Voigt function can be used to fit the profile.

## **2.5 Metrics in profile fitting**

Rietveld [3] proposed a profile refinement method to solve neutron diffraction data. This method is based on the profile intensities obtained during step scans in neutron diffraction measurements and is used to refine the structural parameters of the specimen. This method is primarily for structure determination and is called as the whole-pattern-fitting structure refinement method [53] or the Rietveld method. However, profile fitting generally aims to fit the above discussed PSFs (§2.4) with the measured profile so as to obtain accurately the profile parameters like the peak position, profile width and peak intensity or the integrated intensity. The fitting procedure appropriately fits and minimizes the difference between the observed profile and the analytic function which has been chosen to fit the observed XRD profile. The advantage of profile fitting is that all of the intensity measurements defining the profile are used to determine the best way of fitting an analytical function to the observed envelope. Thus, the estimate of the peak location in  $2\theta$ , as well as its FWHM and integrated intensity will be determined by all measurements rather than just a few. In general, peak locations from profile fit data are twice as precise as those given by the second derivative technique. It is this second type of procedure which can be regarded more properly as profile fitting because here the fit is carried out on experimental data without imposing any structural constraint [62]. This method requires, in the first stage, an accurate determination of the instrumental function, which is subsequently convoluted

with a parametric function adjusted to fit the diffraction profile intensities of the specimen investigated.

To evaluate the fit obtained between the observed (obs) and calculated (calc) profiles certain  $R$  factors have been defined.  $R_{wp}$  is a measure of how well the entire pattern matches with the calculated pattern. The weighing factor,  $w_i$  is inversely proportional to the variance of the quantity in square brackets. The  $R$  factor,  $R_{wp}$  [53] is determined from the relation

$$R_{wp} = \left[ \frac{\sum w_i [I_i(obs) - I_i(calc)]^2}{\sum w_i (I_i(obs))^2} \right]^{1/2} \quad - - (2.6)$$

where,  $I_i(obs)$  and  $I_i(calc)$  are the observed and calculated intensities at  $i^{th}$  location in  $2\theta$  scale and the summation is over all the points in the pattern. Similarly,  $R_{Bragg}$  compares the integrated intensities ( $I_B$ ) of all the reflections being considered and is given by

$$R_{Bragg} = \frac{\sum [I_B(obs) - I_B(calc)]}{\sum (I_B(obs))} \quad - - (2.7)$$

$R_{wp}$  is statistically most meaningful indicator of overall fit in the sense that its numerator is the residual that is minimized in the least-squares procedure. However,  $R_{wp}$  is inflated both by contributions from background statistics and by shape differences between calculated and observed profiles even if they are adjusted to have nearly equal areas. Difference plots also provide unique information, such as systematic trends in the differences and aid in easy identification of any second phases which act as inflators of  $R_{wp}$ .

## 2.6 Microstructural causes of profile broadening

### 2.6.1 Crystallite size

Smaller crystallite size is the first microstructural feature that was observed by Scherrer to cause broadening of X-ray diffraction line profiles [9]. Broadening due to smaller crystallite size can be understood as follows: Generally, the plane participating in scattering a ray exactly out of phase with the ray from the first plane lies deep within the crystal, as the path difference between rays scattered by the first two planes differs only slightly from an integral number of wavelengths. In case, where the crystal is small, complete cancellation does not occur. As the number of planes decreases, the width of the diffraction curve increases. Hence, the observed broadening can be used to determine the crystallite size of the material and it is assumed that the broadening is only due to the size. The apparent crystallite size  $D_v$ , is related to the width of the peak at a height half-way between background and peak maximum ( $\beta_{fwhm}$ ) and is given by the famous Scherrer formula [9]

$$D_v = \frac{K_\beta \lambda}{\beta_{fwhm} \cos \theta} \quad - - (2.8)$$

where  $\lambda$  is the wavelength,  $\theta$  is the half of diffraction angle and  $K_\beta$  is the Scherrer constant [63]. If Eq. (2.8) is used with integral width ( $\beta_s$ ), defined as the total area under the diffraction maximum divided by the peak intensity [64], then the size determined is the volume average of the thickness of the crystallites along the direction of the diffraction vector and is actually denoted as  $L_v$  and is called the volume weighed mean column length [21]. The constant  $K_\beta$  in eqn. (2.8) depends on the shape of the crystallites and the reflections being considered. The  $K_\beta$  values for different shapes and reflections have been listed in the review of Scherrer equation published by Langford and Wilson [65].

Assuming spherical crystallites,  $K_\beta$  value of 0.9 and 1 are generally used for FWHM and integral width based equations, whereas the actual values are 0.83 and 1.07 respectively. In a polycrystalline material, if a grain is broken into smaller incoherently diffracting domains by dislocation arrays (small-angle boundaries), stacking faults, twins, large-angle boundaries (grains) or any other extended imperfections, then domain size broadening occurs. In the literature of XRD analysis, crystallite size and domain size are used in tandem.

The variance method proposed by Wilson is a single peak method, and is based on the second moment of the intensity distribution. The variance is taken over a region  $\pm\sigma$  of a diffraction line, where  $\sigma$  is measured from the centroid of the profile and  $\sigma$  is normally taken in the  $g$  space where  $g=2\sin\theta/\lambda$  [66]. In the variance method, variance is estimated over a range of truncated profile widths ranging from  $\sigma_1$  to  $\infty$  and is plotted as a function of  $\sigma$ . As the intensity varies asymptotically as the inverse square of the range, the variance is a linear function of range in the tail region of the profiles. From a plot of variance as a function of range, the crystallite size can be estimated. Further details about the variance method are detailed in literature [67,68]. This method has been applied for estimating the size of ZnO powder wherein strain effects were minimal [68].

### **2.6.2 Microstrain**

Strain generally is defined as the ratio of change in dimension with the original dimension and if it is estimated in one dimension, it is called as longitudinal strain. Further, the strain may be classified as uniform strain where the strain extends over large distances or at least over many grains causing peak shifts in XRD patterns. These are called as macro stresses. Non-uniform strain arises due to systematic shifts of atoms from their ideal positions due to defects, like point, line, planar and volume defects. This arises due to a number of

sources like vacancies, interstitials, dislocations, thermal expansion and contraction, etc. Each of these defects, except point defect, causes profile broadening and planar defects may be accompanied with peak shifts. These defects which cause broadening are due to the non-uniform distribution of the lattice strains which extend over a range which is dependent on the defect (see §1.2, pg. 3). Stokes and Wilson [69] connected broadening with lattice strains. They defined an apparent strain ( $\epsilon$ ) and considered how different distributions of strain (distortion) would affect the integral breadth,  $\beta_D$ . In cases where a complete strain range from zero to maximum is equally likely, then the upper bound for microstrain  $\epsilon_{\max}$  is given by

$$\epsilon_{\max} = \frac{\beta_D}{4 \tan \theta} \quad \text{-- ( 2.9 ).}$$

However, when the strain distributions are Gaussian, the rms microstrain  $\epsilon_{rms}$  was estimated by Stokes and Wilson as

$$\epsilon_{rms} = \frac{\beta_D}{2\sqrt{2\pi} \tan \theta} \quad \text{-- ( 2.10 ).}$$

The above two contributions by Scherrer and Stokes and Wilson have been the basis of understanding XRD profile broadening.

With the assumption of Gaussian strain distribution, the well known Warren-Averbach method is used to estimate the mean square strain and this method would be dealt in the following section (§2.7). However, it is worthwhile to mention about the alternate strain field model developed by van Berkum et al. [70] wherein a flexible model considering various distributions of lattice defects and their distortion fields were presented. In this model, the lattice defects were parameterized based on the distance between the defects, the amplitude of the strain fields, by mean square strain and the extent or width of strain fields. From these model parameters, the diffraction profiles were calculated. This model

was applied to study ball milled tungsten powder and the results indicate that wide component strain fields produce order dependent broadening. The order dependence of the shape and width of line profiles can be studied from this model.

## 2.7 Approaches in separating the size-strain effects

### 2.7.1 Williamson-Hall approach

In most of the polycrystalline materials, broadening of XRD profiles occurs due to size and strain related effects. When both these effects are present, the diffraction profile is a convolution of size and strain broadened profile. Assuming that the size and strain profile components are Lorentzian profiles, a linear addition of breadths is used in the Williamson and Hall method to separate the components of broadening. Herein, the fact that strain induced diffraction peak broadening follows a  $\tan\theta$  function whereas crystallite size broadening has  $1/\cos\theta$  dependence allows us to separate these effects. Hence the measured breadth  $\beta$  is given as  $\beta = \beta_s + \beta_D$ . Using Eqns. 2.8 and 2.9,  $\beta$  is written as

$$\beta \cos \theta = \frac{K_\beta \lambda}{D} + 4\varepsilon \sin \theta \quad - - (2.11).$$

This equation is the well known Williamson-Hall (WH) [13] equation for estimating the crystallite size  $D$  from the intercept and the microstrain  $\varepsilon$  from the slope of a plot between  $\beta \cos \theta$  vs.  $4 \sin \theta$ . Scherrer constant  $K_\beta$  as listed in [65] may be used depending on shape of the crystallite and a value of 1 is generally used when integral widths and spherical crystallites are considered as briefed in §2.6.1. The estimated  $D$ , actually is a measure of the volume weighted average column length  $L_v$ . This equation is based on the Cauchy-Cauchy approximation. Converting the integral breadths into reciprocal space units,  $\beta^* = \beta \cos \theta / \lambda$  and  $K = 2 \sin \theta / \lambda$  leads to an equation of the form

$$\beta^* = 1/D + 2\varepsilon K \quad - - (2.12).$$



The first term ' $1/D$ ' is replaced with ' $0.9/D$ ' if full width at half maximum (FWHM) value is used for breadth  $\beta$ . Also the above equation shows that size broadening is angle independent whereas strain broadening depends on diffracting angle. It should be noted that a large crystallite size results in a line with an intercept very close to zero. An uncertainty in large crystallite size values was occasionally observed, leading to negative intercept values.

Similarly, Cauchy-Gauss and Gauss-Gauss approximations can be used to add the breadths of the size and strain broadened profiles to give the following two equations:

$$\beta = (1/D) + (4\varepsilon^2 s^2 / \beta) \quad - - (2.13)$$

$$\beta^2 = (1/D)^2 + (4\varepsilon^2 s^2) \quad - - (2.14)$$

Equation 2.13 assumes the Cauchy size-broadened and Gaussian strain broadened profile, while Gaussian function is assumed for both size and strain in eqn. 2.14 [16].

### **2.7.2 Warren-Averbach method**

The theoretical background of size-strain separation was laid out initially by Warren and Averbach (WA) by plotting the variation of Fourier coefficients with column length which is the length perpendicular to the diffracting planes [71]. This is based on the Fourier line shape analysis of XRD profiles, as briefed below. The convolution of the size and strain broadened profiles in reciprocal space (XRD profile) can be estimated from the product of their Fourier transforms in real space. Hence, the cosine Fourier transform of the broadened profile  $A(L)$  due to microstructural features is given by

$$A(L, g) = A^S(L)A^D(L, g) \quad - - (2.15)$$

where  $A^S(L)$  denotes the order-independent size Fourier coefficient and  $A^D(L, g)$  is the order dependent strain Fourier coefficient (or distortion coefficient) and  $L$  is the Fourier

variable:  $L=na_3$ ,  $n$  are integers and  $a_3$  the unit of Fourier length in the direction of the diffraction vector  $g$ :

$$a_3 = \frac{\lambda}{2(\sin \theta_2 - \sin \theta_1)} \quad - - (2.16)$$

wherein the diffraction profile has been measured within the angular range  $2\theta_2$  and  $2\theta_1$ .

Eqn. (2.15) maybe written as

$$\ln A(L, g) = \ln A^S(L) + \ln A^D(L, g) \quad - - (2.17)$$

The distortion coefficient is a cosine function which is approximated to an exponential for small values of  $L$  and hence  $\ln A(L)$  can be written as:

$$\ln A(L) \approx \ln(A^S(L)) - 2\pi^2 \langle \varepsilon^2(L) \rangle L^2 / d_{hkl}^2 \quad - - (2.18)$$

where  $\langle \varepsilon^2(L) \rangle$  is the mean square of the strain component perpendicular to the reflecting planes averaged over the length  $L$  and  $g=1/d$ . Eqn. (2.18) is known as the Warren-Averbach method of size-strain separation [14]. If at least two reflections from the same crystallographic-plane family are available, it is possible to separate the crystallite size and microstrain contributions (distortion effects) to profile broadening from pure-specimen broadening. From the plot of  $\ln A(L)$  vs.  $1/d_{hkl}^2$ , the size coefficient is estimated from the intercept and  $\langle \varepsilon^2(L) \rangle$  is evaluated from the slope for each value of  $L$ . From the plot of the size coefficient,  $A^S(L)$  vs.  $L$ , the area-weighted average column length  $\langle L \rangle_{area}$  can be obtained from the initial slope

$$\left[ \frac{dA^S(L)}{dL} \right]_{L \rightarrow 0} = - \frac{1}{\langle L \rangle_{area}} \quad - - (2.19).$$

The volume-weighted average column length can be obtained by integrating the size coefficient as proposed by Krill & Birringer [72] and is given as

$$\langle L \rangle_{vol} = 2 \int_0^{\infty} A^s(L) dL \quad \text{-- ( 2.20 ).}$$

The second derivative of the size coefficients is proportional to the surface-weighted column-length distribution function,

$$\left[ \frac{d^2 A^s(L)}{dL^2} \right]_{L \rightarrow 0} \propto P_s(L) \quad \text{-- ( 2.21 ).}$$

The column-length distribution function is related to the true crystallite-size distribution function, but it also depends on the shapes of crystallites and the order of reflection [73]. Fourier analysis of the peak profiles can in principle give information on the column length distribution of the diffracting domains based on the column length model of Bertaut [15]. Figure 2.1 shows typical columns of 5 unit cells arranged in spherical particles of various sizes. The XRD analysis provides information about the column length average and its distribution. This information has been used by Mahadevan et al. [74] to assess the shape of the nano particles and the size estimates were compared with Dynamic light scattering measurements.

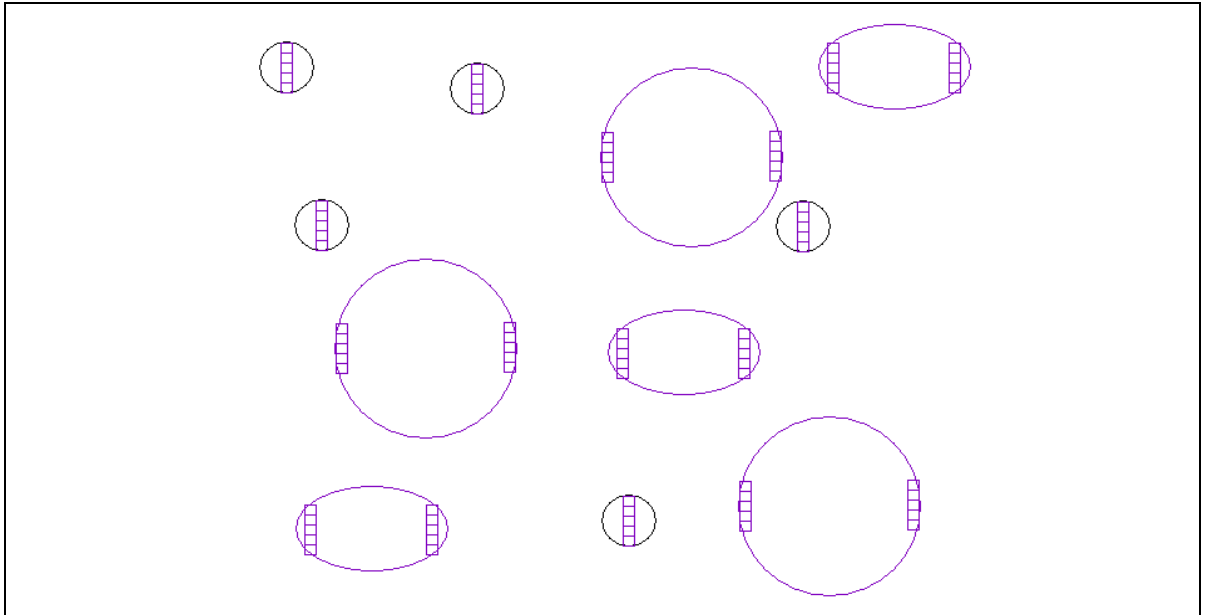


Fig. 2.1. Typical representation of columns with 5 unit cells are shown in particles with different sizes and shapes

### 2.7.3 Other approaches

Langford [57] used the Voigt function and derived the Cauchy ( $\beta_C$ ) and Gaussian ( $\beta_G$ ) components of profile broadening from FWHM ( $I$ ) and integral breadth ( $\beta$ ) of XRD profiles. De Keijser et al. [75] used the components of Voigt function (of each of the peaks) to estimate the crystallite size and microstrain by using  $\beta_C$  and  $\beta_D$  in Eqns. (2.8) and (2.9) respectively. They analyzed the errors that can occur in such a single peak analysis and concluded that the error in crystallite size and microstrain are more if the  $g$  (instrumental) and  $f$  (specimen) profiles are of the same order of magnitude. Balzar and Ledbetter [16] proposed the double-Voigt method wherein the size and strain broadened profiles are assumed to be Voigtian. They obtained the Fourier transformation of the Voigt function and were able to express the Fourier coefficients in terms of  $\beta_C$  and  $\beta_G$  and is given by:

$$A(L) = \exp [-2L\beta_C - \pi L^2 \beta_G^2] \quad \text{-- ( 2.22 )}.$$

They derived expressions for the volume weighted domain size  $D_V$ ,  $\langle \varepsilon^2(L) \rangle$  and the column length distribution from the various components of the profile parameters. This approach showed that this alternative Fourier approach using Voigt function with the assumption of the Gaussian strain distribution leads to Warren and Averbach method of separation of the size and strain distribution.

It is also worthwhile to mention that the methods based on variance are also in use for separating the contribution to size-strain broadening. When XRD profile broadening is dominated due to size effects, Wilson proposed that, mean-square breadth (variance) of a truncated profile (§2.6.1) is a measure of mean crystallite size [66]. Wilson by considering negligible broadening of XRD profiles due to size effects, derived relations to estimate strain from variance of diffraction peaks [76]. He concluded that strain adds a

contribution to the variance that increases with the square of the order of reflection but is independent of the range of integration as stated in §2.6.1. These two contributions were incorporated by Bajo et al. [77] to propose a method for determining variance from the profile parameters of a pseudo Voigt function. The variance thus obtained is used for determining mean crystallite size and root-mean square strain.

## 2.8 Modified approaches for separating the size-strain effects

The approaches presented in §2.7 are valid when the observed profile broadening is isotropic along various crystallographic directions. The anisotropy arises from crystallite shape being non-uniform or strain being anisotropic. All experimental evidence showed that strain,  $\langle \varepsilon^2(L, g) \rangle$  is dependent on  $L$  as well as on diffraction order  $g$ . To explain the order dependence, few phenomenological models were proposed based on the anisotropic elastic constants, by Stokes and Wilson in 1942 [69] and by Stephens in 1999 [78]. Similarly, the order dependence was explained by Krivoglaz [79] on the basis of dislocation model of mean square strain. The dislocation model of strain,  $\langle \varepsilon^2(L, g) \rangle$ , is based on the effect of dislocations to strain broadening and depends on the relative orientation of the Burgers vector  $\mathbf{b}$  and diffraction vector  $\mathbf{g}$ . This implies that if  $\mathbf{b} \cdot \mathbf{g} = 0$ , the dislocation is invisible and has no contribution to profile broadening. This is similar to the contrast effects in electron microscopy. The dislocation model was used by Ungár and Borbély [17] to address the anisotropic broadening observed in XRD profiles and proposed the modified Williamson-Hall and Warren-Averbach approaches.

### 2.8.1 Modified Williamson-Hall (mWH) approach

When the contribution to strain broadening is caused by dislocations, the WH plot discussed in §2.6.1 is not linear and a modified Williamson-Hall equation has been derived by Ungár and Borbély [17,18] and is given by

$$\beta^* = 1/D + \alpha(K\bar{C}^{1/2}) + O(K^2\bar{C}) \quad - - (2.23)$$

where,  $\alpha = (\pi A^2 b^2 / 2)^{1/2} \rho^{1/2}$  is called the hkl independent or normalized mean square strain and  $O$  indicates non-interpreted higher-order terms. The variable  $A$  is a constant depending on the effective outer cutoff radius of dislocations ( $R_e$ ),  $b$  is the Burgers vector,  $\rho$  is the dislocation density and  $\bar{C}$  is the average contrast factor of the dislocations. The average contrast factor  $\bar{C}$  takes into account the relative orientation between diffraction vector and Burgers vector. The Eqn. (2.23) shows that, if dislocations are the primary source of strain, the scaling factor for breadths is  $K\bar{C}^{1/2}$  instead of  $K$ . The third term in eqn. (2.23) is important if there is local fluctuation in the dislocation density [20]. For brevity, the normalized mean square strain ( $\alpha$ ) would be mentioned as microstrain ( $\alpha$ ) at a few locations in this thesis, as the microstrain  $\varepsilon$  derived from WH plot is not reported in this study.

The estimation of average contrast factor  $\bar{C}$  is important for making these modified Williamson-Hall plots. It has been shown by Ungár et al. [80] that, in an untextured cubic polycrystalline specimen or one with randomly populated Burgers vectors (slip systems), the values of average contrast factors are simple fourth order polynomials of  $hkl$  and are given by

$$\bar{C}_{hkl} = \bar{C}_{hoo}(1 - qH^2) \quad - - (2.24)$$

where,  $H^2 = (h^2k^2 + k^2l^2 + l^2h^2)/(h^2 + k^2 + l^2)^2$  and  $q=B/A$  with  $A$  and  $B$  as constants which depend on the elastic constants of the crystal. The value of  $A$  is the average contrast factor corresponding to the indices  $h00$ :  $\bar{C}_{h00} = A$ . Ungár et al. [81] proposed methods for estimating the theoretical and experimental ‘ $q$ ’ factors and  $\bar{C}_{h00}$  for cubic crystals and described them in detail. For brevity, it is sufficient to indicate that the procedure for estimating  $q$  follows from the quadratic form of Eqn. (2.23) which is given by

$$(\beta^*)^2 = (1/D)^2 + \alpha^2(K^2\bar{C}) \pm O(K^2\bar{C})^2 \quad - - (2.25).$$

Substituting Eqn. (2.24) into (2.25) yields

$$[(\beta^*)^2 - (1/D)^2]/K^2 \approx \alpha^2\bar{C}_{h00}(1 - qH^2) \quad - - (2.26).$$

The parameter ‘ $q$ ’ can be estimated from experimental data by using linear regression of left hand side of equation (2.26) by varying the value of  $D$  versus  $H^2$ . The ‘ $q$ ’ factor thus determined is used to estimate the average contrast factors of various planes as per equation (2.24) which is used to draw the modified Williamson-Hall plot.

### 2.8.2 Modified Warren-Averbach (mWA) method

In a crystal with dislocations, for small  $L$  values,  $\langle \varepsilon^2(L, g) \rangle$  was arrived at by Krivoglaz [79] and is given by:

$$\langle \varepsilon_{L,g}^2 \rangle \cong \frac{\rho \bar{C} b^2}{4\pi} \ln \left( \frac{R_e}{L} \right) \quad - - (2.27)$$

where  $R_e$ ,  $b$  and  $\rho$  are the effective outer cut-off radius of dislocations, modulus of the Burgers vector and dislocation density respectively.  $\bar{C}$ , the average contrast factor takes into account the relative orientation between diffraction vector and Burgers vector. Substituting eqn. (2.27) in to (2.18) yields the modified Warren-Averbach equation and is given as:

$$\ln A(L) \cong \ln A^S(L) - \rho B L^2 \ln \left( \frac{R_e}{L} \right) (K^2 \bar{C}) + O(K^2 \bar{C})^2 \quad - - (2.28)$$

where  $O$  stands for higher order terms, details of which can be found in [17] and [10] with  $B = \pi b^2/2$ . The scaling factor here is  $K^2 \bar{C}$  instead of  $K^2$ . A plot of  $\ln A(L)$  vs.  $K^2 \bar{C}$  yields the size coefficient from the intercept, and the coefficient of the first order term gives the estimate of  $\rho B L^2 \ln(R_e/L)$  for each value of  $L$  and is termed as  $X(L)$ . The average dislocation density  $\rho$  and  $R_e$  can be estimated from a plot of  $X(L)/L^2$  vs.  $\ln L$  based on the equation below:

$$X(L)/L^2 = B \rho \ln R_e - B \rho \ln L \quad - - (2.29).$$

It is to be noted that the outer cut-off radius of dislocations,  $R_e$  has nothing to do with the crystallite size, but is basically a parameter characterizing the distribution and the interaction of the dislocations in the analyzed region [18].

The apparent size value determined from the FWHM and the integral breadth using Eqn. (2.23) and the area weighted column length estimated from Fourier coefficients reflect the largest, medium and smallest lengths in the specimen since they are related to the central part, the integral and the outer-most tails of the profiles, respectively.

## 2.9 Application of XRD LPA in materials

This section would focus on studies which were focused towards size-strain separation using XRD LPA but are not related to ageing induced precipitation.

### 2.9.1 Studies using WH and WA approaches

Williamson and Hall [13] studied the effect of annealing the filings of Aluminium and Wolfram by the size-strain separation method (§2.7.1) proposed by them. They concluded that a smaller density of dislocations persists even after annealing. Similarly a single crystal of Cu with 2% Si, was studied by Warren and Averbach [14] by rolling it up to



50%, and concluded that, distortion is the major cause of broadening with little influence from changes in crystallite size. Turunen et al. [82] studied the recovery process of cold rolled aluminium during isochronal ageing at different temperatures from the variation of  $\langle \varepsilon^2(L) \rangle$  as a function of column length  $L$ . They were able to identify the characteristic sharpening of the cell boundaries that occurs during type I recovery from an increase of the averages of the derivatives of mean squared strain. The decrease observed at higher annealing temperatures was attributed to the annihilation and movement of cell walls that occur during type II recovery. Jayan et al. [83] studied the effect of long term ageing on size of carbide precipitates in 2.25Cr–1Mo steel tubes using WH and WA techniques. The crystallite size estimated by these techniques compared well with each other and the size of the carbides increased with increase in the ageing duration from 74,000 to 160,000 hours. In Fe-Al alloys prepared by mechanical alloying, the crystallite size and mean lattice strain were estimated for various milling times using the Williamson-Hall plot, without accounting for the anisotropic broadening [84]. The domain size, microstrain within the domain and dislocation density were estimated by the simplified breadth method, Williamson–Hall technique and the modified Rietveld method in deformed polycrystalline Zr alloys [85]. These authors found that anisotropy of domain shape exists along different crystallographic directions.

### **2.9.2 Studies using modified WH and WA approaches**

Ungár et al. [18] applied the modified WH and WA approaches to address the anisotropic broadening observed in inert gas condensed nanocrystalline copper. They determined the particle size and the dislocation structure using these approaches. The particle size was in the range of 14 to 30 nm with a dislocation density of  $5 \times 10^{15} \text{ m}^{-2}$ . Ungár et al. [86] studied the variation in grain size and dislocation density in nanocrystalline electrodeposited Ni

foils by these approaches. The average grain size ranges from 50 to 12 nm, as determined from FWHM and Fourier analysis which were in good agreement with TEM observations. They determined the average dislocation density to be  $4.9 \times 10^{15} \text{ m}^{-2}$ , and also inferred that the dislocations were mostly of screw character. The modified WH and WA procedures were applied and tested on a nanocrystalline powder of silicon nitride and a severely plastically deformed bulk copper specimen [19]. They found good agreement between X-ray and TEM data for nanocrystalline loose powders. Ungár et al. [87] carried out XRD/LPA analysis of SiC specimens sintered at 1800 °C at pressures of 2 and 5.5 GPa. Their study was able to provide quantitative numbers for crystallite or sub-grain size, dislocation densities, and planar fault densities or frequencies. M300 grade 18Ni maraging steel deformed by equal channel angular pressing was studied by modified WH and WA approaches for understanding the microstructural evolution [88]. The study revealed an increase in dislocation density on severe plastic deformation with relative increase in screw dislocations. Dey et al. [20] applied the modified approaches to study the effect of cold work in Pb-Bi alloys. The WH plot and modified WH plot for annealed Pb, 15% Bi alloy is shown in Fig. 2.2. The anisotropic broadening observed in Fig. 2.2(a) is addressed by the modified approach as shown in Fig. 2.2(b) [20]. Their analysis revealed that annealing leads to a decrease in dislocation density and is dependent on the wt% of Bi in the alloy.

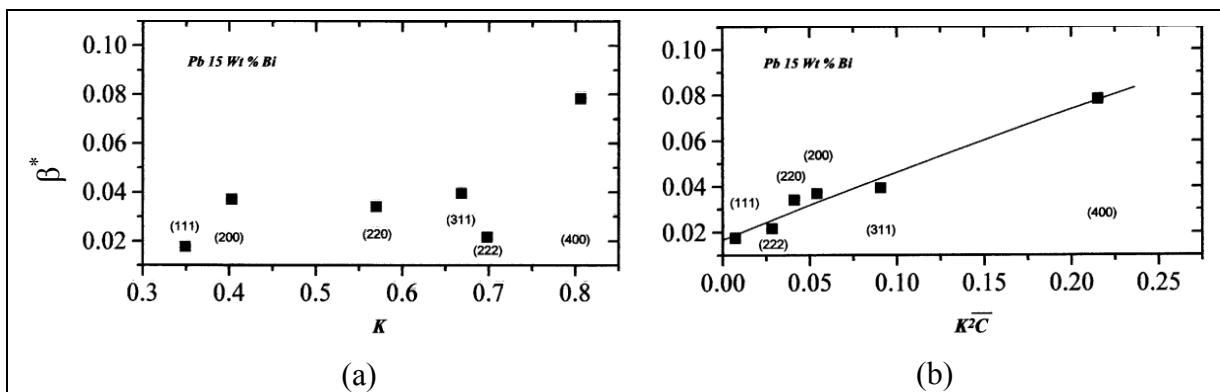


Fig. 2.2. (a) Williamson-Hall plot and (b) modified WH plot for Pb 15 wt% Bi alloy [20].

### **2.9.3    *Implications***

The literature presented above clearly shows that the modified approaches have been mostly used for studying nanocrystalline materials, ball milled powders, in cold rolled materials and in deformation carried out using equal channel angular processes. Hence, it is clear that application of XRD/LPA for studying ageing behaviour would widen the scope of profile analysis and improve the understanding of precipitation induced microstructural changes to the matrix.

## Chapter - 3

### 3 Experimental methods

In this study, age hardening behaviour of 17-4 PH steel and M250 grade maraging steel is planned. In this chapter, the chemical composition and the ageing treatments carried out on these two steels would be briefed. The details of the experimental techniques used to study the microstructural changes like X-ray diffraction and scanning electron microscopy would also be presented. The details of hardness measurements carried out to evaluate the increase in strength would also be briefed.

#### 3.1 Sample details

##### 3.1.1 17-4 PH steel

Specimens of 17-4 PH stainless steel with dimensions 10 mm x 10 mm x 3 mm were cut from mill annealed plates. The chemical composition (in wt. %) of the 17-4 PH stainless steel used in this study is shown in Table 3.1.

Table 3.1 Chemical composition of 17-4 PH steel (wt. %)

Cr	Ni	Cu	Si	Mn	Nb	S	P	C	Fe
16.3	4.5	3.75	0.32	0.5	0.2	0.01	0.02	0.040	Bal

The specimens were solution annealed at 1040 °C (1313 K) for one hour and followed by water quenching. These solution annealed specimens were isochronally heat treated at various temperatures ranging from 430 to 530 °C (703 to 803 K) for different durations, as shown in Table 3.2 followed by air cooling. The lower temperature heat treatment at 380 °C (653 K) for durations of 0.5 and 1 h were carried out to understand early precipitation behaviour. It is to be noted that precipitation kinetics is generally studied isothermally, and the results of precipitation kinetics would be presented based on the isothermal representation.

Table 3.2 Heat treatment details of 17-4 PH steel

Ageing duration in hours (h)	Temperature in °C (K)			
0.5	380 (653)	430 (703)	480 (753)	530 (803)
1	380 (653)	430 (703)	480 (753)	530 (803)
3	-	430 (703)	480 (753)	530 (803)

### 3.1.2 M250 grade maraging steel

The chemical composition (wt. %) of the M250 grade maraging steel used in this study is given in Table 3.3. A 15 mm thick plate of maraging steel was solution annealed at 820 °C (1093 K) for 1 h followed by air cooling. The specimens of approximate dimensions 30 mm x 25 mm x 7 mm extracted from the solution annealed plates, were encapsulated in quartz tubes under vacuum and aged at 482 °C (755 K) for different durations of 0.25, 1, 3, 10, 40, 70 and 100 h followed by water quenching.

Table 3.3 Chemical composition of M250 grade maraging steel (wt. %)

Ni	Co	Mo	Ti	Mn	Cr	Si	Cu	Al	C	Fe
17.89	8.16	4.88	0.43	0.05	0.05	0.05	0.05	0.096	0.003	Bal

## 3.2 Hardness measurements

The hardness measurements in 17-4 PH steel specimens were carried out using 423D digital Vickers hardness tester manufactured by M/s Innovatest with a load of 1kg. Similarly, hardness measurements in M250 grade maraging steel specimens were carried out with 10 kg load. Five measurements were done on each sample and the average value was taken. The observed maximum scatter in hardness for each sample was found to be within  $\pm 5$  VHN.

### **3.3 X-ray diffraction measurements**

#### **3.3.1 Details of diffractometer**

The XRD profiles of all the samples were recorded using MAC Science MXP18 X-ray diffractometer with Cu K $\alpha$  radiation. The X-ray tube is evacuated to a vacuum level of  $1 \times 10^{-7}$  mbar using a combination of turbo-molecular pump and rotary pump. The instrument which has a fixed tube is set up in the Bragg - Brentano geometry with a line focus and a graphite monochromator in the diffracted beam arm. The diffractometer has a  $2\theta$  scan range extending from  $-3^\circ$  to  $130^\circ$ . The diffracted X-ray beam is then detected using the scintillation detector. The system has suitable holders to hold powder specimens and solid samples. The experimental parameters and acquisition of data are automated and can be adjusted using an interfaced computer system.

#### **3.3.2 Experimental conditions used for XRD data acquisition**

X-ray diffraction profiles of all the 17-4 PH steel specimens were obtained with Cu K $\alpha$  radiation in the angular range of  $40 - 120^\circ$  with a step size of  $0.02^\circ$  and dwell time of 4 seconds per step. The tube was operated at a power level of 35 kV x 80 mA. Similarly XRD spectra of M250 grade maraging steel specimens were recorded in the angular range of  $36 - 122^\circ$  with a step size of  $0.02^\circ$  and dwell time of 4s. Both the divergence slit (DS) and receiving slit (RS) were set at  $0.5^\circ$ . The slit width at the monochromator was 0.15 mm. For obtaining the instrumental function, data from LaB $_6$  powder was obtained.

#### **3.3.3 Analysis of diffraction data**

The individual XRD peak profile corresponding to each plane was extracted for all the samples by fitting a suitable background along with a pseudo-Voigt function [58] after accounting for instrumental broadening. The profile refinement was carried out using the software XPRESS available along with the diffractometer. The profile refinement is based

on the approach of Howard and Snyder used in the program SHADOW [54]. The refinement gave the parameters of the pseudo-Voigt function like peak position, full width at half maximum (FWHM) and Gauss content of these peaks. The values of FWHM and integral breadth used in the analysis were estimated from the extracted individual profiles.

### **3.4 SEM investigations**

The heat treated specimens were polished metallographically and etched using Fry's reagent for microstructural studies using the CamScan 3200 Scanning Electron Microscope (SEM). The etched specimens were observed in the secondary electron (SE) mode. The microscope is operated at an accelerating voltage of 20 kV with an emission current of  $\sim 65 \mu\text{A}$ . The working distance between the lens and the sample were adjusted according to the requirement of the investigation. Larger working distance results in higher depth of focus, whereas smaller working distance results in higher resolution. As and when required, the specimens were tilted at an appropriate angle to properly observe the microstructure.

## Chapter – 4

### 4 Studies on ageing behaviour of 17-4 PH steel

In this chapter, the changes in hardness on ageing would be presented first and the kinetic parameters derived from the change in hardness would be elucidated. This would be followed by the results from XRD analysis. The crystallite size and microstrain estimated from the modified WH approach [§2.8.1] would be presented and explained. The results of the changes in lattice parameter would be presented and used for estimating the precipitate fraction. Finally, the strengthening mechanisms active in this steel would be discussed. The calculated strengthening would be compared with experimentally measured hardness by using an unique approach.

#### 4.1 Hardness changes on ageing

The variation of hardness with ageing temperature at various ageing times is shown in Fig. 4.1. (The dotted lines act as a guide to the eye in following the changes.) In this figure and all figures henceforth, the legend SA in the abscissa indicates solution annealed specimen. The specimens aged for 0.5 h shows an increase in hardness as the temperature is increased to 380 °C (653 K) and reaches a peak hardness of 434 VHN at 480 °C (753 K). On further increasing the temperature to 530 °C (803 K), the hardness decreased to a value which is still higher than that observed in solutionized sample. Similarly, on ageing the specimens for 1 h at various temperatures, it is seen that the hardness peaks at 430 °C (703 K). As the temperature is increased to 480 °C (753 K), the hardness decreases marginally to 431 VHN from 435 VHN. Further increase in the temperature reduces the hardness. On ageing the specimens for 3 h at 430 °C (703 K), a peak hardness of 460 VHN is achieved and decreases with increasing ageing temperature. A similar peak hardness value of 450 VHN has been reported for this steel in other studies [35,37]. The increase in the hardness



follows the typical age hardening behaviour. The decrease in the hardness on increasing the temperature is in agreement with that reported by Wang et al. [38] wherein, with increase in holding time, the copper precipitates grow and lose their coherency with the matrix leading to reduction in hardness.

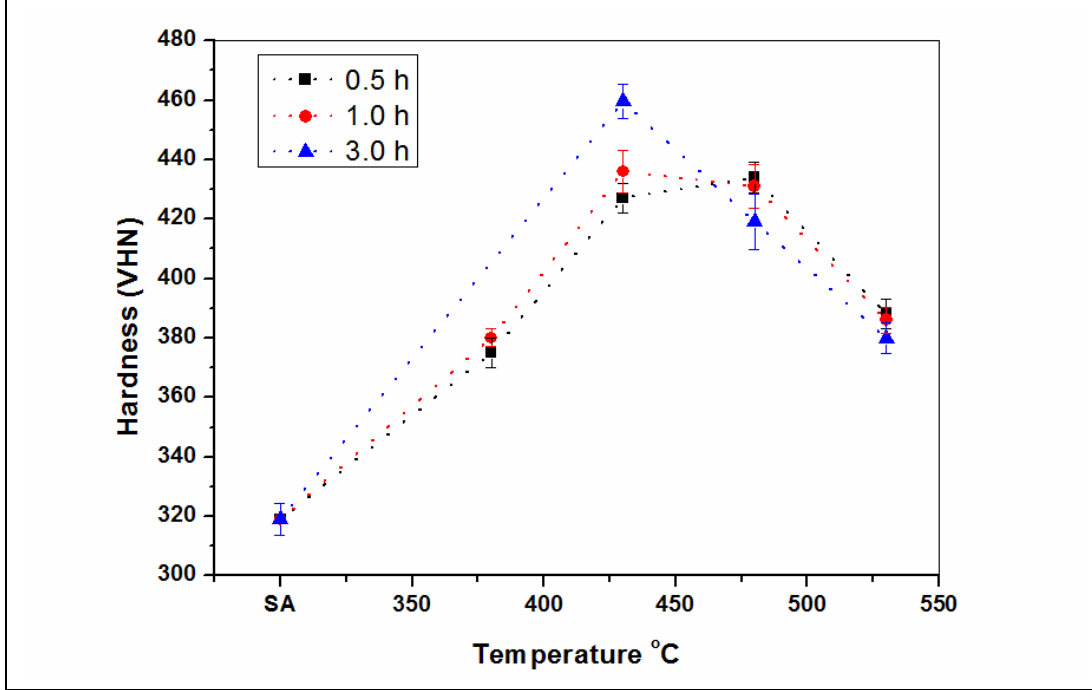


Fig. 4.1. Variation of hardness with ageing temperature of 17-4 PH samples isochronally aged for durations of 0.5, 1 and 3 h

#### 4.1.1 Precipitation kinetics in the age hardening regime

The ageing kinetics is studied based on the Avrami equation [89] wherein the fraction of precipitates ( $f$ ) transformed at a given temperature is given by

$$f = 1 - \exp(-kt)^n \quad \text{--- (4.1)}$$

where  $t$  is the ageing time (s),  $k$  is the reaction rate constant and  $n$  is the Avrami exponent. The kinetics of precipitation has been studied by calorimetry, variations in hardness and resistivity by various authors [27,28,31]. In earlier studies, the fraction transformed has been assumed to be linearly dependent on hardness or resistivity. However, a more

appropriate relationship has been derived by Robino et al. [90] and has been shown to be proportional to  $H^{3/2}$  where H is the hardness.

Hence, to study the kinetics during the age hardening regime, the hardness changes on ageing at 430 °C (703 K) are used. The measured hardness at 430 °C (703 K) for varying durations are normalized with respect to the peak hardness ( $H^{3/2}$ ) achieved at this temperature. The variation of hardness ( $H^{3/2}$ ) (equivalent to the precipitate fraction) with ageing time at 430 °C (703 K) is shown in Fig. 4.2. The fit obtained for the Avrami equation (eqn. 4.1) gives an  $n$  value of 0.52 (at 430 °C) which is in close agreement with the values of 0.44 and 0.46 obtained by Mirzadeh and Najafizadeh [39] at temperatures of 400 and 450 °C respectively for this steel. A theoretical  $n$  value of  $\sim 2/3$  has been predicted from the Avrami equation for precipitation on dislocations [90]. Hence, the value of  $n$  obtained herein points to enhanced nucleation of Cu due to the high density of dislocations present in this steel.

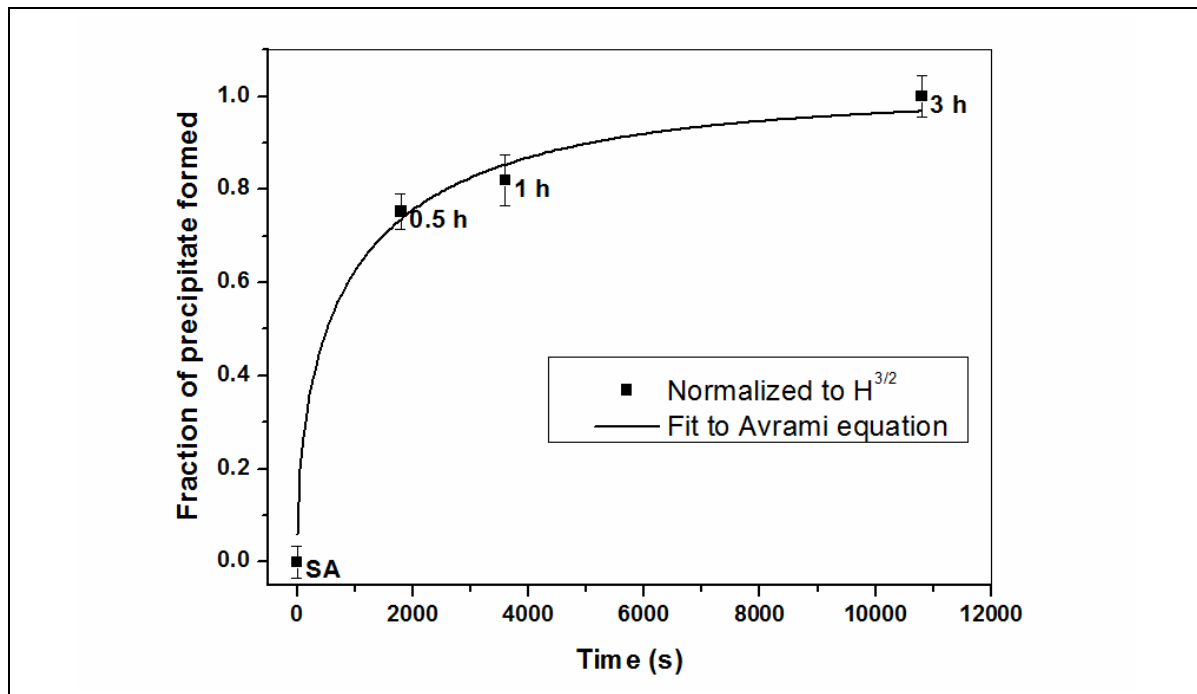


Fig. 4.2. Fit of the Avrami equation using normalized hardness<sup>3/2</sup> (the Avrami equation is conventionally fitted on a time scale in seconds, hence the legends show the ageing duration in h)

#### 4.1.2 *Precipitation kinetics in the overaged regime*

Once peak hardness is achieved, on further increasing the ageing time the hardness decreases. The change in hardness is related to the ageing time ( $t$ ) through an equation proposed by Wilson [91] which is based on the Orowan mechanism and is given as;

$$\left(\frac{1}{\Delta H}\right)^3 = M(t - t_o) + \left(\frac{1}{\Delta H_o}\right)^3 \quad \text{-- ( 4.2 )}$$

where  $\Delta H_o$  is the increase in hardness at the commencement of coarsening time  $t_o$ , which is equal to the difference between peak hardness and hardness in solutionized condition,  $\Delta H$  is the difference between the hardening of the overaged sample and the solutionized sample.  $M$  is a constant which is dependent on temperature.

In the overageing regime, wherein the hardness decreases with time, the change in hardness is analysed based on the Wilson model briefed above. The variation of  $1/\Delta H^3$  with ageing time at temperatures of 480 and 530 °C is shown in Fig. 4.3. The data is fitted to eqn. 4.2 and is also shown in Fig. 4.3. The correlation coefficient is better than 0.99, which indicates that the observed changes in precipitation hardening on overageing are due to Orowan bowing and the yielding is isotropic [91]. Though measurements were conducted at two different temperatures in the over ageing regime, the intercept ( $M$  in eqn. 4.2) of the two curves shown in Fig. 4.3 were used to estimate the activation energy using the Wilson approach based on a plot of  $\ln(MkT)$  versus  $1/T$  [91], which gives an activation energy of  $143 \pm 20$  kJ/mol. Viswanathan et al. [28] estimated an activation energy of 112 kJ/mol from resistivity measurements in 17-4 PH steel. The above values are lower than the activation energy of 186 kJ/mol determined by Hornbogen and Glenn [92] for Cu diffusion in alpha iron. The lower value was attributed to enhanced diffusion of copper through the matrix assisted by dislocations. Large variation in activation energy ranging from 71 to 240 kJ/mol has been reported for Fe-Cu alloys with different alloying elements

[93]. Hence the activation energy arrived at in this study points to an assisted diffusion process.

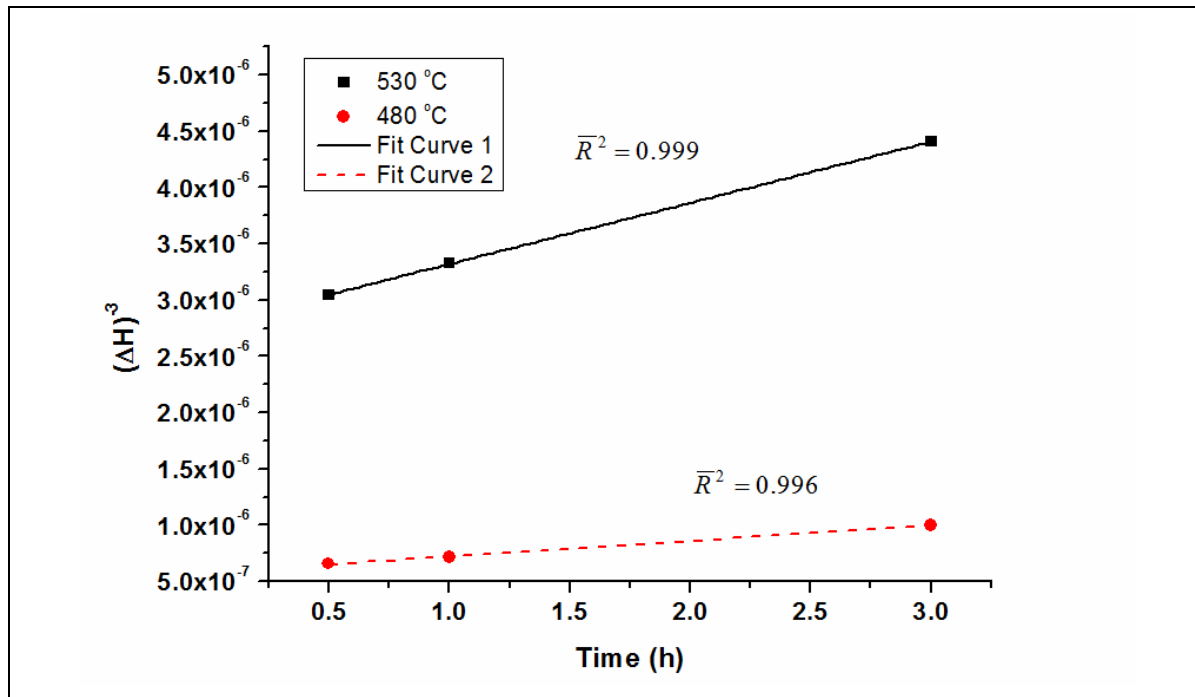


Fig. 4.3. Variation of change in overaged hardness with ageing time

#### 4.1.3 Variation of hardness with tempering parameter

Since ageing of the material has been carried out at various temperatures and durations, it is necessary to correlate the observed variation in the hardness under different ageing times and temperatures through a single variable. This is possible by adapting the Hollomon-Jaffe parameter [48] which is commonly known as the tempering or Larson-Miller parameter (P) which is given by

$$P = T(C + \log t) \times 10^{-3} \quad \text{-- ( 4.3 )}$$

where  $T$  is absolute temperature in K,  $t$  is the tempering time in hours and  $C$  is a material constant. Mirzadeh and Najafizadeh [94] collated the age hardening data of 17-4 PH steel carried out by different authors and correlated the relative percentage of hardening achieved with tempering parameter by using artificial neural network approach. They used a single curve to fit the variation of hardness with tempering parameter in both the

age hardening and overageing regimes by using a  $C$  value of 20. It is to be noted that the Hollomon-Jaffe parameter was determined based on the fact that softening results from diffusion phenomenon. Gomes et al. [95] by comparing different tempering parameters felt that Hollomon-Jaffe parameter is valid only if the physical phenomenon leading to softening is the same over the whole temperature range and if temperature only impacts the kinetics. In the age hardening regime at lower temperatures and times, dislocation annihilation and precipitation compete with each other.

The variation of hardness with tempering parameter (with  $C=20$ ) is shown in Fig. 4.4. In Fig. 4.4, the hardness values in the age hardening regime are shown as open circles and in the overaged condition as filled circles. Once peak hardness is achieved at each of the temperatures, the kinetics is mostly driven by precipitate coarsening and hardness decreases with time. In the overaged condition, a linear fit is obtained to the data and the  $\bar{R}^2$  value is shown in the figure. Since the hardness decreases from a peak hardness value of 459 VHN, this data is also included, to fit the reduction in hardness observed in overaged condition. Such linear behaviour has been observed while studying softening of die steels [96]. A decrease in hardness with tempering parameter was fitted to a third degree polynomial by Vasudevan et al. [97] while studying softening of different % cold worked stainless steels.

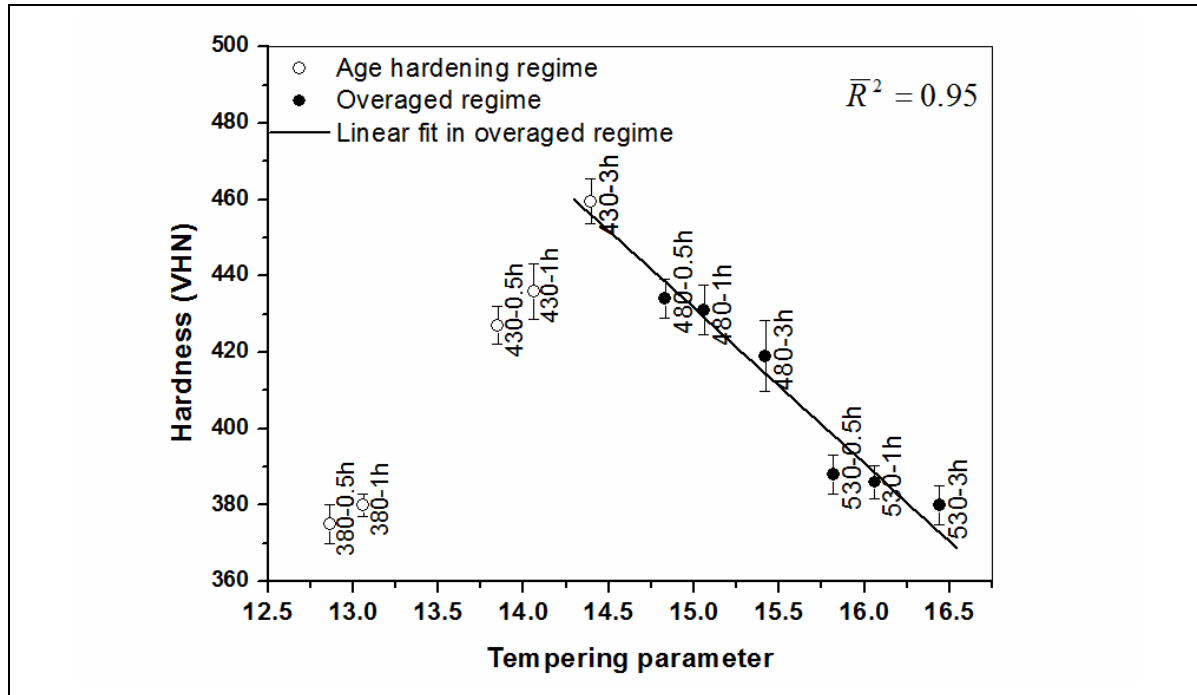


Fig. 4.4. Variation of hardness with tempering parameter

From the data presented in the age hardening regime (open circles), a linear fit appears to be appropriate. However, analysis of hardness data published by Viswanathan et al. [27] and Hsiao et al. [35] points to an S type curve similar to the JMA equation (4.1) would give a better fit. Mirzadeh et al. [94] had used a hyperbolic tan function to fit the data in the age hardening regime. Shin et al, [98] carried out microstructural investigation of precipitation hardenable martensitic steel and plotted the variation of hardness with tempering parameter without any fit. Their data in the age hardening regime does not indicate a linear behaviour in the age hardening regime. Hence, with the limited data presented herein, it cannot be conclusively proven that a linear fit is appropriate. Hence the data in age hardening regime is left as open circle.

## 4.2 XRD analysis and SEM investigations

X-ray diffractograms of all the specimens used in the study were obtained with the experimental parameters mentioned in §3.3.2. The X-ray diffractograms of the specimens aged at 380 and 480 °C (653 and 753 K) for 0.5 h along with that of solution annealed

specimen are shown in Fig. 4.5. The reflections from the solution annealed specimen revealed pure bcc structure and they are indexed in Fig. 4.5. The widths of the bcc reflections increase marginally on ageing for 0.5 h at 380 °C (653 K), and no additional reflections are seen. However on ageing for 0.5 h at 480 °C (753 K), additional reflections corresponding to an fcc phase are identified and indexed. The full width at half maximum (FWHM -  $\beta$ ) corresponding to the bcc phase and peak location were determined for all the specimens using the procedures mentioned in §3.3.3.

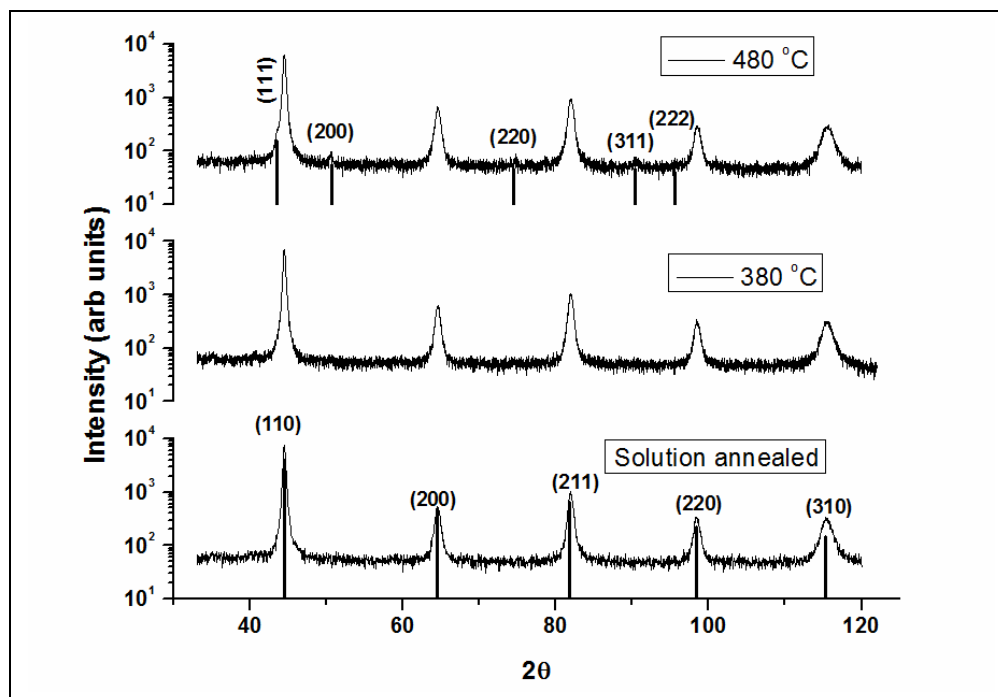


Fig. 4.5. X-ray diffractograms of 17-4PH samples aged for 0.5 h at 380 and 480 °C along with solution annealed sample

#### 4.2.1 Size-strain analysis in 17-4 PH steel

The WH plots (based on eqn. 2.11, p.30) and mWH plots (based on eqn. 2.23, p.36) for specimens aged for 0.5 h at 380 and 480 °C (653 and 753 K) conditions are shown in Fig. 4.6a and b respectively. It is clear from Fig. 4.6a that the WH plot shows anisotropic order dependent broadening. This feature was observed for all the specimens used in the study. Hence, mWH plots (Fig. 4.6b) have been made for all the specimens and the normalized mean square strain ( $\alpha$ ) and crystallite size have been estimated from the slope and

intercept of these plots. The observed linear fit for all the specimens showed a  $\bar{R}^2$  value of 0.98 or better. The observed linear fit shows that there is no local variation of dislocation density and hence makes the variable  $O$  of eqn. 2.23 small [20]. Such linear behaviour has also been reported in ball milled iron powder [80] and in aged Maraging steel specimens [32]. The observed variations in normalized mean square strain ( $\alpha$ ) and crystallite size with ageing temperature are shown Fig. 4.7 (a) and (b) respectively.

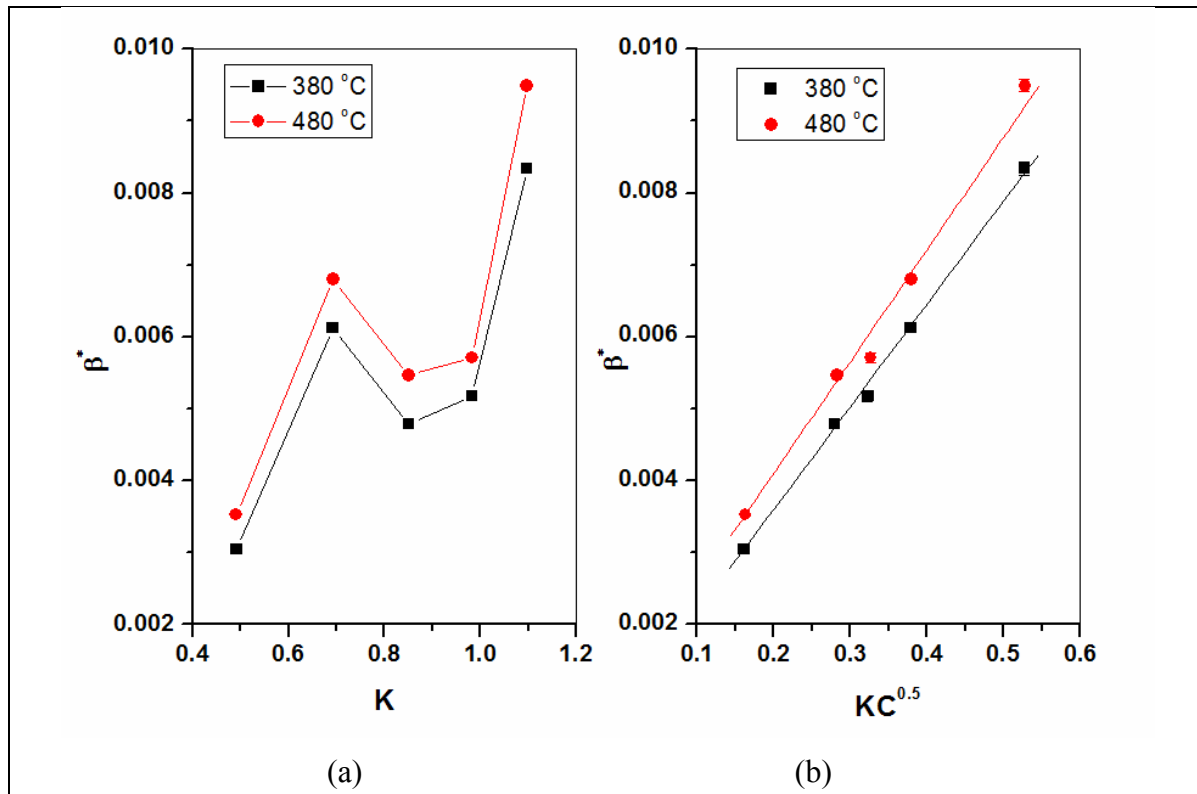


Fig. 4.6. (a) WH plot and (b) modified WH plot for the samples heat treated for 0.5 h at 380 and 480 °C (the axis in units of  $\text{\AA}^{-1}$ )



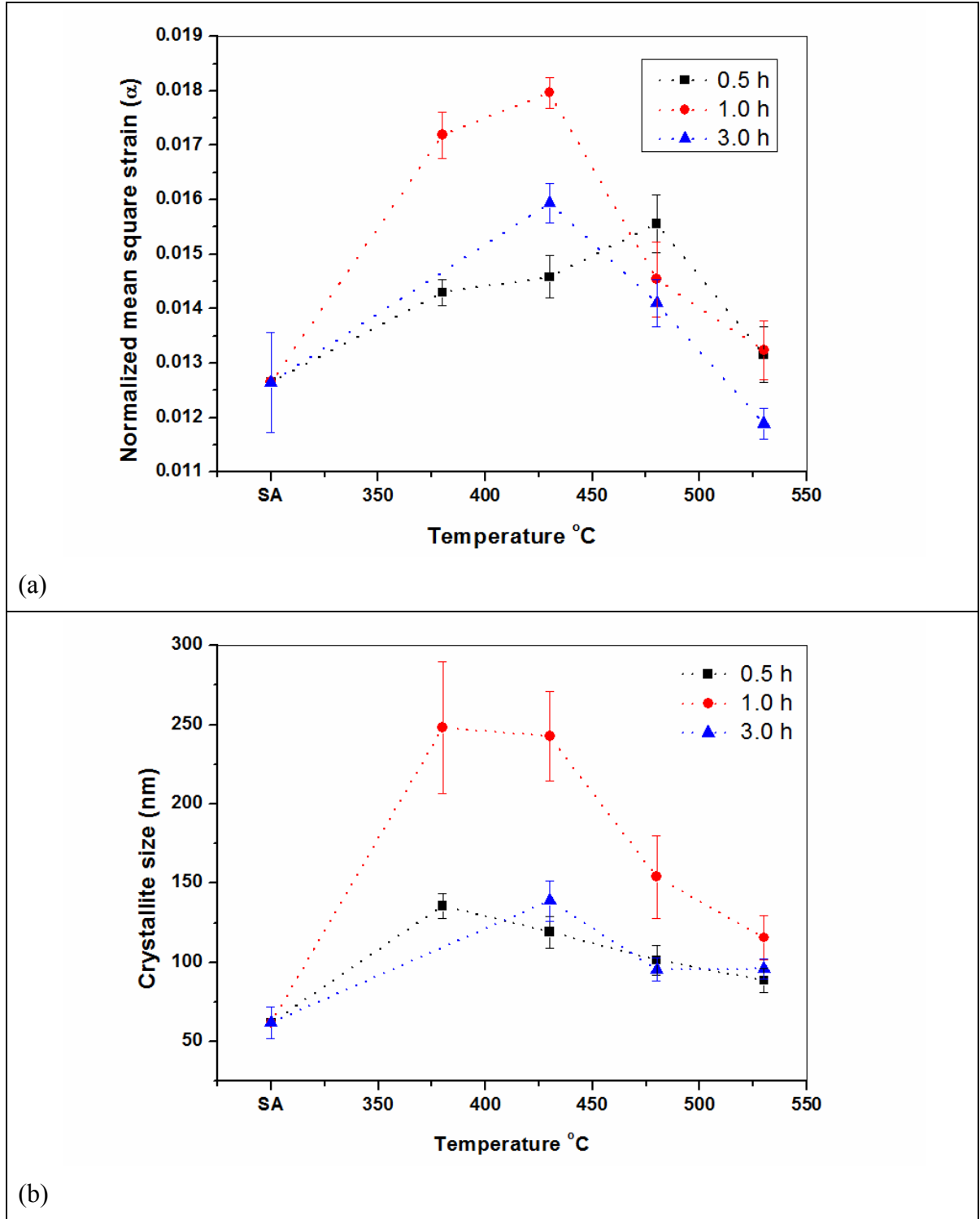


Fig. 4.7. Variation of (a) normalized mean square strain and (b) crystallite size with temperature in isochronally aged samples of 17-4 PH SS for different durations of 0.5, 1 and 3 h.

#### 4.2.1.1 Ageing for 0.5 h

From Fig. 4.7a, it is clear that the normalized mean square strain ( $\alpha$ ) increases as the temperature is increased from 380  $^{\circ}\text{C}$  (653 K) and reaches a peak value at 480  $^{\circ}\text{C}$  (753 K).

It is to be noted that annihilation of dislocations and precipitation occurs simultaneously on ageing. The initial precipitation starts with the formation of copper rich zones with bcc structure which is coherent with the matrix [27]. Supersaturated copper precipitates during ageing at lower temperature, as the incubation period for precipitation is insignificant in this steel [28]. Hence, the increase in  $\alpha$  is attributed to the precipitation induced strain in the matrix. On further increasing the temperature to 530 °C (803 K),  $\alpha$  decreases to a value of 0.0132 which is close to the value of 0.0126 obtained for the solutionized sample. This indicates that the precipitates have become incoherent with the matrix. The apparent crystallite size increased from the lowest value of 60 nm in the solution annealed condition to 130 nm at 380 °C (653 K) for ageing duration of 0.5 h. The smaller crystallite size obtained in solutionized condition is consistent with the high density of dislocations reported in the solutionized condition [35,39]. However, on subsequent increase in temperature, the crystallite size decreases continuously to a value of ~100 nm at 530 °C (803 K). The observed decrease will be discussed in the following section (§4.2.1.2).

Several authors inferred early precipitation of copper in these steels using change in hardness and conductivity [28,35]. Miller et al. [37] successfully observed copper precipitates in specimen aged at 482 °C for 1h aged using TEM. At this ageing temperature, though precipitates were not detected in specimen aged for 0.5 h by TEM, they were successful in detecting copper precipitates using field ion microscopy. Similarly, Viswanathan et al. [28] also reported copper precipitates using TEM in a specimen aged for 2 h at 499 °C. In the present investigation, the initial increase in  $\alpha$  (after ageing at 380 °C for 0.5 h) is attributed to the formation of coherent precipitates in the matrix which is in agreement with hardness change, as shown Fig. 4.1. This shows that changes in normalized mean square strain can be used to detect early precipitation.

#### 4.2.1.2 Ageing for 1 h

On ageing the specimens for 1 h at various temperatures, it is seen from Fig. 4.7a that the  $\alpha$  peaks at 430 °C (703 K). As the temperature is increased to 480 °C (753 K),  $\alpha$  decreases significantly from 0.018 to 0.0145. The reduction in the microstrain occurs when the precipitates become incoherent with the matrix. Hence, the reduction in the microstrain is analyzed from theoretical considerations. It is known that, above a critical precipitate radius  $R \approx b/3|\varepsilon|$ , the Orowan mechanism becomes operative and the precipitates become incoherent [49]. Herein,  $\varepsilon$  and  $\mathbf{b}$  represent the misfit strain and Burgers vector respectively. When the microstrain reaches a maximum value of 0.018, the estimated radius of copper precipitates is  $\sim 4.7$  nm. Hence, it is inferred that under peak microstrain conditions (aged at 430 °C (703 K) for 1 h), the precipitates are coherent and with subsequent reduction in microstrain, the coherency between the matrix and the precipitate is partially lost.

It is also known that the lattice misfit  $\delta$  is given by [99]

$$\delta = \frac{2(a_{ppt} - a_{mat})}{(a_{mat} + a_{ppt})}$$

where  $a_{mat}$  and  $a_{ppt}$  are the lattice parameters of the matrix and the precipitate phase respectively. The lattice parameter of bcc Cu reported in A710 type steel is 2.96 Å [100]. This value has been used in simulations [101]. The solution annealed specimen of 17-4 PH used in this study has a lattice parameter of 2.88 Å which gives a misfit value of 0.027. It is to be noted that the misfit and misfit strain are also related with  $\varepsilon \sim 2/3\delta$  [102] which gives a  $\varepsilon$  value of 0.018. The maximum normalized mean square strain,  $\alpha$  estimated in this study is 0.018. It is to be noted that the microstrain estimated would include some contributions from the dislocations present in the material. An  $\alpha$  value of 0.0126 is

estimated in solutionized condition. The difference in the microstrain between peak strained condition and solutionized condition is 0.0054. In previous studies [103,104], a value of 0.0057 has been used as the misfit strain assuming that the precipitates contain 1/3 of Fe and 2/3 of Cu. An analysis of misfit strain values used in Cu added steels was done by Isheim et al. [105] and they found that values in the range of 0.032 to 0.003 have been used in various studies. Hence, the microstrain estimated herein is consistent with the above studies. It is to be noted that a hardness of 435 VHN is measured under peak microstrain conditions. The hardness decreases marginally to 431 VHN from 435 VHN on increasing the temperature to 480 °C (753 K).

On ageing for 1 h at 380 °C (653 K), the crystallite size increases to 250 nm and remains almost same at 430 °C (703 K) as seen from Fig. 4.7. Ungar had reported that the crystallite size estimated from bulk specimens including ferritic/martensitic steels is closer or almost equal to the subgrain or dislocation cell size [106]. Hence, to confirm these changes, microstructural studies using SEM were carried out. SEM images of the specimens heat treated for 1 h at various temperatures along with the solution annealed specimen are shown in Fig. 4.8. The specimen details are marked below the figure.

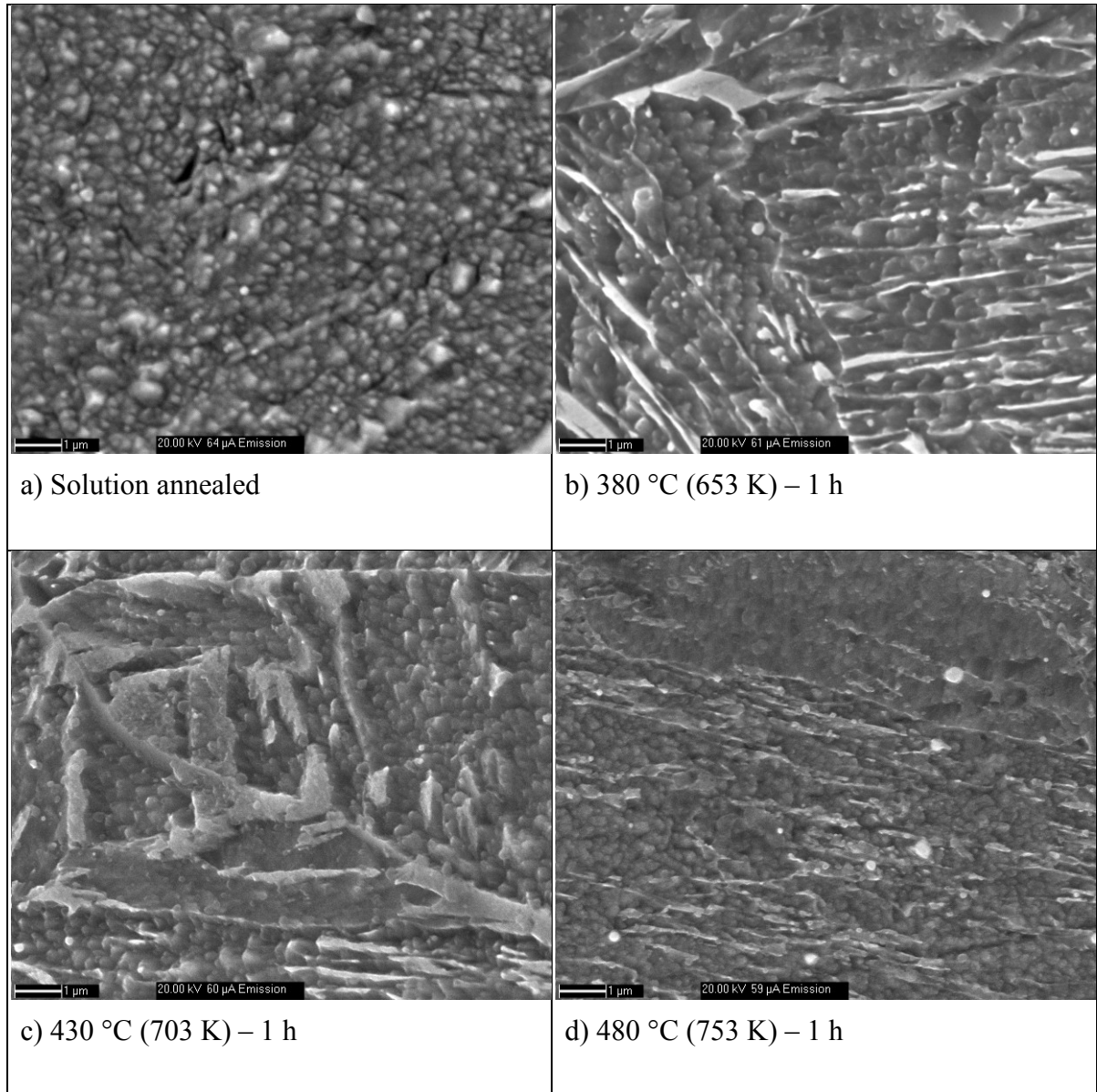


Fig. 4.8. SEM images of samples aged for 1 h at different temperatures along with solution annealed sample.

The microstructure of the solutionized steel consists of lath martensite with size ranging from 300 to 1000 nm. The misorientation of lath boundary is known to be  $\sim 5^\circ$  or lower. As a result, the microstructural changes within the lath could not be revealed when the specimen is perpendicular to the primary beam. Hence, specimens were oriented at an angle of  $18^\circ$  to reveal the underlying microstructure. From Fig. 4.8b and Fig. 4.8c it is clear that there is an increase in the size of the subgrains from the solutionized condition to the aged condition (380 and 430 °C for 1 h). However, on subsequent ageing at higher

temperature (480 °C), refinement takes place which is evident from Fig. 4.8d. The observed microstructural changes are in qualitative agreement with the crystallite size estimated from the peak profile analysis, as shown in Fig. 4.7b. The increase in the crystallite size with ageing time at lower temperature is attributed to annihilation of dislocations. Similar increase in crystallite size on initial ageing of maraging steel for 0.25 h at 482 °C (755 K) has been observed [32].

The observed decrease in crystallite size at higher temperatures is due to the competing mechanisms of annihilations of dislocations (which would increase the crystallite size) and other mechanisms which would lead to a decrease in crystallite size. It is to be noted that at higher temperature, the precipitation process gets accelerated due to increased diffusion, however, the matrix can accommodate more of the Cu at this temperature due to higher solubility, leading to a complex behaviour. The possible alternative mechanisms which would lead to grain refinement are sub-boundary pinning by dislocations or due to the formation of misfit dislocations which would be reflected as a decrease in subgrain size. Ghosh et al. [93] studied the effect of Cu precipitation in thermomechanically processed low carbon microalloyed steel. They found that the softening process during ageing is significantly reduced by the sub-boundary pinning caused by the Cu precipitates. Hwang et al. [107] studied the effect of direct quenching on the microstructure of copper-bearing high-strength alloy steels. They also found the effect of sub-boundary pinning due to precipitates of Cu. Huang et al. [108,109] studied the influence of different initial amounts of Mn (0.4 and 1.0 wt%) on the softening behaviour of Al–Mn–Fe–Si alloys using conductivity, hardness and electron backscattered diffraction measurements. Their study showed that precipitation in presence of fine dispersoids influences the recrystallization behaviour of this material. They concluded that the effect of preexisting dispersoids (or formed by concurrent precipitation) had an impact on the size of the matrix crystals by

providing a pinning effect. It is also known that, when the precipitates become partially coherent (semicoherent) as seen by the reduction in microstrain, some interface dislocations may form, leading to apparent reduction in crystallite size [50]. It is observed that, under the ageing conditions being discussed (480 °C and 1 h), there is a reduction in microstrain as shown in Fig. 4.7a. Hence, it is possible that the misfit dislocations which form lead to an apparent decrease in subgrain size. Rozenak [110] had suggested misfit dislocations at the semicoherent interfaces in Si structures. In M250 grade maraging steel, on ageing for 40 h (peak hardness condition), increase in positron life time has been observed which was attributed to the misfit dislocations arising from the incoherent nature of the precipitates by Rajkumar et al. [111]. In maraging steel, peak microstrain was observed on 10 h of ageing [32].

#### *4.2.1.3 Ageing for 3 h*

The variation of normalized mean square strain with temperature shows that  $\alpha$  peaks at a ageing temperature of 430 °C (703 K). On increasing the temperature, the microstrain decreases continuously and reaches a value of 0.0119 which is lower than the value obtained in the solutionized condition. The peak microstrain observed at 430 °C (703 K), is lesser than the value observed in peak microstrain condition (aged for 1 h at 430 °C). The lower microstrain in this condition leads us to conclude that the precipitates are incoherent with the matrix. Similarly, the crystallite size increases on ageing at 430 °C (703 K), but decreases with further increase in temperature. The decrease in the crystallite size has been explained in the earlier §4.2.1.2.

#### **4.2.2 Influence of coherency strain on hardness**

In the present study, a peak hardness of 460 VHN is observed on ageing for 3 h at 430 °C (703 K). The peak microstrain is seen on ageing for 1 h at 430 °C (703 K). Similar

behavior is reported while ageing M250 grade maraging steel at 482 °C [32] and these results would be discussed in the following Chapter. In maraging steel, hardness peak is reported after 40 h of ageing while the microstrain peaked at 10 h of ageing. These results can be understood from the fact that the precipitation process (growth) completes much ahead of peak hardness which is similar to the modeling results reported by Guo et al. [31]. Subsequent growth is attributed to coarsening which minimizes the interfacial energy leading to incoherency and reduction in microstrain. Similarly, hardness decreases on further ageing as discussed in §4.1.2.

Based on the results presented here, a preliminary attempt is made to relate the observed increase in hardness with the microstrain in the matrix. Hardness has been directly related to the flow stress by various authors [90,94]. The increase in the strength due to coherency has been shown to be proportional to  $\varepsilon^{3/2}(rf)^{1/2}$ , where  $r$  is the radius of the precipitate,  $f$  is the volume fraction of precipitate and  $\varepsilon$  is the misfit strain [49]. These authors had suggested that  $\varepsilon$  would reduce with smaller size particles as the thickness of the interface plays a significant role. Since the change in misfit strain ( $\varepsilon$ ) with size of precipitates is reflected in the normalized mean square strain ( $\alpha$ ), this variable, determined from mWH, is used to link with the hardness. Hence, a plot of  $\alpha^{3/2}$  vs Hardness (with ageing condition marked as legends) is shown in Fig. 4.9. It is to be noted that the 2 points which lie away from the linear fit are the one hour aged specimens wherein the crystallite size had increased significantly as discussed earlier. All the specimens aged for 3 h at different temperatures were shown to be in incoherent in §4.2.1.3. Hence these specimens were excluded from the analysis. The plot given in Fig. 4.9 shows a clear dependence of the increase in strength due to coherency strains. For correctly estimating the magnitude of increase in strength due to coherency hardening requires values of radius of precipitates



and fraction of precipitates which would be presented in the following section after estimating the fraction and radius of precipitates.

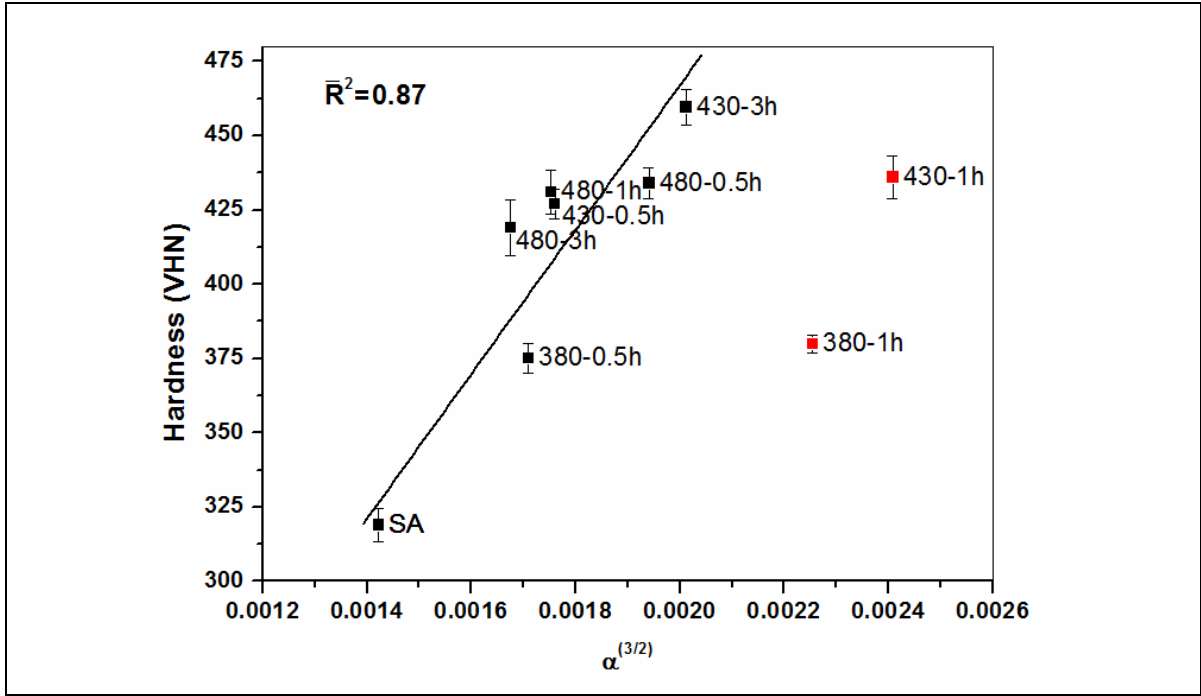


Fig. 4.9. Variation of Hardness with  $\alpha^{3/2}$

#### 4.2.3 Variation of microstrain with tempering parameter

The hardness in the overaged regime correlated well with tempering parameter, as explained in §4.1.3. Similarly, as explained in §4.2.2, the strain in the matrix due to precipitation had an impact on the strength which was reflected in the hardness. Hence, to correlate the normalized mean square strain ( $\alpha$ ) measured at different ageing temperatures and times, a plot of  $\alpha$  with tempering parameter is shown in Fig. 4.10. In this figure, the  $\alpha$  values in the regime when the precipitates are coherent are shown as open squares and in the incoherent regime as filled squares. Similar to hardness, the sample with peak microstrain is included in the fit. It is clear from Fig. 4.10 that the 3 points excluded from the fit correspond to specimens which have not crossed the peak microstrain conditions. This aspect can be verified by looking at Fig. 4.7a. All the excluded points in Fig. 4.10 lie on the rising part of Fig. 4.7a. A linear fit is obtained for all the specimens that have

crossed the “peak microstrain” condition, as shown in Fig. 4.10. This indicates that the precipitate coarsening is the dominant factor. Hence, the analysis presented above clearly demonstrates that the observed change in microstrain in the overaged regime can be effectively linked with the tempering parameter. *It would be worthwhile to validate this linear behaviour in the future by studying other precipitation hardenable materials wherein the softening mechanism may be different.*

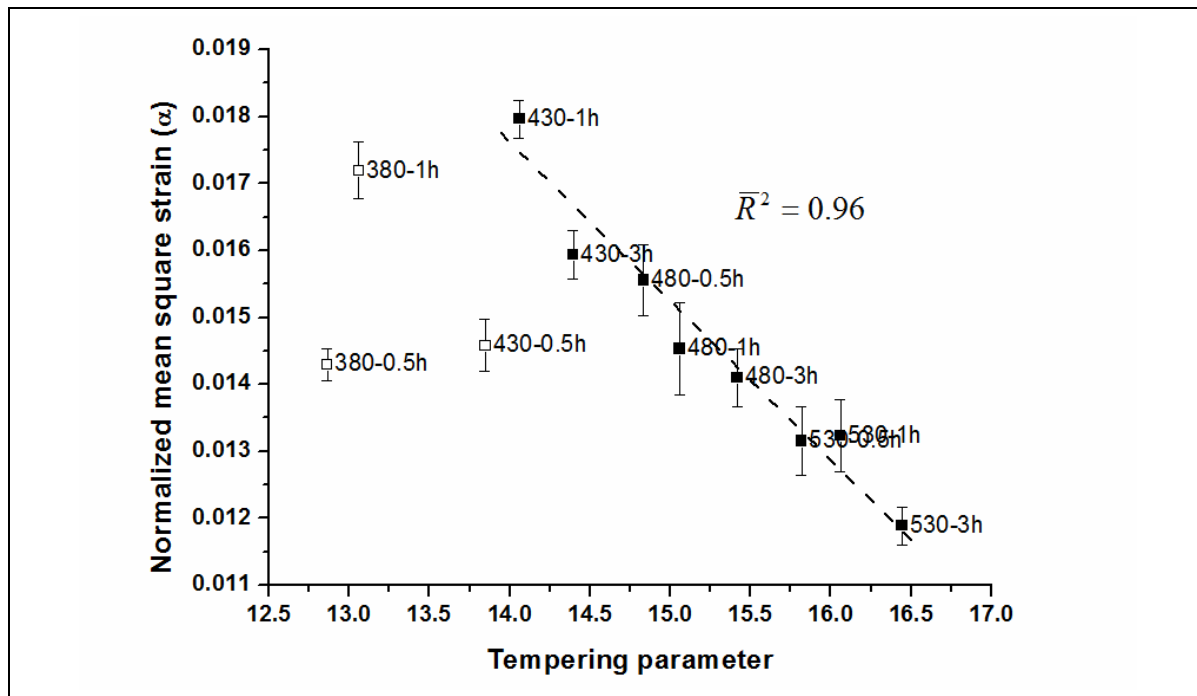


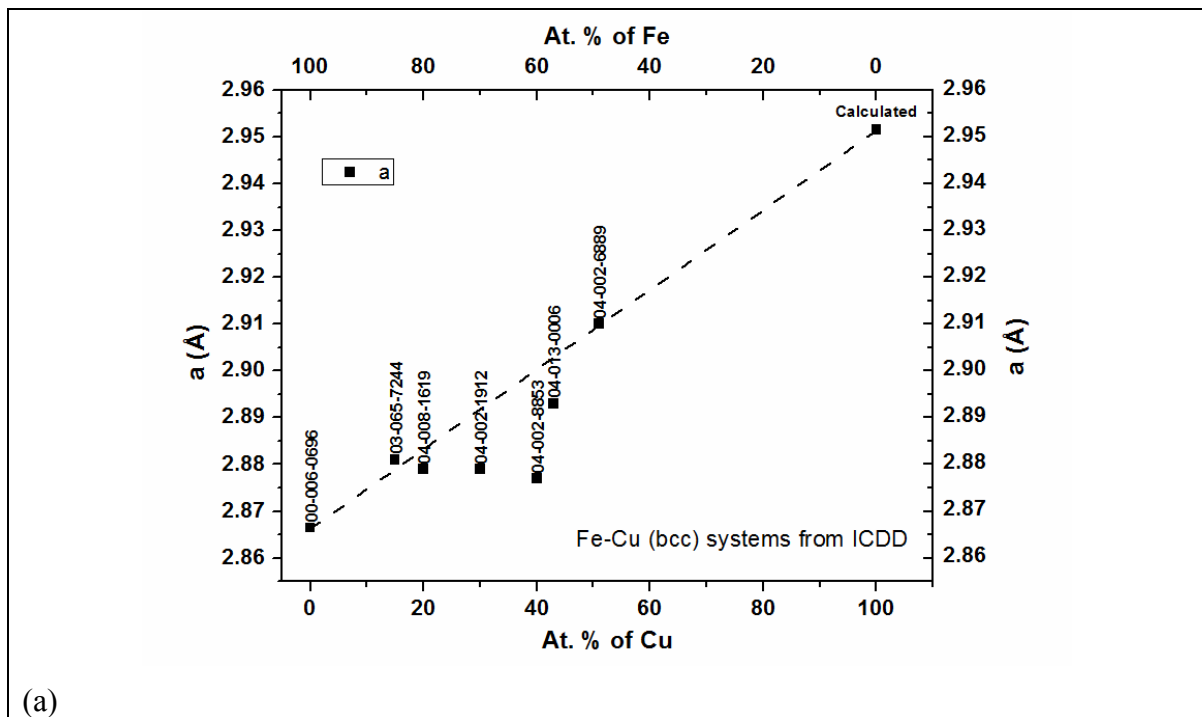
Fig. 4.10. Variation of mean square strain with tempering parameter

### 4.3 Determination of precipitate fraction

#### 4.3.1 From changes in lattice parameter

The literature presented in §1.4 showed the applicability of using changes in lattice parameter for determining precipitate fraction. Based on the distance of closest approach determined in fcc structure, the calculated lattice parameter ( $a$ ) of bcc Cu and bcc Ni are 2.9516 Å and 2.8772 Å respectively. From these values of ‘ $a$ ’, the volume occupied by these atoms in a unit cell of bcc structure are 1.28575E-29 and 1.19088E-29 m<sup>3</sup>/cell for Cu and Ni respectively. The value of 1.09389E-29 m<sup>3</sup>/cell for Ni used by Guo et al. [26] is

based on the volume arrived at considering the fcc structure. For validating the distance of closest approach for determining lattice parameter and thereby arriving at volume occupied by atoms in crystals, a survey of Fe-Cu and Fe-Ni binary systems with bcc structure is carried out. The lattice parameters of Fe-Cu and Fe-Ni binary systems are collated from Powder Diffraction Files (PDF) available from International Centre for Diffraction Data – ICDD and shown in Fig. 4.11a and b respectively. A straight line is drawn between the lattice parameter of pure Fe and calculated  $a$  value of pure bcc Cu and bcc Ni and is shown in Fig. 4.11a and b respectively. The data presented in Fig. 4.11 shows that deviations from Vegard’s law exist, which are similar to that reported by Teng et al. [112].



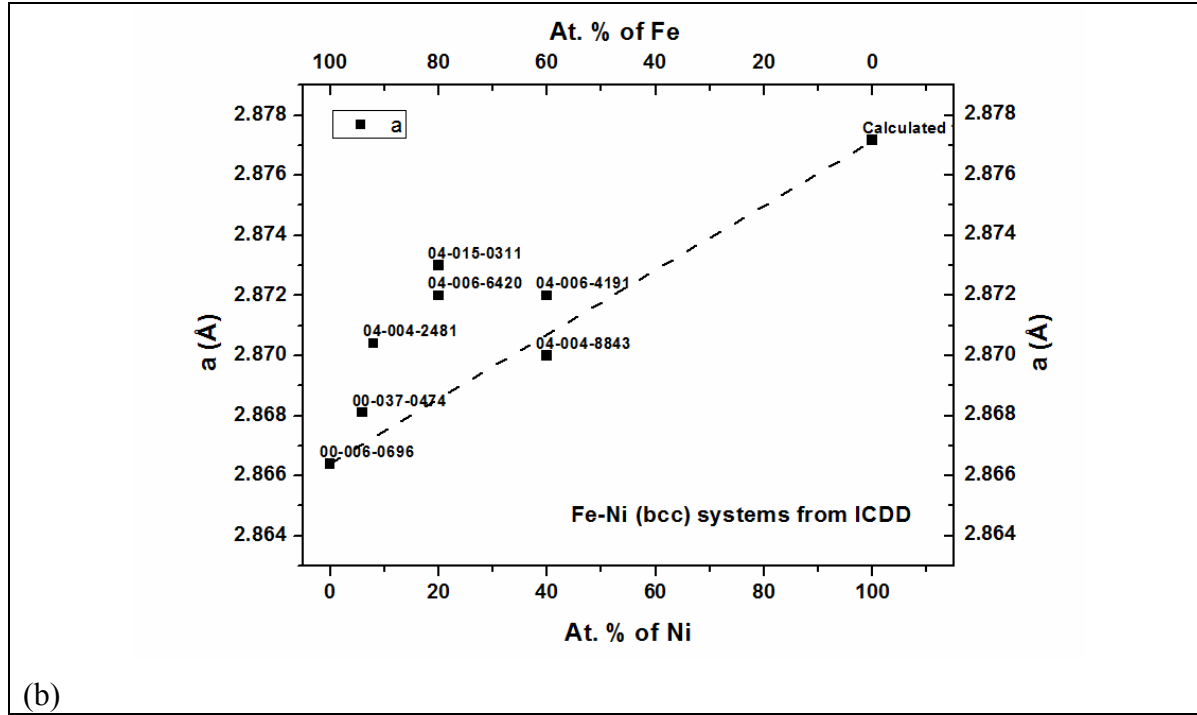


Fig. 4.11. Variation of lattice parameter of (a) Fe-Cu bcc alloys with Cu concentration and (b) Fe-Ni bcc alloys with Ni concentration based on ICDD data (The legends indicate the Powder diffraction file available from ICDD)

The volume/unit cell of each of the major alloying elements present in 17-4 PH steel is presented in Table 4.1. From the values of volume given in Table 4.1 along with the volume of Cu and Ni mentioned in the previous paragraph, a lattice constant of 2.8774 is estimated. The measured lattice parameter of 17-4 PH steel in solutionized condition is  $2.8807 \pm 0.0007$ . The lattice parameter is underestimated by  $0.0033 \text{ \AA}$  by this approach. However, a detailed calculation by Teng et al. [112], overestimated the lattice parameter by  $0.0025 \text{ \AA}$  in NiAl precipitate strengthened Fe-based alloy. A reduction in the lattice parameter of 17-4 PH steel is expected due to the precipitation of Cu. The change in the  $a$  value of the matrix due to depletion of Cu, gives a slope of  $da/dx$  of  $-7.9714\text{E-}4 \text{ \AA/at\%}$ . This value is very close to the  $\Delta a$  of  $7.2\text{E-}4$  computed theoretically by Harry and Bacon [101]. The precipitate fraction is estimated by multiplying the slope ( $da/dx$ ) with the difference in lattice parameter at different ageing conditions with that of the lattice parameter in solutionized condition ( $a_{SA}$ ). It is to be noted that 2 atoms of Cu are required

to form an unit cell of bcc precipitate and hence the precipitate fraction is half the atom fraction. This approach of estimating precipitate fraction is valid if no other precipitates form by depleting the matrix. In 17-4 PH steel, Cu precipitation has been the main source of strengthening. However in some studies presence of NbC has been reported [39] in the solution annealed condition. Kobayashi et al. [113] studied the effect of Nb addition on Cu precipitation in ferritic steels and it was shown that Nb addition only delays the nucleation of Cu rich zones. Nb has lower diffusivity in Fe matrix and Nb contributes to the solid solution strengthening of these steels. Nb enriched precipitates were observed at higher ageing temperatures than those considered in this study [113,114]. Hence the influence of NbC formation on lattice changes is neglected in this study.

Table 4.1 Volume of major alloying elements present in 17-4 PH steel

Element	Volume (m <sup>3</sup> /cell)	PDF card from ICDD
Fe	1.17755E-29	00-006-0696
Cr	1.19925E-29	00-006-0694
Nb	1.80175E-29	00-034-0370
Si	2.0014E-29	00-005-0565
Mn	1.22043E-29	00-032-0637

The lattice parameters of all the samples used in this study were estimated by Rietveld refinement. Due to ageing, reduction in the lattice parameter was observed. The estimated increase in precipitate fraction arrived at from lattice parameter changes for the three different temperatures is shown in Fig. 4.12. The plots show typical features of increase in precipitate fraction with ageing time. However, marginal increase in lattice parameter leading to a reduction in precipitate fraction is observed in samples aged for an hour at 430

and 480 °C. Similar observation was made by Holzer et al. [104] during their computer simulation of 1.4% Cu added steel. Their simulations showed that there is a region in which the total precipitate fraction decreases during ageing. This coincides with the reduction in the volume fraction of bcc Cu and initiation of formation of fcc Cu. A structural transformation of bcc to fcc Cu is reported. Increase in the phase fraction on 3 h ageing at 480 °C (marked as a circle in Fig. 4.12) is attributed to the fact that phase fractions have been calculated assuming a bcc structure (with 2 atoms), whereas a structural transformation to fcc (with 4 atoms) is well reported [35,104,115].

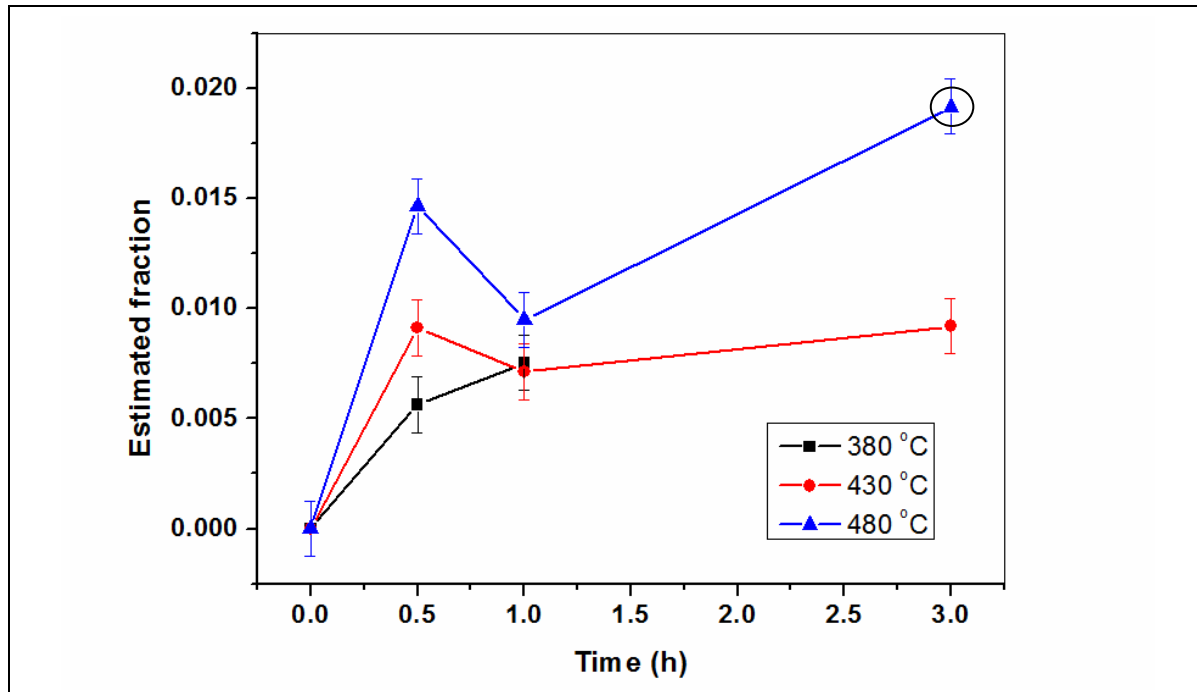


Fig. 4.12. Estimated precipitate fraction (from lattice parameter changes) as a function of ageing time at different temperatures

#### 4.3.2 From hardness measurements

In order to compare the estimated precipitation fraction from changes in lattice parameter, an alternative approach is followed. In the age hardening regime, the precipitation kinetics has been studied from changes in hardness and the results were presented in §4.1.1. The hardness measured at each of the ageing temperatures and durations is normalized with the peak hardness of 459 VHN achieved on ageing at 430 °C for 3 h. It is also known that the

same peak hardness will not be achieved at each of the temperatures. This approach has been used for estimating the precipitate fraction, thereby determining the Avrami exponent and activation energy of the precipitation process by various authors [90,94]. The observed variation in precipitate fraction with ageing time at different temperatures is shown in Fig. 4.13. The curves show typical age hardening characteristics at each of the temperatures. The sample aged at 480 °C for 3 h shows lesser hardness indicative of over ageing (marked as a circle in Fig. 4.13). This is consistent with the structural transformation of the precipitate to fcc as discussed at the end of §4.3.1.

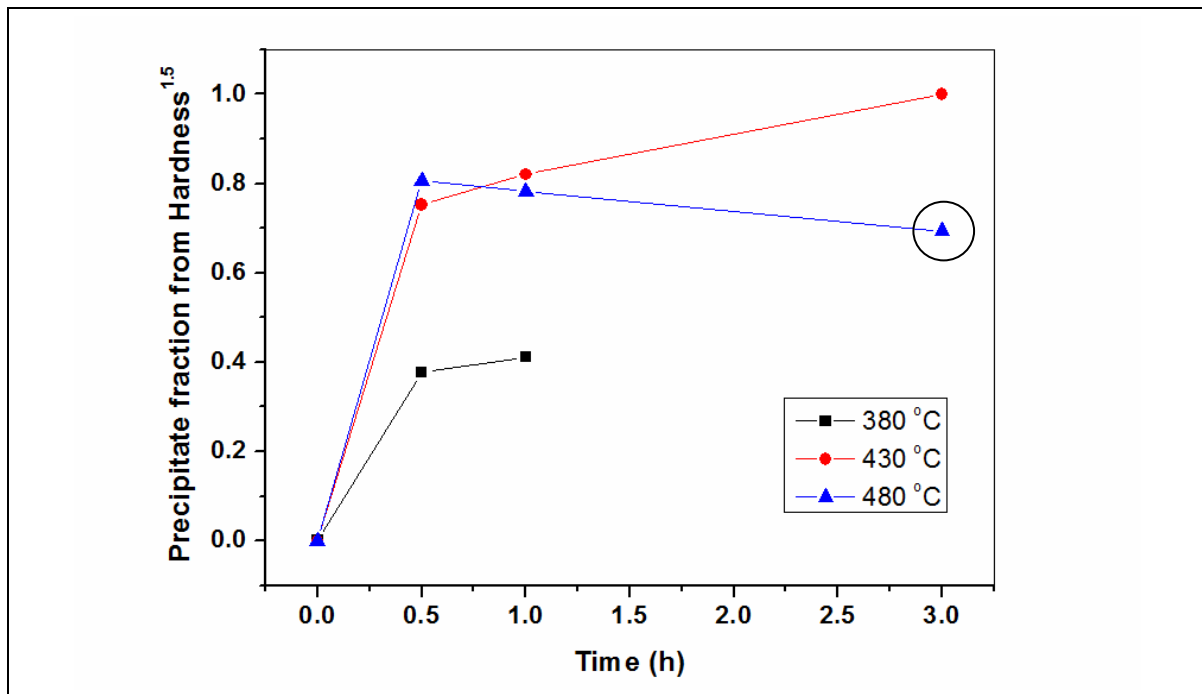


Fig. 4.13. Variation of precipitate fraction estimated from  $\text{Hardness}^{1.5}$  with ageing duration at different temperatures

#### 4.3.3 Comparison of precipitate fractions

The precipitate fractions determined from changes in lattice parameter are in the absolute scale. However, the precipitate fraction obtained from hardness changes are in relative scale and has been normalized to 1. Ideally, both the approaches should lead to same results. This is achieved when the precipitate fraction determined from hardness is normalized to a peak fraction of 0.013, which is close to the peak precipitate fraction

observed from changes in lattice parameter. Table 4.2 shows the precipitate fractions determined from changes in lattice parameter and hardness along with the difference between them.

The difference between the precipitate fraction (0.004) estimated by both the approaches is more at 480 °C (0.5 h). In this condition, the precipitate fraction estimated from the lattice changes is the maximum. The deviation could arise from two possibilities. At this temperature, the kinetics would be faster leading to higher fraction of precipitates. An increase in precipitate fraction when the precipitates are in bcc structure is also reported [104]. Alternatively, the precipitate fraction estimated from changes in hardness could be underestimated. This is a distinct possibility considering the fact that precipitate fractions have been obtained by normalizing with the peak hardness of 459 VHN achieved at 430 °C (3 h). At, 480 °C (0.5 h), the hardness is 434 VHN, which could be the start of overageing at this temperature.

Table 4.2 Precipitate fraction determined from the two approaches and their difference

Ageing condition Temperature - duration	Precipitate fraction from changes in lattice parameter ( $\pm 0.00125$ max)	Precipitate fraction from changes in hardness	Difference
380 °C – 0.5 h	0.0056	0.0049	0.0007
380 °C – 1 h	0.0075	0.0054	0.002
430 °C – 0.5 h	0.0091	0.0098	-0.0007
430 °C – 1 h	0.0071	0.0106	0.0035
430 °C – 3 h	0.0092	0.0126	-0.0034
480 °C – 0.5 h	0.0147	0.0105	0.004
480 °C – 1 h	0.0095	0.0102	0.0007



## 4.4 Precipitation strengthening of 17-4 PH steel

### 4.4.1 *Strengthening in Fe-Cu alloys*

Increase in strength of 17-4 PH steel during ageing is attributed to the precipitation of fine copper particles. Similarly, strengthening behaviour of Fe-Cu alloys by Cu precipitates has been studied experimentally and theoretically by various authors [51,92,101,103,104,115,116]. The strengthening of  $\alpha$  iron by a softer phase like Cu was attributed by Hornbogen and Glenn [92] to the following possibilities: coherency stresses in the matrix due to the particles, energy necessary to shear the particles or to the spacing between the particles. Russel and Brown [51] proposed a model to estimate the yield stress, considering the interaction between a slip dislocation and a precipitate with a lower shear modulus than that of the matrix. This model was applied to iron-copper system with Cu up to 4% and was able to explain the observed increase in strength with volume fraction of precipitates. Harry and Bacon [101,116], from their computer simulations of strengthening of bcc-iron with copper precipitates, concluded that the strengthening is due to the effect of screw dislocation core on bcc Cu structure of the precipitate rather than the elastic interaction. This interaction causes the bcc Cu structure to change to a close packed structure. Fine and Isheim [103] considered the contributions of various strengthening mechanisms like misfit strengthening, chemical strengthening, modulus difference strengthening and dislocation core-precipitate interaction strengthening. The change in the screw dislocation core energy as the dislocation traverses the precipitate was seen as a major cause of strengthening similar to that reported by Harry and Bacon [116]. However, they also felt that the accuracy of the interatomic potentials is limited and further theoretical work is required to conclude about the active strengthening mechanism. Holzer and Kozeschnik [104] carried out computer simulations taking into account the variable nucleus composition that occurs during early precipitation. They found that the

coherency strain and modulus strengthening effects contribute to the precipitation strengthening. Together with intrinsic strength of the matrix and solid solution strengthening contribution, they were able to qualitatively compare the calculated and experimental results of lower yield strength of Fe-1.4% Cu alloy. Recently, Takahashi et al. [115] considered the strengthening mechanisms in Fe-1.4% Cu steel and studied the same by atom probe tomography. They studied the effect of particle diameter on the interaction force of a dislocation with an obstacle. From this, they concluded that the main mechanism of particle strengthening is due to the difference in the elastic modulus of the particle and the matrix.

#### **4.4.2 *Strengthening studies in other alloys***

The above studies were on steels with Cu as the only major alloying element. However, 17-4 PH steel has many alloying elements, notable among them being Cr and Ni in addition to Cu. Seetharaman et al. [102] studied the precipitation hardening behaviour of PH 13-8 Mo SS. They considered the contributions of various strengthening mechanisms like coherency, modulus and order strengthening and estimated that the increase in shear strength is due to the collective influence of these three mechanisms. Knipling et al. [117] studied the precipitation strengthening of binary Al-0.1Sc, Al-0.1Zr and ternary Al-0.1Sc-0.1Zr alloys and considered the various strengthening mechanisms. Their analysis of increase in yield stress of ternary alloy aged at three different temperatures was based on additive nature of the strengthening mechanisms. However, they proposed ‘order strengthening’ as the cause for the increase in strength. Hence, in the following sections, the strengthening mechanisms active in 17-4 PH steel would be analyzed. This would enable comparing the measured strength with theoretical estimates.

#### 4.4.3 Strengthening mechanisms

As discussed in the previous section, the increase in the hardness/strength on ageing is due to the combined effect of the intrinsic strength of the matrix and strengthening contributions from the finely dispersed precipitates in the matrix. The intrinsic strength of the matrix is due to the solid solution strengthening achieved from the constituent alloying elements present in 17-4 PH steel. The strengthening contribution of precipitates in this class of steel is due to the coherency strains (between the matrix and the precipitate) and the difference in modulus between precipitate and matrix. The theoretical formulation of these strengthening mechanisms is briefed further.

##### 4.4.3.1 Coherency strengthening

Coherency strengthening arises from the elastic coherency strains that exist surrounding a particle that does not fit in the matrix. Gerold and Haberkorn [49,118] estimated the increase in yield stress ( $\Delta\tau_{\text{coh}}$ ) caused by coherent precipitates and is given by

$$\Delta\tau_{\text{coh}} = \Phi G |\epsilon|^{3/2} \left( \frac{rf}{b} \right)^{1/2} \quad \text{-- ( 4.4 )}$$

where  $G$ ,  $\epsilon$ ,  $r$ ,  $f$  and  $b$  denote the shear modulus of the matrix, misfit strain, radius of the precipitate, volume fraction of precipitates and Burgers vector respectively. The constant  $\Phi$  depends on the type of the dislocation and a value of 6 has been used [119,50]. Considering the variation in  $\epsilon$  values reported in literature and discussed in detail in §4.2.1.2, p.57, it is felt that the experimentally measured normalized mean square strain can be used to estimate the coherency strengthening. Gerold et al. [49] clearly concluded that when the precipitates are of small size, the  $\epsilon$  may be different. Hence the normalized mean square strain estimated in this study would be used to evaluate the coherency strengthening, similar to the usage of  $\alpha$  to link with the tempering parameter.

#### 4.4.3.2 Modulus strengthening

The energy of a dislocation is a function of the shear modulus of the lattice in which the strain field of the dislocation exists, leading to a decrease or increase in energy as it passes through the particle (precipitate). The increase in strength ( $\Delta\tau_{\text{mod}}$ ) due to the difference in modulus between the precipitate and the matrix was given by Kelly [120] as

$$\Delta\tau_{\text{mod}} = \frac{\Delta G}{4\pi^2} \left( \frac{3\Delta G}{Gb} \right)^{1/2} [0.8 - 0.143 \ln(r/b)]^{3/2} (rf)^{1/2} \quad \text{-- ( 4.5 )}$$

where  $\Delta G$  is the difference in modulus between matrix and precipitate,  $G$  is matrix shear modulus,  $b$  is the Burgers vector,  $r$  is the radius of the precipitate and  $f$  is the volume fraction of the precipitate. A modulus of 77 GPa for the matrix and 48 GPa for the Cu precipitate were assumed [51,121,112].

### 4.5 Estimation of radius of precipitates

For theoretically determining the contributions of various strengthening mechanisms discussed above (as given in eqn. 4.4 and 4.5), the microstrain, precipitate fraction and radius of precipitates are the important variables required. The microstrain and fraction of precipitates have been estimated from XRD/LPA and the constants in these equations are available from literature. Determination of radius of precipitates especially in early stages requires atom probe or TEM investigations wherein the sampled volume is very small. The radius of precipitates can be estimated from Zener's theory of growth of spherical precipitates from solid solutions [122]. The growth of spherical precipitates follows the equation  $r = \alpha'(D't)^{0.5}$  where  $r$  is the particle radius after time  $t$ ,  $D'$  is the atomic diffusion coefficient at a given temperature and  $\alpha'$  is the growth coefficient which is a function of concentration and is taken as  $10^{-2}$  [92]. The temperature independent pre-exponential  $D_0$  is determined from the data available from literature while studying Cu

precipitation in  $\alpha$ -iron [92]. The diffusion coefficient,  $D'$  is dependent on the activation energy of the precipitation process. The activation energy for the precipitation process determined from hardness measurements is 143 kJ/mol as given in §4.1.2 [123]. The radius of precipitates estimated in each of the ageing conditions is shown in Table 4.3 along with microstrain, crystallite size and hardness.

Table 4.3 Estimated radius of precipitates, normalized mean square strain ( $\alpha$ ), crystallite size and Hardness at different ageing conditions

Ageing condition	Estimated radius from Zener's equation ( $\text{\AA}$ )	Normalized mean square strain from mWH approach (eqn. 2.23)	Crystallite size (D) of the matrix from mWH plot (eqn. 2.23) (nm)	Hardness (VHN) $\pm 5$ VHN
Solution annealed	Nil	0.0126	62	319
380 °C – 0.5 h	10	0.0143	136	375
380 °C – 1 h	14	0.0172	248	380
430 °C – 0.5 h	26	0.0146	119	427
430 °C – 1 h	36	0.0179	242	436
430 °C – 3 h	62	0.0159	139	459.5
480 °C – 0.5 h	59	0.0156	101	434
480 °C – 1 h	84	0.0145	154	431

It is necessary to evaluate the consistency of the theoretical estimates of radius with other experimentally measured parameters. Hence, a brief recap of the discussions presented in §4.2.1.2 (p. 57) is given first. From theoretical considerations, it is known that above a critical radius ( $R \approx \frac{b}{3|\epsilon|}$ ) of the precipitate, the precipitates become incoherent [49]. As discussed earlier, a misfit strain value of 0.0179 gives a critical radius of 47  $\text{\AA}$ . Above this

radius, the precipitates are incoherent with the matrix. A closer analysis of the data presented in Table 4.3 shows that the microstrain is maximum when the radius is less than 47 Å. The peak hardness is observed when the radius is slightly larger than this value. This is consistent with the earlier findings [32,31] wherein it has been shown that growth of precipitates completes much ahead of peak hardness and subsequent growth is due to coarsening. This is also consistent with the marginal reduction in microstrain. The analysis presented above clearly shows that the radius of precipitates estimated is consistent with theoretical and experimental observations. However, it would be worthwhile to use the above estimated precipitate radius values to evaluate the strengthening contributions.

#### 4.6 Estimation of strengthening contributions

The strengthening mechanisms active in this class of steel have been discussed in §4.4.3. All the parameters required for estimating the contributions to coherency strengthening and modulus strengthening have been estimated and these can be linked to increase in strength observed on ageing. Hardness has been semiempirically linked linearly to flow stress by Tabor [124] and to shear modulus by Clerc and Ledbetter [125]. Hence an attempt is made to correlate the strengthening contribution directly with hardness. Since the precipitate fractions obtained from changes in lattice parameter and hardness were different, both the fractional estimates would be used to evaluate the strengthening contributions based on equations 4.4 and 4.5 (p. 73). The strengthening contributions can be added linearly or by pythagorean superposition [50,104]. Hence, the hardness ( $H$ ) at different ageing conditions is linked to the modulus and coherency strengthening contributions as

$$H = H_o + k_1 \sqrt{(\Delta\tau_{mod}^2 + \Delta\tau_{coh}^2)} \quad \text{-- ( 4.6 )}$$

where  $H_o$  is the intrinsic hardness arising due to the alloying elements and the quenched-in dislocations present in the steel under solutionized condition. The intercept of a plot between hardness and the strengthening contributions would yield  $H_o$  and the slope is  $k_I$ . The variation of the theoretically estimated strengthening contribution with hardness is shown in Fig. 4.14 and Fig. 4.15. In Fig. 4.14 the strengthening contributions have been estimated with precipitate fractions determined from changes in lattice parameter (as discussed in §4.3.1). Similarly, Fig. 4.15 depicts the strengthening contributions estimated with precipitate fractions obtained from hardness changes (as discussed in §4.3.2). The legends in these figures show the ageing condition of the sample. The linear fit obtained in each case and the adjusted  $\bar{R}^2$  values are shown in these figures. The correlation is better when the fractional estimates are obtained from hardness changes, as compared to the estimates from lattice parameter. The intercepts obtained in each case are  $311 \pm 23$  VHN and  $309 \pm 12$  VHN respectively which is close to the hardness of 320 VHN obtained in the solutionized condition. Similarly, the slopes are  $1.26e-6$  and  $1.36e-6$  with an error one order less. Though the estimated precipitate fractions showed minor deviations based on the approaches used to estimate them, the strengthening contributions and the constants determined are in good agreement with each other.

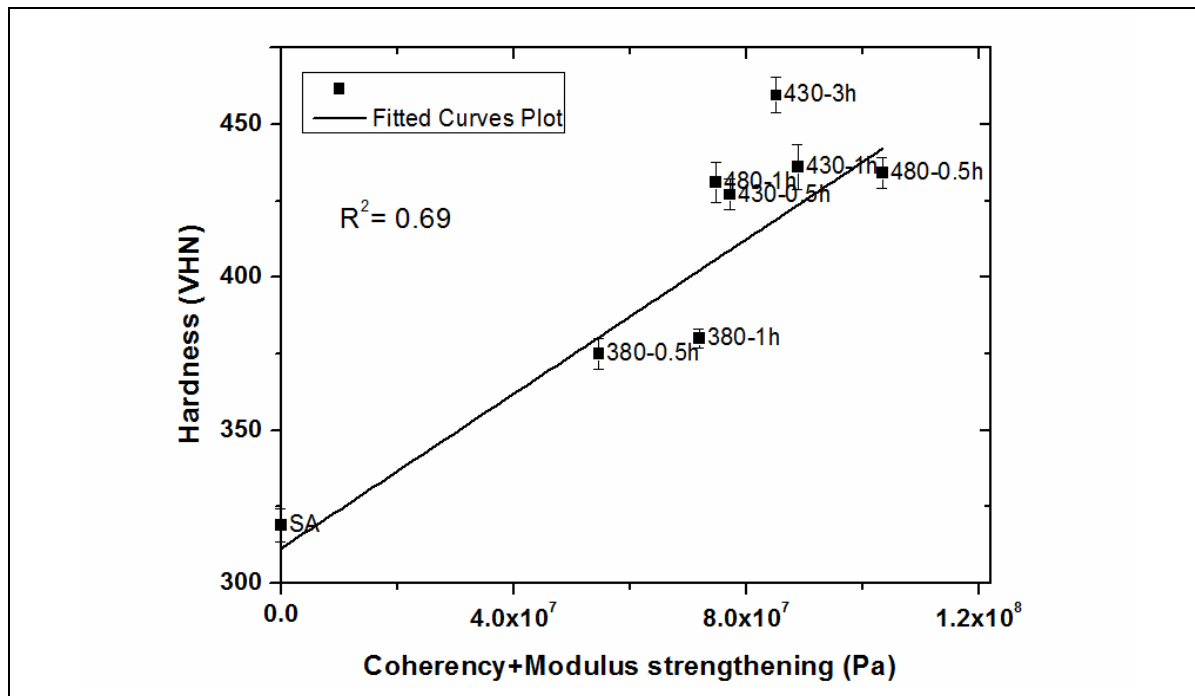


Fig. 4.14. Variation of hardness with coherency + modulus strengthening (precipitate fraction estimated from changes in lattice dimensions)

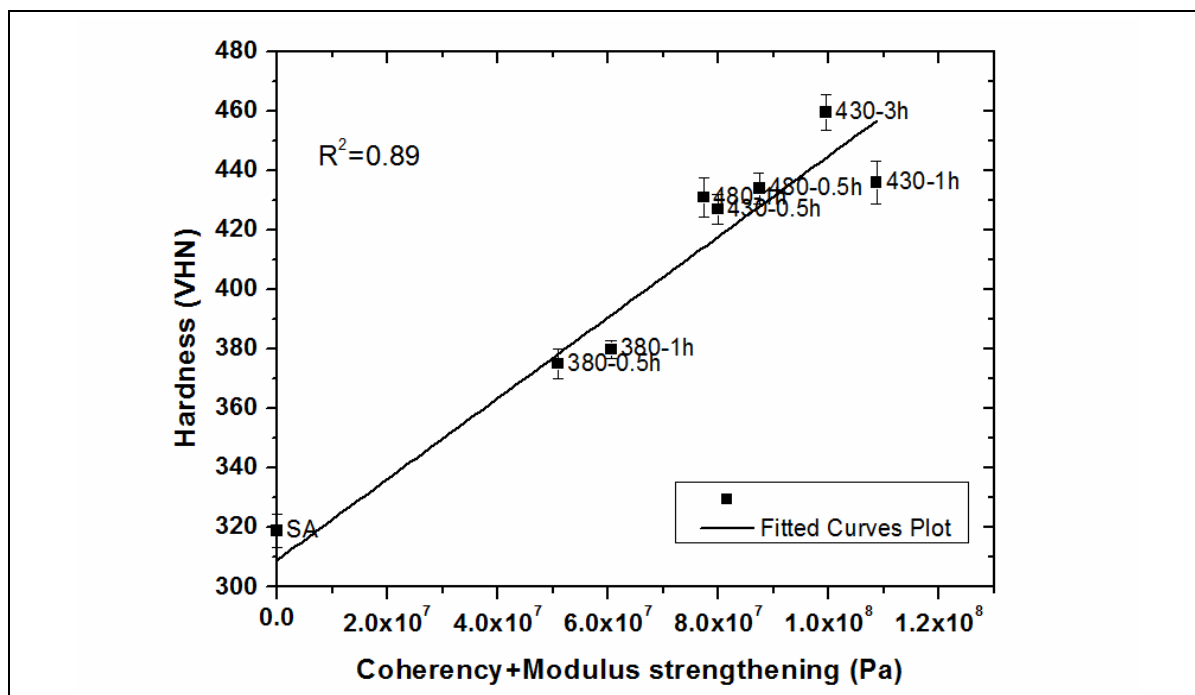


Fig. 4.15. Variation of hardness with coherency + modulus strengthening (precipitate fraction estimated from changes in hardness)

It is well known that during ageing, microstructural changes take place with annihilation of dislocations causing increase in crystallite size and refinement of substructure at elevated temperatures [50,123]. The observed changes in crystallite size with ageing have



been well explained in §4.2.1.2. Hence, the contribution to strengthening arising from changes in grain size caused by the microstructural changes should also be included. The effect of grain size on strengthening is well related by the Hall-Petch equation. Hence, eqn. 4.6 (p. 76) is modified by incorporating the effect of grain size ( $d$ ) on strengthening and the variation in hardness is given by

$$H = H_o + k_1 \sqrt{(\Delta\tau_{mod}^2 + \Delta\tau_{coh}^2)} + k_H d^{-1/2} \quad \text{-- ( 4.7 ).}$$

Herein,  $k_H$  is the Hall-Petch constant (in hardness scale) and  $k_1$  is a constant to the strengthening term. A least square refinement of the planar equation would yield the constants  $H_o$ ,  $k_1$  and  $k_H$ . In martensitic steels, the accepted measure of grain size is the size of the crystallographically coherent block, which is the packet size or block size [126]. Ungar et al. [127] had reported that the crystallite size estimated in ferritic/martensitic steels is closer or almost equal to the subgrain size. Hence, the crystallite size  $D$  estimated from XRD/LPA based on equation 2.23 (p. 36) has been used as the size in equation 4.7 (p. 79). The variation of hardness with contributions from strengthening due to precipitates (term 2 of eqn. 4.7 in x-axis) and due to the subgrain size changes (term 3 of eqn. 4.7 in y-axis) are shown in Fig. 4.16 and Fig. 4.17. These two figures are based on strengthening contribution estimated from changes in precipitate fraction obtained from lattice changes and hardness respectively. The planar fit obtained is also shown along with the projection of the hardness values on x-y plane as square filled dots. The correlation coefficient  $\bar{R}^2$  is 0.75 and 0.93 for the case of fractional estimates based on changes in lattice parameter and hardness respectively. The correlations are better than that obtained in the 2-d plots shown in Fig. 4.14 and Fig. 4.15. The deviation of the plane shown in Fig. 4.16 from the measured hardness is within 30 VHN. In Fig. 4.17, the deviation of the plane at each of the locations in the 3-dimensional space is within 10 VHN at all the points except 16 VHN at

one of the locations. The intercepts are 280 and 250 VHN and the coefficient  $k_l$  has values of  $1.42\text{e-}6$  and  $1.51\text{e-}6$  for each of the above approaches with an error one order less.

When the planar fit is obtained by considering only the strengthening contributions due to coherency, the  $\bar{R}^2$  values were low and the  $H_0$  values were substantially higher than the hardness obtained in solutionized condition. It was also reflected with a negative  $k_H$  coefficient. This clearly showed that all the strengthening contributions were not included. The maximum strengthening observed due to coherency strengthening is  $\sim 70$  MPa, which is consistent with the observations of 75 MPa reported by Holzer et al. [104].

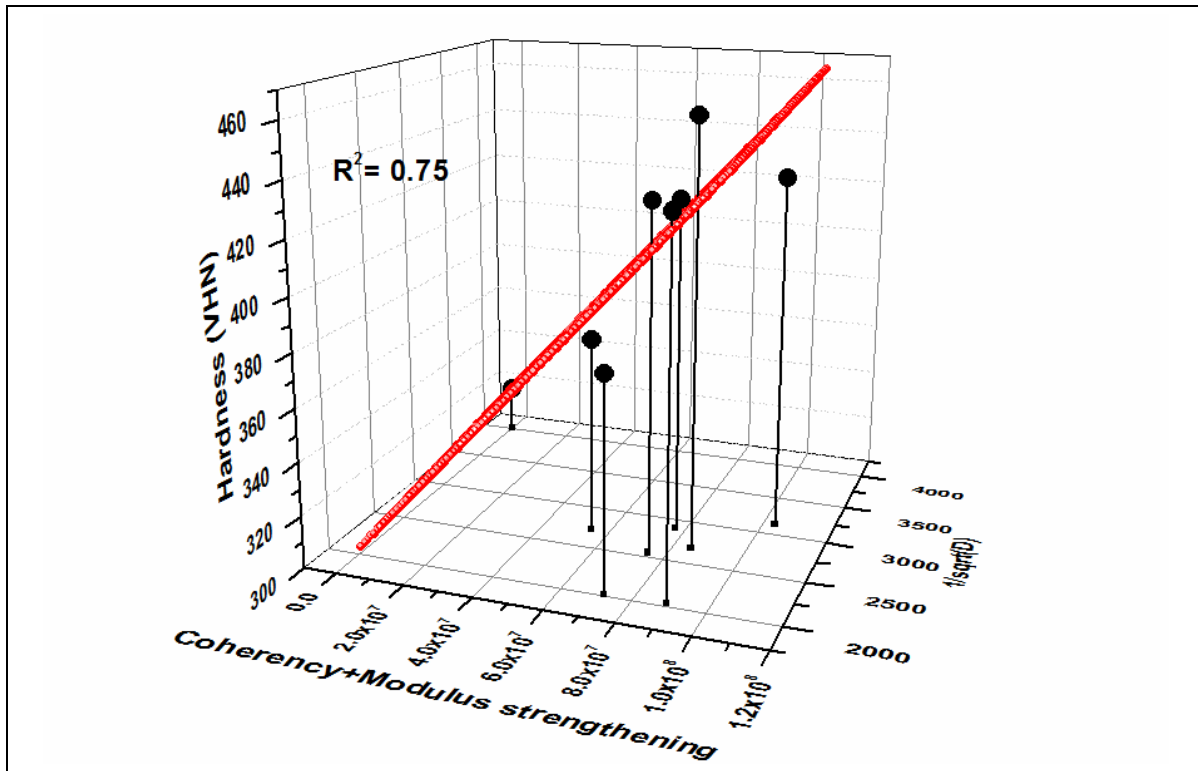


Fig. 4.16. Linking hardness with the strengthening mechanisms based on eqn. 4.7, x axis in (Pa) and y axis in ( $\text{m}^{-1/2}$ ) (precipitate fraction estimated from changes in lattice)

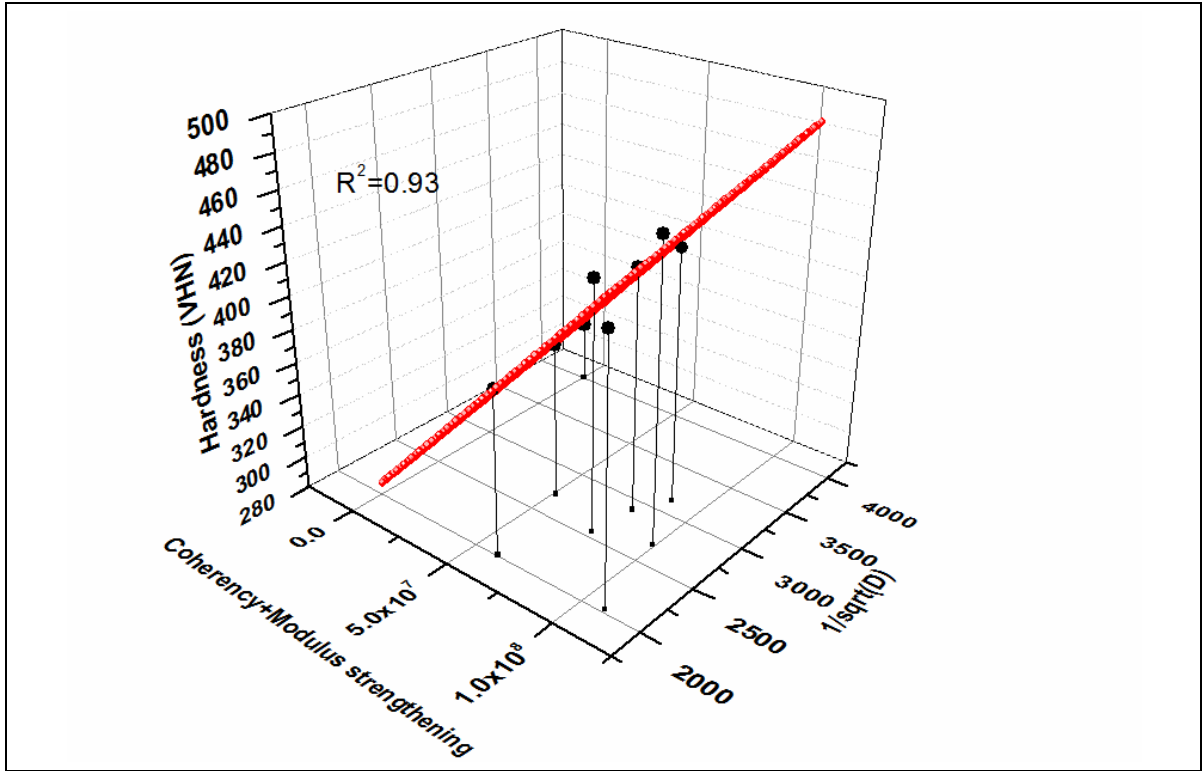


Fig. 4.17. Linking hardness with the strengthening mechanisms based on eqn. 4.7,  $x$  axis in (Pa) and  $y$  axis in ( $m^{-1/2}$ ) (precipitate fraction estimated from changes in hardness)

#### 4.6.1 Discussions on the estimated constants

The Hall-Petch constant  $k_H$  is determined by linking with the hardness scale. To compare the value of  $k_H$  determined by this approach with existing literature, a conversion of scales is required. By studying many materials, it has been shown that the hardness ( $H$ ) in Vickers hardness number scale and flow stress are related by  $H = 3\sigma_f$  [124]. Converting the hardness in VHN scale to flow stress in MPa scale is done by multiplying the hardness with 3.2. Converting the hardness to yield strength, the plots shown in Fig. 4.17 were redrawn but are not shown here. From the planar fit of the converted plot, the constants  $k_l$  and  $k$  (the Hall-Petch constant) are estimated. The value of Hall-Petch constant thus obtained is  $57 \text{ MPa}\cdot\mu\text{m}^{1/2}$ . A value of  $k$  in the range of  $0.04$  to  $0.16 \text{ MPa}\cdot\text{m}^{1/2}$  has been reported for various materials with fcc structure [128]. In low carbon steel, a Hall-Petch coefficient of around  $600 \text{ MPa}\cdot\mu\text{m}^{1/2}$  is reported, whereas it is between  $130$ - $180 \text{ MPa}\cdot\mu\text{m}^{1/2}$  in interstitial free steel [129]. While considering the average spacing between the low and

high angle boundaries as  $D_{av}$ , a Hall-Petch coefficient of  $310 \text{ MPa}\cdot\mu\text{m}^{1/2}$  has been estimated for shot-peened low carbon steel specimens deformed to different strains [130]. The lower value of  $k$  obtained in the present study is attributed to the use of subgrain size estimated from XRD/LPA measurements [131]. Similarly, the intercept of the plane to the z-axis occurs at a value of  $0.7967 \pm 0.11 \text{ GPa}$ . This value is close to the 0.2% proof stress of 670 MPa reported for 3.95% Cu added Fe-Cu alloy [51]. Similarly, yield strength of tempered 17-4 PH steel has been reported as 0.895 GPa [39].

Iso-hardness contours are derived from the projection of the plane shown in Fig. 4.17 which is depicted in Fig. 4.18. From these contours, it is possible to estimate the combination of crystallite size and strengthening contribution required to achieve a given strength in the material. This would be beneficial to improve the strength, under a given ageing condition (precipitation strengthening is known) by modifying the grain structure by cold working or by any other process.

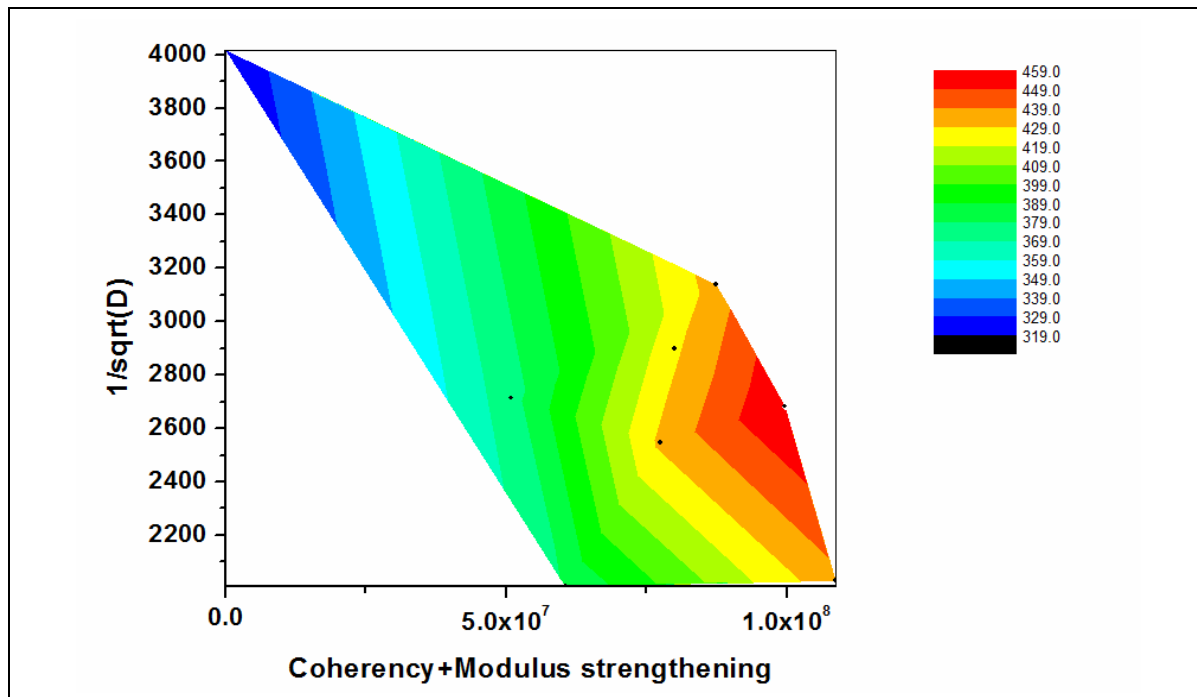


Fig. 4.18. The plan view of the iso-hardness contours corresponding to the strengthening from the precipitates and grain boundaries

In this study, the influence of depletion of the matrix due to Cu precipitation would reduce the solid solution strengthening contribution, and was not considered. However, while addressing the solid solution strengthening of  $\alpha$ -iron, Schmauder et al. [132] found that the strengthening increases drastically to 60 MPa when the Cu concentration increases to 1% and later slowly increases from 80 to 140 MPa when the Cu concentration increases from 2 to 5%. Holzer et al. [104] had reported a solid solution strengthening contribution of Cu in Fe as  $k_{Cu} \cdot x_{Cu}^{0.5}$  with  $k_{Cu}$  as 40 MPa/(wt% Cu) and  $x_{Cu}$  as the Cu content of the matrix in wt%. A reduction in Cu content in the matrix from 4 to 2.5 % (due to 1.5% Cu precipitate formation as estimated earlier) would reduce the solid solution strengthening contribution by 17 MPa. Hence, ignoring the effect of depletion of the precipitating element from the solid solution strengthening is marginal. However, the results would improve if this effect is also considered.

#### 4.7 Summary

- ✓ The Avrami exponent determined is 0.52 which is marginally higher than the published literature value of 0.45 for this class of steel.
- ✓ In the overaged regime, the kinetics follows the Wilson model showing that the Orowan mechanism is predominant.
- ✓ The activation energy of the precipitation process is estimated as  $143 \pm 20$  kJ/mol which also matches with published literature.
- ✓ The observed anisotropic broadening in WH plot has been addressed using the modified WH approach which takes into account the contrast caused by dislocations to address the anisotropic broadening. The application of the modified WH approach to study ageing behaviour is able to identify early precipitation and addresses the anisotropic broadening.

- ✓ The normalized mean square strain estimated shows good correlation with changes in hardness indicating the contribution of coherency strain to hardening.
- ✓ The crystallite size changes are consistent with microstructural observations.
- ✓ The hardness and normalized mean square strain have been correlated linearly to the tempering parameter in the over aged and incoherent regime.
- ✓ A simple approach is presented for theoretically determining the lattice parameter and is used to estimate precipitate fractions below 2%.
- ✓ The parameters derived from XRD profile analysis, namely lattice parameter, microstrain and crystallite size in 17-4 PH steel have been uniquely used to understand the age hardening behaviour of 17-4 PH steel.
- ✓ Studies using this unique approach clearly show that coherency strengthening, modulus strengthening and grain boundary strengthening act in tandem and result in improved strength of this steel. This approach would be used to evaluate the strengthening mechanisms active in maraging steel in the following chapter.
- ✓ The values of constants namely  $H_o$  and  $k$  determined in this study matches well with the published literature [51,129,130,39].
- ✓ Iso-hardness curves have been generated and they can be used for determining the appropriate contributions to strengthening from grain boundaries and precipitates.

## Chapter - 5

### 5 Ageing behaviour of M250 grade maraging steel

In this chapter, the studies carried out on isothermally aged (at 482 °C, 755 K) M250 grade maraging steel are to be presented. First, the changes in hardness on ageing and the kinetic parameters derived from the change in hardness would be presented. The results of the XRD analysis carried out using modified WH approach and modified WA analysis would be explained. A comparison of the results obtained by the two approaches would be made. The approach adapted for using the observed changes in lattice parameter for estimating precipitate fraction would be presented. Finally, the parameters estimated from XRD/LPA are used to explain the observed increase in strength of maraging steel using a unique approach.

#### 5.1 Precipitation kinetics from hardness

The variation of hardness with ageing time of M250 grade maraging steel samples aged at 482 °C (755 K) is shown in Fig. 5.1a. The hardness variation shows typical age hardening features, i.e. the hardness in solutionized condition (329 VHN) increases to a peak value of 600 VHN on ageing for 40 h. On further increasing the ageing time to 70 and 100 h, hardness decreases, which implies over ageing. As explained in §4.1.1, the kinetics during the ageing regime is studied using the Avrami equation (eqn. 4.1). The hardness is normalized with the peak hardness using the approach of Robino et al. [90] as detailed in §4.1.1. The variation of normalized hardness which is equivalent to precipitate fraction with ageing duration is shown in Fig. 5.1b. The fit of the Avrami equation obtained from the normalized hardness is also shown in Fig. 5.1b. The Avrami exponent ( $n$  in eqn. 4.1, p. 47) estimated from this fit is  $0.34 \pm 0.04$  which matches well with the published data of 0.35 [29] and 0.39 [43] arrived at from resistivity measurements at this temperature. An

exponent value in this range has been attributed to initial precipitation on dislocations, followed by growth on these dislocations [29]. A value of 0.34 is determined from microstrain based on the assumption that the increase in coherency strain is due to growth of precipitates [32]. This result would be presented in the following section (§5.2.1.2, p. 90).

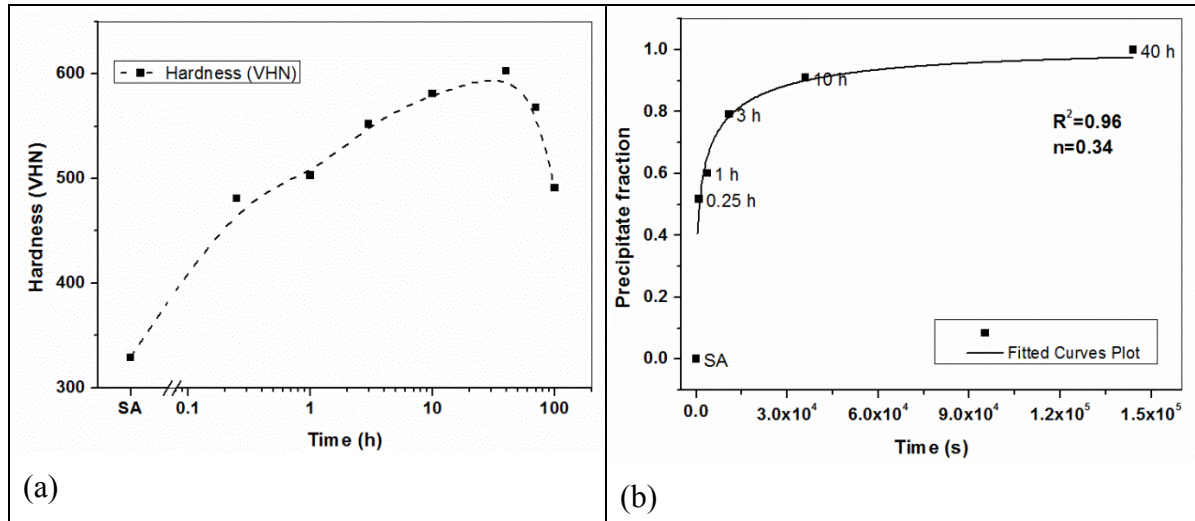


Fig. 5.1 (a) Variation of hardness with ageing time (h) and b) Fraction of precipitates transformed with ageing time (s) (legends indicate the ageing time in h)

## 5.2 XRD studies in maraging steel

The XRD spectra of samples aged at 482 °C (755 K) for 0.25, 70 and 100 h along with the solution annealed specimen is shown in Fig. 5.2. The peaks in the spectrum of the solution annealed sample have been marked and indexed, which correspond to body centred cubic (bcc) matrix. All the peaks show similar features except for changes in full width at half maximum (FWHM). In addition to the matrix peaks from bcc structure, the peaks due to austenite are indexed in the XRD profile of 100 hour aged sample. Evolution of reverted austenite is clearly seen in samples aged at 70 and 100 h. The volume percent of austenite ( $\gamma$ ) formed by reversion of martensite during ageing, was determined by direct comparison of the integrated intensities of the (111) and (200) planes of the  $\gamma$  phase with the intensities of the (110) and (200) planes of the bcc phase [55]. The percentage of austenite has been



estimated as 5 and 30% in 70 and 100 h samples respectively. The reduction in hardness observed on ageing for 70 and 100 h (Fig. 5.1a) is consistent with the austenite formed.

Features of an additional peak seen at an angle of  $\sim 42^\circ$  (as identified in 100 h aged sample) is found to match with the PDF (Powder diffraction files from ICDD) cards of  $\text{Ni}_3\text{Ti}$  (05-0723) and  $\text{Fe}_2\text{Mo}$  (06-0622). Clearly distinguishable peaks corresponding to intermetallic phases are observed in the samples aged for 70 h and more. However all the peaks corresponding to these intermetallic phases could not be identified as some of the intense peaks coincide with the peaks of the matrix that has both martensite and austenite. The full width at half maximum (FWHM -  $\beta$ ) corresponding to all the phases and peak locations were determined for all the specimens using the procedures mentioned in §3.3.3. These values are used in further analysis of XRD data.

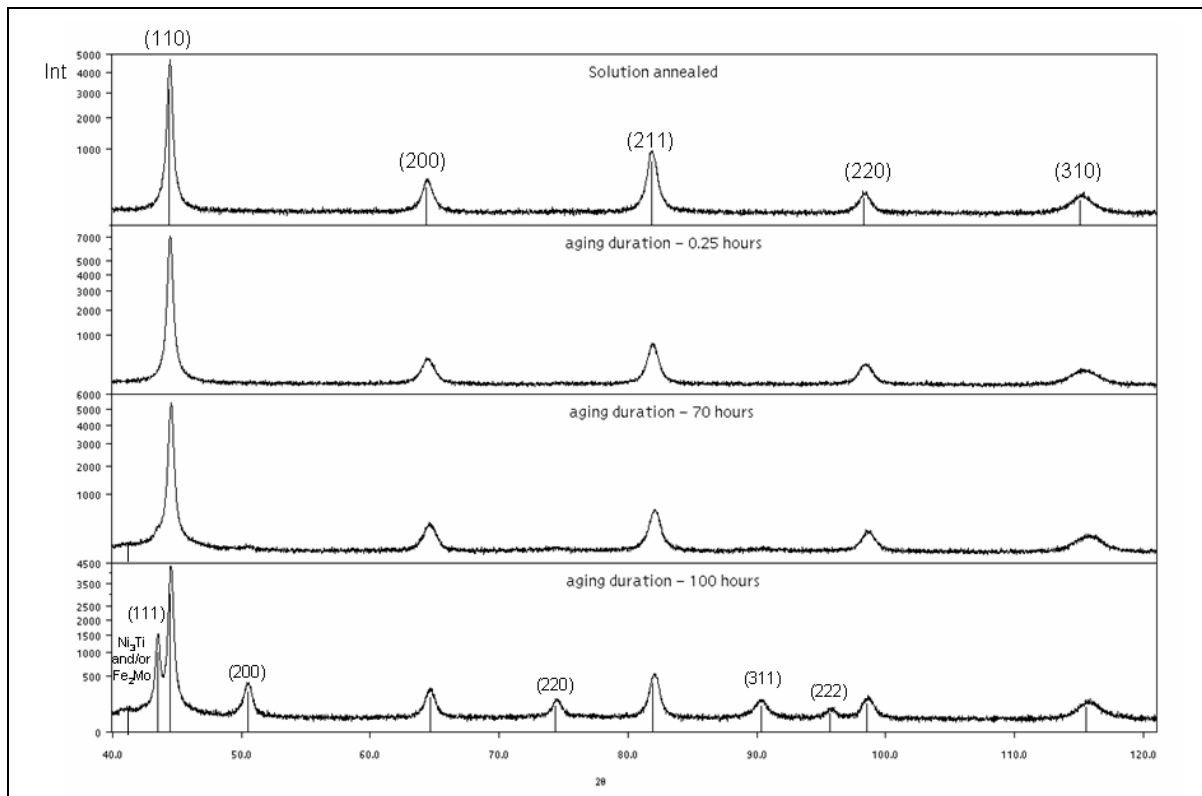


Fig. 5.2 XRD spectra of solution annealed M250 samples along with 0.25, 70 and 100 h aged samples

### 5.2.1 Modified WH approach

The WH plots (as per eqn. 2.11, p.30) and modified WH plots (as per eqn. 2.23, p.36) of samples aged for 0.25, 10 and 100 hours at 482 °C (753 K) are shown in Fig. 5.3a and b respectively. Similar feature of anisotropic broadening with diffraction angle is observed for all the samples. The typical features of all the plots were that reflections corresponding to (200) and (310) had higher values of  $\beta\cos\theta$  as compared to (110), (211) and (220) which almost followed a linear increase with diffraction angle owing to the uniform contrast factor ( $\overline{C}$ ) (eqn. 2.24, p.36) arising from the same  $H^2$  value.

The observed anisotropic broadening is treated using the modified Williamson-Hall (mWH) approach which takes into account the strain anisotropy caused by dislocations. All the samples showed similar linear fit with a correlation coefficient better than 0.99. The observed linear fit also validates the assumption that there is no local variation of dislocation density and hence makes the variable  $O$  of eqn. 2.23 small. Such linear behaviour has been observed in ball milled iron powder (Fig. 8 of Ref. [80]) and Rb-doped  $\text{Rb}_3\text{C}_{60}$  fullerite powder specimens (Fig. 5(b) of Ref. [81]). Similar linear fits were obtained in 17-4 PH steel samples reported in the earlier chapter.

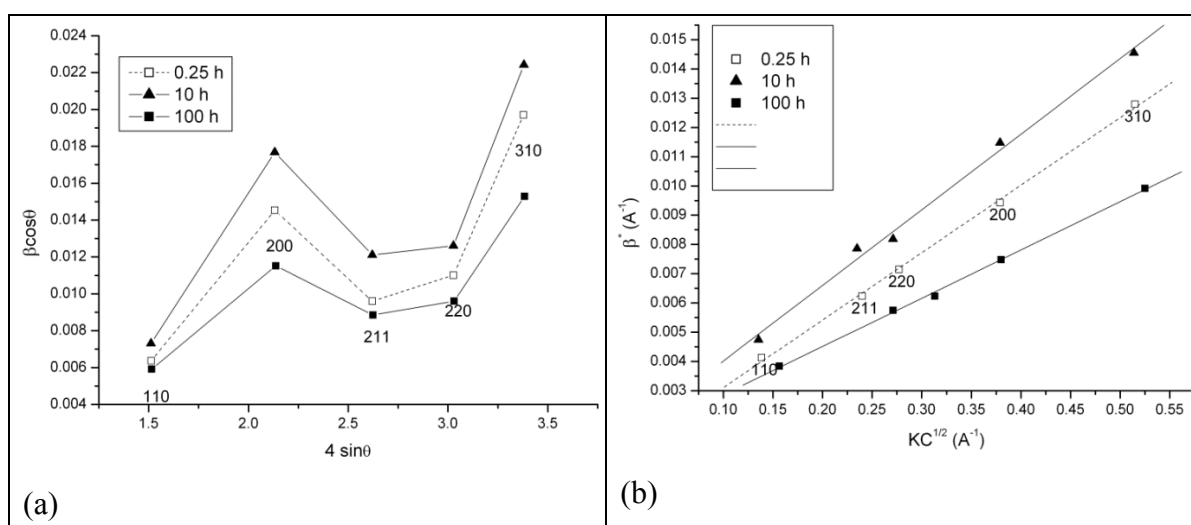


Fig. 5.3 (a) WH plot (b) modified WH plot for samples heat treated at 482 °C for 0.25, 10 and 100 h

#### 5.2.1.1 *Changes in microstrain on ageing*

The normalized mean square strain ( $\alpha$ ) is estimated from the slope of the mWH plots shown in Fig. 5.3b. The variation of normalized mean square strain (microstrain) with ageing duration is shown in Fig. 5.4. Among all the samples,  $\alpha$  is the lowest for the solution annealed sample. On initial ageing, recovery of martensite [26,133] takes place in this steel which should ideally reduce the strain in the matrix. However, the rapid increase in the strain by  $\sim 100\%$  after 0.25 hours of ageing is attributed to the formation of fine intermetallic precipitates causing coherency strains. The TEM studies carried out by Vasudevan et al. [29] on 1 h aged C250 samples showed pronounced streaking indicative of precipitation. The elemental composition of commercial C250 grade steel and M250 grade steel used in this study are almost similar. Rajkumar et al. [133] reported precipitate reflections from selected area diffraction (SAD) patterns of 3 h aged M250 steel samples, similar to the observations of Vasudevan et al. [29]. Peters and Cupp [43], from their resistivity measurements have found that no incubation period is required for precipitation in maraging steels. Hence, the increase in the microstrain after 0.25 h of ageing can be used to detect early precipitation. Novelo-Peralta et al. [134] carried out characterization of Al-Mg-Cu alloys using WH method and by estimating the attenuation factor. The authors found negligible change in microstrain during early ageing (up to 0.5 h) but found significant changes after 6 h of ageing. However, change in attenuation factor during early ageing was reported by these authors [134]. In this study, early precipitation induced microstrain has been detected using mWH approach in both 17-4 PH steel and maraging steel.

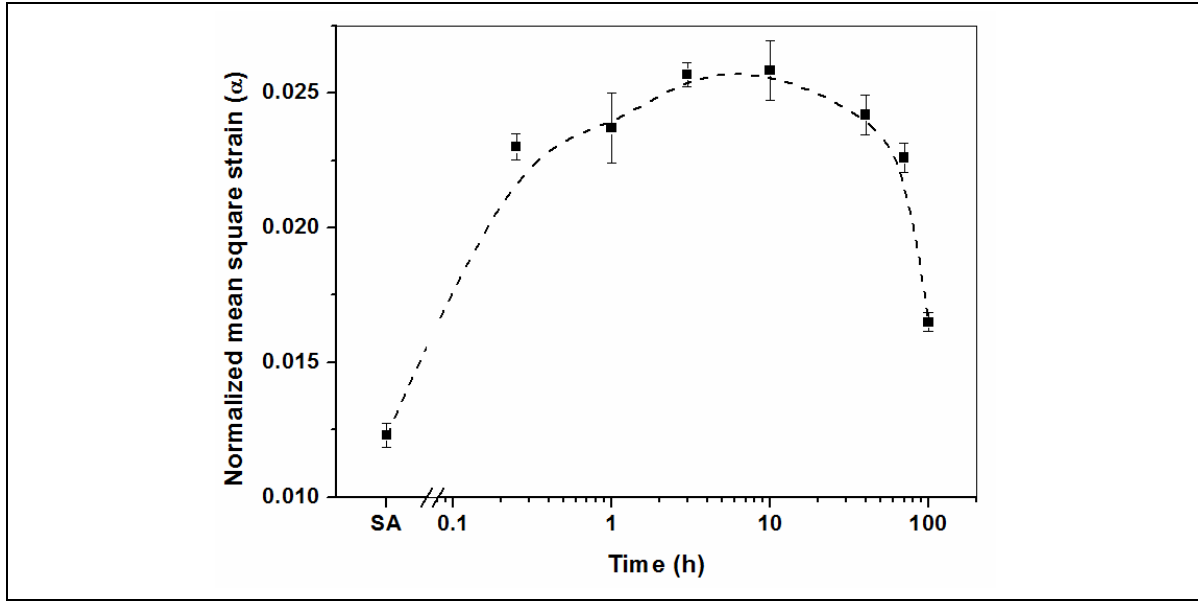


Fig. 5.4 Variation of normalized mean square strain with ageing time

The peak microstrain is observed in samples aged for 10 h at 482 °C as shown in Fig. 5.4. This indicates that the precipitates are still coherent with the matrix. The decrease in the microstrain on ageing above 10 h is attributed to the coarsening of precipitates which causes reduction in coherency strains. Optimum size and distribution of the precipitates is essential to achieve optimum hardness. It is clear from Fig. 5.1 and Fig. 5.4. that the increase in the hardness of this material on ageing is related to the increased microstrain ( $\alpha$ ) in the matrix which increases due to the formation of fine intermetallic precipitates.

#### 5.2.1.2 Microstrain for precipitation kinetics

The shape of the normalized mean square strain ( $\alpha$ ) curve with ageing (Fig. 5.4) suggests that the kinetics of precipitation can be represented by the Avrami equation. The fraction of precipitates transformed can be obtained by normalizing  $\alpha$  and is given by  $(\alpha_t - \alpha_{SA}) / (\alpha_{\max} - \alpha_{SA})$ , where  $\alpha_t$ ,  $\alpha_{SA}$ , and  $\alpha_{\max}$  indicate the  $\alpha$  values at ageing time  $t$ , solution annealed condition and the maximum value of  $\alpha$  achieved here at 10 h of ageing respectively. The use of  $\alpha$  value of sample aged for 10 h duration as  $\alpha_{\max}$  is also based on the fact that size increment of precipitates during ageing occurs due to coarsening rather

than growth kinetics, once precipitation growth completes [31]. The reduction in microstrain on further ageing is attributed to the coarsening of precipitates causing the coherency strains to reduce. This normalization procedure is valid provided the increase in  $\alpha$  is due to the formation of precipitates. The value of Avrami exponent thus determined using the above normalization procedure is  $0.34 \pm 0.08$  which matches with the value determined using hardness measurements as detailed in §5.1. The fit of the above equation clearly showed that the changes in microstrain on ageing can be used as the basis to model the kinetics of precipitation. For this approach to be valid, the increase in the microstrain due to precipitation should clearly dominate the reduction in microstrain expected due to annihilation of dislocations. This approach of using microstrain to study precipitation kinetics could not be validated in 17-4 PH steel as peak microstrain was achieved as early as 1 h at the temperature and time ranges considered in this study.

While peak hardness in maraging steel is observed at 40 hours (Fig. 5.1a), normalized mean square strain peaks at 10 hours. These results are consistent with the findings of Guo et al. [31] that, growth of precipitates completes ahead of peak hardness at various temperatures in C250 steel. Similar observations were made while studying ageing behaviour of 17-4 PH steel as reported in §4.2.2.

#### *5.2.1.3 Crystallite size changes on ageing*

Table 5.1 gives the variation of crystallite size with ageing duration. A lower value of crystallite size (38 nm) observed in the solution annealed specimen is consistent with the high density of dislocations observed in this condition in various studies [29,133]. It is well known that dislocation substructure fragments the grains of polycrystalline materials into small domains. Also, the drastic increase in crystallite size to (125 nm) observed after 0.25 hours of ageing at 482 °C stems from the annihilation of dislocation substructures,

notwithstanding the initiation of precipitation of intermetallics. Annihilation of dislocations has been inferred by Rajkumar et al. [111] from positron annihilation studies under these conditions. The crystallite size estimates of the samples aged for 10, 40, 70 and 100 hours are almost same, which shows that the internal substructure of the martensite matrix remains unchanged.

Table 5.1 Changes in crystallite size estimated from the intercept of mWH plot shown in Fig. 5.3 along with the correlation coefficient

Ageing duration	Crystallite size estimated from modified WH plot (nm) [32]	Correlation coefficient of modified WH plot
Solution annealed	38±2	0.998
0.25 h	125±25	0.999
1 h	71±22	0.995
3 h	153±35	0.999
10 h	70±18	0.997
40 h	76±14	0.998
70 h	90±15	0.999
100 h	83±9	0.993

### 5.2.2 Modified WA analysis

The Fourier transformation of each of the 5 peaks was carried out to estimate the Fourier coefficients ( $A(L)$ ) based on the procedures mentioned in §2.7.2 (p. 31). A typical plot of  $\ln A(L)$  vs.  $K^2 \bar{C}$  of 1 h aged sample is shown in Fig. 5.5 along with the fits obtained based on eqn. 2.28 (p. 38). The size coefficient  $A^S(L)$  is estimated from the intercept of the fit. The coefficient of the first order term gives the estimate of  $\rho BL^2 \ln(R_0/L)$  for each value of  $L$  and is denoted as  $X(L)$ .

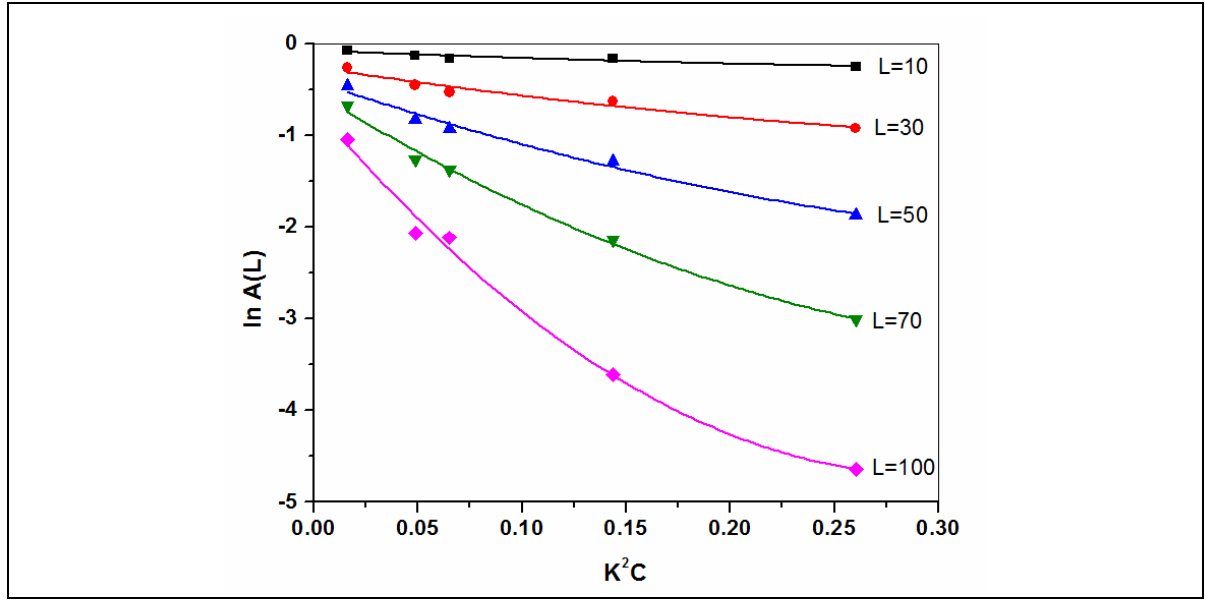


Fig. 5.5 Plot of  $\ln A(L)$  vs.  $K^2 \bar{C}$  of 1 h sample at  $L$  values of 10, 30, 50, 70 and 100 Å

#### 5.2.2.1 Dislocation parameters derived from mWA analysis

The dislocation density  $\rho_S$ , and outer cutoff radius of the dislocations  $R_e$  are estimated based on procedures mentioned in §2.8.2 by plotting  $X(L)/L^2$  vs.  $\ln L$  as per eqn. 2.29 in p.38. The values obtained under different ageing conditions are listed in Table 5.2. The slope of the  $A^S(L)$  vs.  $L$  plot has been used to determine the area weighted size  $L_S$ , as per eqn. 2.19. The dislocation density,  $\rho_S$  determined by this approach shows continuous increase and peaks at 10 h. However, Williamson and Smallman [135] had shown that the average dislocation density,  $\rho = (\rho_S * \rho_D)^{0.5}$  where the subscripts S and D denote the contributions from strain and domain size respectively. The contribution to dislocation density from domain size can be estimated from  $3/D^2$  where  $D$  is the domain size [135]. In studies based on WA approach, the area weighted size  $L_S$  has been used as the value of  $D$  [85,136]. Based on this approach, the average dislocation density is determined and the values are listed in the fifth column of Table 5.2. The dislocation arrangement parameter or the Wilkens arrangement parameter is defined as  $M = R_e \sqrt{\rho}$  [137]. The Wilkens parameter  $M$  is listed in the last column of Table 5.2.

Table 5.2 Variation of the various parameters determined from modified WA approach with ageing duration is shown below

Ageing duration	Dislocation density ( $\rho_s$ ) from mWA ( $\text{m}^{-2}$ )	$L_s$ ( $\text{\AA}$ )	$R_e$ ( $\text{\AA}$ )	Average dislocation density $\rho=(\rho_D * \rho_s)^{0.5}$ ( $\text{m}^{-2}$ )	Wilkens Parameter M
Solution annealed	8.38E15	118	250	1.34E16	2.29
0.25 h	1.08E16	140	361	1.28E16	3.76
1 h	1.06E16	120	388	1.48E16	4.01
3 h	1.08E16	118	395	1.52E16	4.11
10 h	1.55E16	112	280	1.92E16	3.5
40 h	1.12E16	106	344	1.73E16	3.65

The value of dislocation density determined in solution annealed condition is close to the value of  $1 \times 10^{16} \text{ m}^{-2}$  reported for 18Ni maraging steel [88] from XRD studies. A dislocation density of  $6 \times 10^{14} \text{ m}^{-2}$  has been determined for 6Cr-3Ni low carbon steel under solutionized condition [138]. The  $\rho$  value decreases marginally on ageing for 0.25 h and increases to a peak value on ageing for 10 h. It is well known that, on ageing, annihilation of dislocations takes place and dislocation density would reduce. TEM studies on the steel used in this study had revealed reduction in dislocation density in 3 h aged specimens [111]. The variation of the average dislocation density with ageing duration is shown in Fig. 5.6. However, the observed changes in average dislocation density (on ageing) determined based on the XRD analysis needs to be understood and validated. It is to be noted that the WA analysis carried out is also sensitive to the effect of coherency strain due to precipitates.

Hence, a survey of literature clearly shows that magnetic Barkhausen emission based studies [36,133] and nonlinear ultrasonic techniques [139] are sensitive to both precipitation and dislocation induced effects. The nonlinear ultrasonic (NLU) parameter



( $\beta$ ), which is the ratio of the amplitudes of the second and first harmonics of the ultrasonic wave is a strong function of dislocation density and coherency strains due to precipitates [140,141,142]. The variation of relative  $\beta$  parameter ( $\beta$  of each sample normalized with the  $\beta$  measured in solutionized condition) with ageing is also shown in Fig. 5.6. Viswanath et al. [139] had separated the observed variation of the relative  $\beta$  parameter with ageing in to 3 regimes [32]. The authors explained the initial decrease to annihilation of dislocations. In the regime above 0.25 h, up to 10 h, a linear increase was explained based on the increase in microstrain estimated from the mWH approach presented in this thesis [32]. Above 10 h of ageing, the observed decrease in relative  $\beta$  parameter was attributed to the coarsening of precipitates and formation of austenite. The average dislocation density determined based on mWA analysis is in agreement with the changes in  $\beta$  parameter. In the following section, an attempt would be made to separate the contributions of precipitates and dislocations to XRD profile broadening.

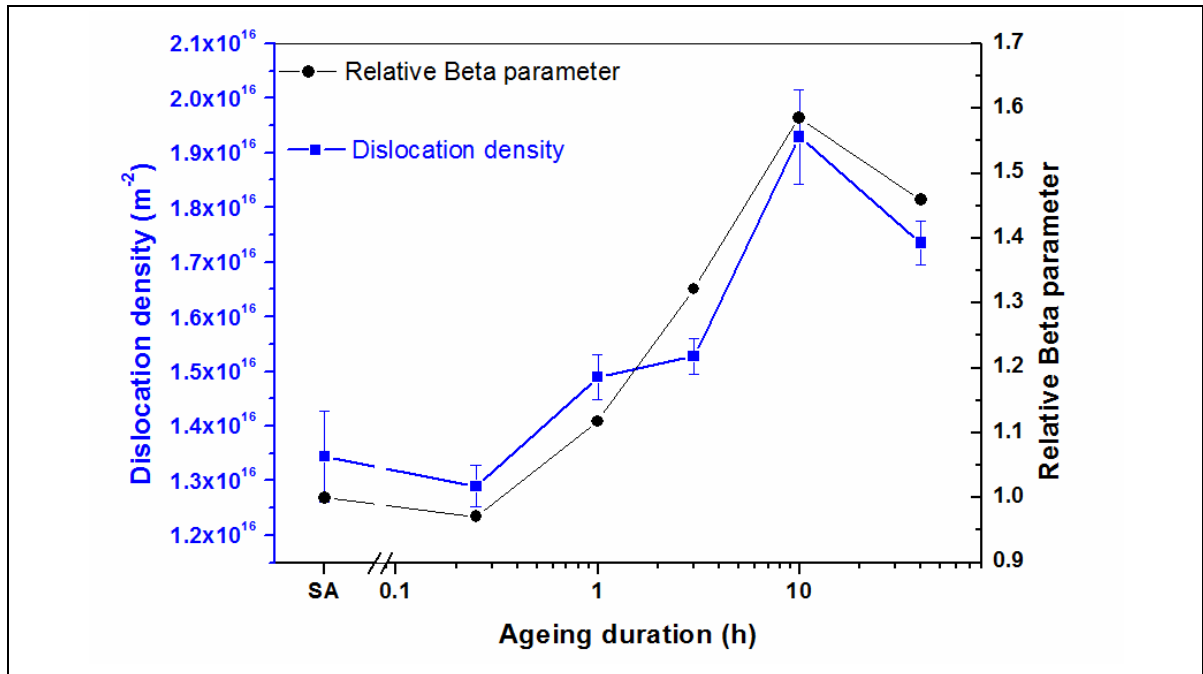


Fig. 5.6 Variation of dislocation density and relative beta parameter [139] with ageing duration (SA indicates solution annealed condition)

The outer cut-off radius of dislocations ( $R_e$ ) drastically increases on ageing for 0.25 h and on further increase in duration up to 3 h, increases marginally. The domain size increased considerably as reported in Table 5.1. The variation of Wilkens parameter  $M$  with ageing follows the trend of  $R_e$ . Shin et al. [138] observed an increase in Wilkens parameter accompanied by increase in domain size while studying the annealing behaviour of precipitation hardenable 6Cr-3Ni martensitic steel. Similar observations were made by Dey et al. [20] in cold-worked Pb-Bi alloys. The results observed here are consistent with these observations. It is to be noted that  $R_e$  is a parameter, having statistical–physical meaning which characterizes the interaction of dislocations and its distribution in an ensemble [86,137]. The Wilkens parameter, signifies the effectiveness of the screening of the strain fields of the neighbouring dislocations. If the value of  $M$  is smaller or greater than unity, the screening effect is strong or weak. Alternately, if the  $M$  parameter is large, the dislocations are randomly located and the tails of the XRD profile converge to a Gaussian function [137].

On increasing the ageing duration to 10 h, a reduction in  $M$  and  $R_e$  is accompanied by an increase in dislocation density. This indicates that the screening effect of dislocations increases. Similar reduction in Wilkens parameter, accompanied by increase in dislocation density has been observed by Garabagh et al. [143] during deformation of 18 Ni maraging steel. On ageing for 10 h, a reduction in volume weighted crystallite size determined from mWH analysis (Refer Table 5.1) with an increase in dislocation density (Refer Table 5.2) is observed. During deformation of maraging steel, Garabagh et al. [143] estimated a decrease in  $M$  value, and inferred that the dislocation arrangement goes towards the formation of low-energy dislocation structures, acting as an initial step in the formation of dislocation cells and ultra-fine grains. Dey et al. [20] observed a decrease in Wilkens

parameter accompanied by a decrease in domain size. The reduction in crystallite size observed in this study is consistent with the reported observations.

#### 5.2.2.2 Mean square strain as a function of column length

The value of  $\langle \varepsilon^2(L, g) \rangle$  can be determined from  $X(L)$  as per eqn. 2.27. Due to the reciprocity of column length  $L$  (Refer Fig. 2.1 in p. 33) with  $d$  space, the tail regions correspond to effects at shorter column lengths, and the regions near the peak correspond to longer column lengths. The inferences that are drawn from the variation of  $\langle \varepsilon^2(L) \rangle$  as a function of column length  $L$  are discussed further. The variation of  $\langle \varepsilon^2(L) \rangle$  vs  $L$  for the (200) plane is shown in Fig. 5.7a and b as filled square and circle. Fig. 5.7a shows the variation of  $\langle \varepsilon^2(L) \rangle$  of solution annealed sample along with that of 3 h aged sample. It is clear from Fig. 5.7a that the strain  $\langle \varepsilon^2(L) \rangle$ , at shorter column lengths is more for the solution annealed sample. While the strain is lower at shorter column lengths, it is more at longer column lengths in the 3 h aged sample. This is indicative of annihilation of dislocations affecting strains at shorter column lengths and precipitate induced effects having long range effects.

Similarly, Fig. 5.7b depicts the variation of  $\langle \varepsilon^2(L) \rangle$  of 10 and 40 h aged samples. From Fig. 5.7b it is seen that the strain is lower at shorter and longer column lengths in 40 h aged sample as compared to the 10 h aged sample. The normalized mean square strain ( $\alpha$ ) (estimated using mWH analysis by using the FWHM as the breadth  $\beta$ ) of the 40 h sample showed a reduction in microstrain ( $\alpha$ ) as compared to the 10 h sample. A marginal increase in strain (of 10 h aged sample) at shorter column lengths is observed as compared to that of the solution annealed sample. This is indicative of formation of fresh dislocations, as some of the precipitate particles reach their critical size to form interface

dislocations which is also reflected in the apparent reduction in crystallite size [50] of 10 h aged sample, as shown in Table 5.1 p. 92. The changes in  $\rho$  and  $M$  parameter are also consistent with these observations.

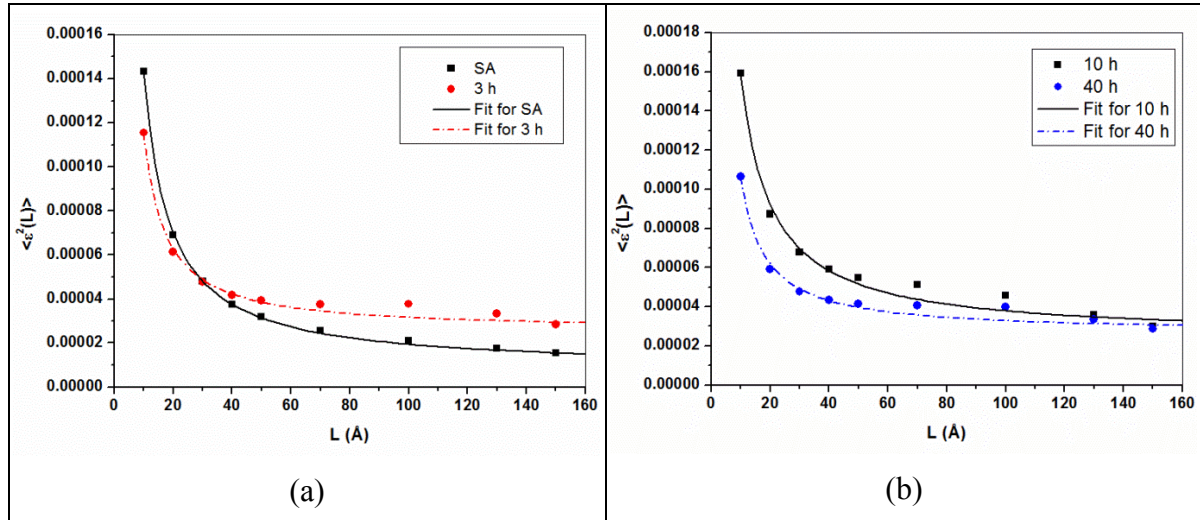


Fig. 5.7 Variation of  $\langle \epsilon^2(L) \rangle$  as a function of column length  $L$  a) for solutionized and 3 h aged sample b) 10 and 40 h aged sample

### 5.2.3 Comparison of the strain estimated by mWH and mWA methods

The observed variation of  $\langle \epsilon^2(L) \rangle$  as a function of column length  $L$  has been analyzed by various authors. According to Rothman and Cohen [144], the mean square strain due to dislocations follows an inverse relation with column length and is given as

$$\langle \epsilon^2(L) \rangle \propto \frac{1}{L} \quad - - (5.1).$$

A detailed derivation of the variation of mean square strain has been carried out by Krivoglaz [79] and Wilkens [137] and had been shown to be proportional to  $\ln(R_e/L)$  and the detailed expression is given in eqn. 2.27 (p.37). Balzar and Ledbetter [16] formulated an empirical relation for strain  $\langle \epsilon^2(L) \rangle$  from the Cauchy and Gaussian components of broadening due to distortion and their relationship (eqn. 19 of [16]) can be written of the form

$$\langle \varepsilon^2(L) \rangle = P_0 + \frac{P_1}{L} \quad - - (5.2).$$

The parameters  $P_0$  and  $P_1$  represent broadening due to Gaussian and Cauchy components respectively.

Expanding the logarithmic expression (eqn. 2.27, p.37) into Taylor series and limiting the same to second order term, the mean square strain is given as

$$\langle \varepsilon^2(L) \rangle = P_0 + \frac{P_1}{L} + \frac{P_2}{L^2} \quad - - (5.3).$$

The fit of the above equation to the data obtained at various  $L$  values for different samples is shown in Fig. 5.7. The adjusted  $R^2$  is better than 0.97 in all the samples. However, the solution annealed sample which is known to have high density of dislocations shows the best fit in the entire  $L$  range which is consistent with the fact that the equations have been derived for dislocated crystals. In other samples, the fit of the data to the eqn. 5.3 is closer at column lengths up to 100 Å. Berkum et al. [145] analyzed the validity of WA analysis and other approaches and found that if the strain distributions deviate more from the Gaussian, the smaller the  $L$  range for which the WA analysis is valid. These authors also showed the applicability of WA analysis in the  $L$  range up to 100 Å.

From the fit, the values of  $P_0$ ,  $P_1$  and  $P_2$  are determined. The parameter  $P_0$  corresponds to the strain observed at larger column lengths. The strain is estimated as  $P_0^{0.5}$ . The strain thus estimated from  $P_0$  as a function of ageing duration is shown in Fig. 5.8 as filled squares. In the same figure, the normalized mean square strain ( $\alpha$ ), estimated from modified WH analysis and presented in §5.2.1, is redrawn. Though there are minor variations, the trend of the variation of strain estimated from both the approaches remains similar. It is clear from this comparison that the long range strain estimated from the mWA analysis matches well with the normalized mean square strain ( $\alpha$ ) estimated from mWH analysis. The variation of  $P_1$  is indicative of dislocation annihilation effects.

However, the physical interpretation of the parameters,  $P_1$  and  $P_2$  determined from the fitting requires further analysis and validation.

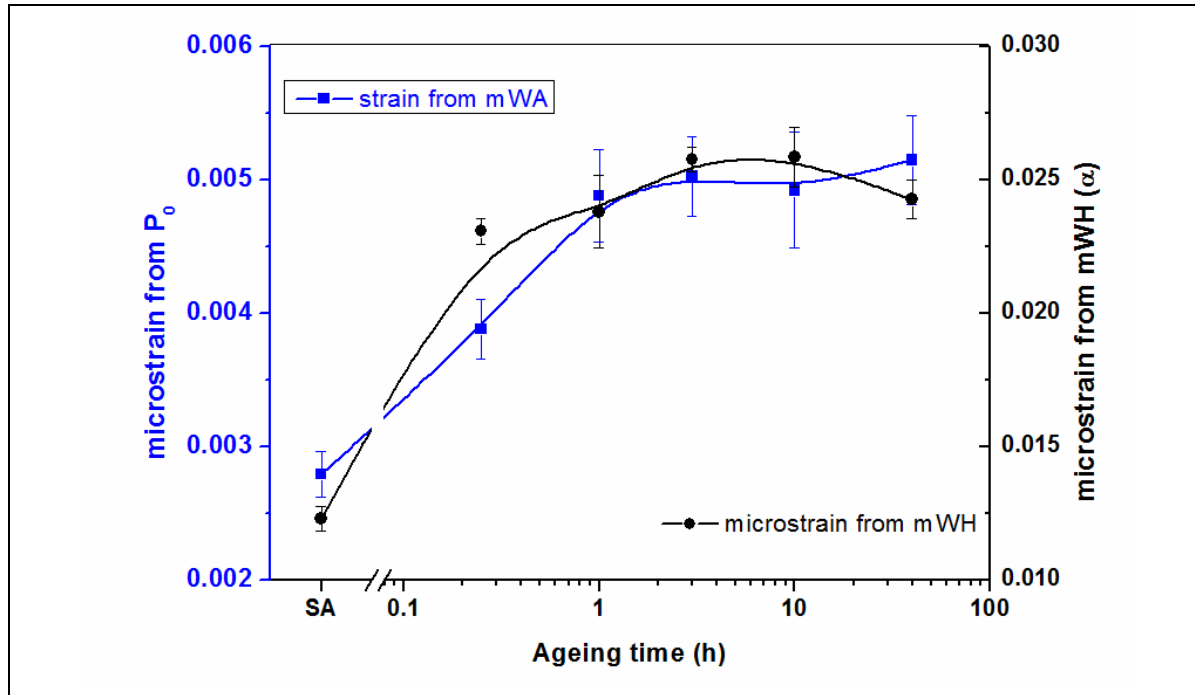


Fig. 5.8 Variation of strain estimated from  $P_0$  based on modified WA analysis and normalized mean square strain  $\alpha$  estimated from mWH analysis with ageing duration

#### 5.2.4 Precipitation fraction from lattice changes

Based on the literature presented in §1.4 (p. 7) and further elaborated in §4.3.1 (p. 64), the fraction of precipitates formed could be evaluated from changes in lattice parameter. However, in maraging steel, it is well known that strengthening of the steel occurs due to the combined presence of hexagonal  $\text{Ni}_3(\text{Ti}, \text{Mo})$  and  $\text{Fe}_2\text{Mo}$  intermetallic precipitates [29,30]. Detailed literature on the precipitation behaviour of maraging steel was presented in §1.5.2 (p. 12). The matrix becomes lean of Ni due to the formation of precipitates, and their impact on changes in lattice parameter was presented in §4.3.1. The effect of Ni addition on lattice parameter of Fe-Ni alloys was presented in Fig. 4.11b. Similarly, Ti present in the matrix joins with Ni to form  $\text{Ni}_3\text{Ti}$  making the matrix lean of Ti. Since, Ti is available as a high temperature phase in bcc structure, the atomic volume of Ti can be arrived at from the lattice parameter of this phase. The effect of addition of Ti to Fe-Ti

binary alloy systems is shown in Fig. 5.9. The inset to the figure shows the changes in lattice parameter at lower concentrations of Ti. A linear relationship is valid in this Fe-Ti system. Hence, the volume occupied by each atom of Ti in a unit cell is estimated as  $1.86 \times 10^{-29} \text{ m}^3/\text{cell}$ . The value of  $1.76 \times 10^{-29} \text{ m}^3/\text{cell}$  used by Guo et al. [26] is arrived at based on volume occupied in hexagonal closed pack (hcp) structure. Molybdenum being stable in bcc structure, the atomic volume has been assumed to be same in maraging steel. Cobalt is found in fcc structure and from the PDF card 00-015-0806, the volume occupied by each atom is estimated as  $1.11 \times 10^{-29} \text{ m}^3/\text{cell}$ . However, as per the distance of closest approach, the volume occupied by Co atom in bcc structure of maraging steel is  $1.21 \times 10^{-29} \text{ m}^3/\text{cell}$ . Since Co is an alloying element, the modified volume of Co has been used to estimate the theoretical lattice parameter of M250 grade maraging steel. However, Co does not have any influence on the changes in lattice parameter during precipitation.

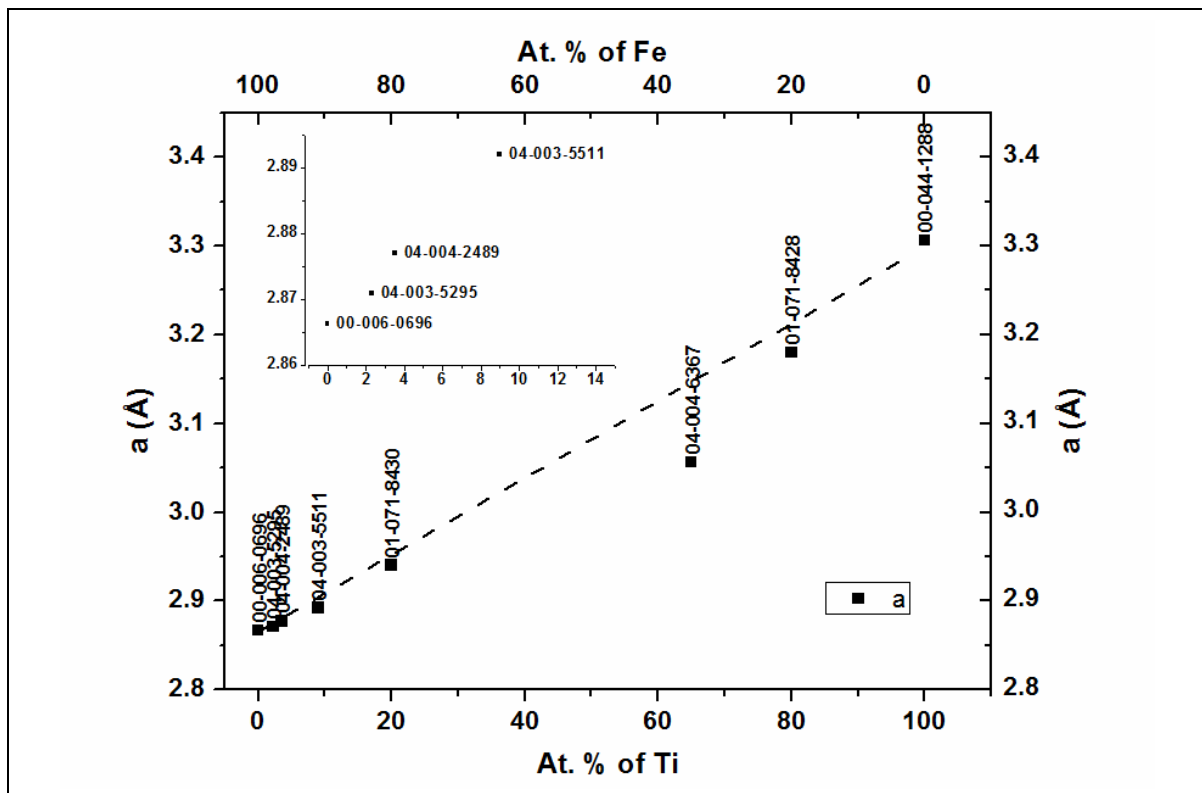


Fig. 5.9 Variation of lattice parameter of Fe-Ti bcc alloys with Ti concentration (The legends indicate the Powder diffraction file available from ICDD)

Based on the chemical composition of maraging steel presented in Table 3.3 (p.43), and the volume occupied by each of the alloying elements as listed in Table 4.1 (p.67) along with the volume of Ti and Co presented above, the lattice parameter of solutionized maraging steel is estimated as 2.8840 Å. The measured lattice parameter of solution annealed maraging steel used in this study is 2.8843 Å, well in agreement with theoretical estimates.

Theoretical estimates of changes in lattice parameter due to these 3 different types of precipitates have been obtained. The calculated decrease in lattice parameter due to precipitation of these precipitates is shown in Fig. 5.10a. The precipitate fractions have been estimated based on the assumption that these precipitates form with hcp structure with 4 atoms per unit cell. (PDF card No. 00-051-1169 for  $\text{Ni}_3\text{Ti}$ , PDF card No. 00-006-0622 for  $\text{Fe}_2\text{Mo}$  and PDF card No. 00-050-1094 for  $\text{Ni}_3\text{Mo}$  with hcp structure) These calculations are at variance with the findings reported by Guo et al. [26] and shown in Fig. 1.2 (p. 9). This is due to the changes in atomic volume considered in this study.

The measured changes in lattice parameter of maraging steel samples heat treated for various ageing durations is shown in Fig. 5.10b. The observed decrease in lattice parameter during initial ageing is consistent with the theoretical estimates based on the formation of  $\text{Ni}_3(\text{Ti},\text{Mo})$ . In maraging steels various studies have shown that in early stages of precipitation  $\text{Ni}_3\text{Ti}$  forms and  $\text{Fe}_2\text{Mo}$  is reported in later stages of precipitation [42,146]. The marginal increase in lattice parameter on 10 h of ageing is due to dissolution of initial precipitates, which occurs before the formation of austenite [34,146]. The large change in lattice parameter observed on ageing from 10 to 40 h is consistent with the formation of  $\text{Fe}_2\text{Mo}$  (as seen by the blue line in Fig. 5.10a). The more or less constant



lattice parameter observed between 40 and 100 h of ageing shows that increase in austenite fraction from 2 to 30% does not influence the lattice parameter.

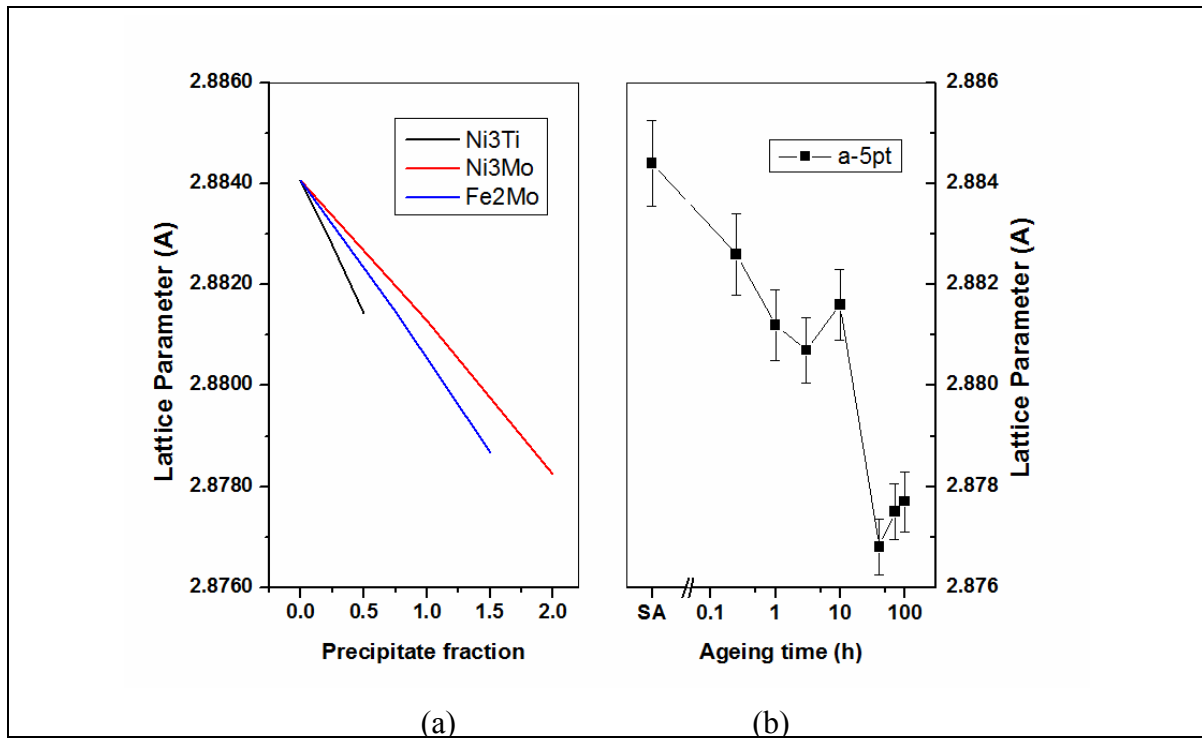


Fig. 5.10 (a) Calculated variation of lattice parameter for different types (Ni<sub>3</sub>Ti, Ni<sub>3</sub>Mo and Fe<sub>2</sub>Mo) of precipitates (b) Measured variation of lattice parameter with ageing time

Vasudevan et al. [29], in their energy dispersive X-ray microanalysis of precipitates obtained on long term ageing of C250 grade steel found substantial amount of Mo substituting Ti in the Ni<sub>3</sub>Ti. Similar inferences were recorded by Viswanathan et al. [42] in their studies on 350 grade maraging steel. Hence, the change in the  $a$  value of the matrix due to the depletion of Ni, Ti and Mo to form intermetallics, gives an average slope of  $da/dx$  of  $-4.09\text{E-}3$  Å/precipitate fraction. Based on this slope, the precipitate fraction is estimated from changes in lattice parameter and is shown in Fig. 5.11 as blue filled circles. It is to be noted that the precipitate fraction estimated on 40 h of ageing from lattice parameter changes would be larger. However, considering the fact that the normalized mean square strain decreases on 40 h of ageing due to the precipitates becoming incoherent, the precipitate fraction has been normalized to the maximum change in lattice

parameter observed in 3 h condition. As discussed earlier, the large decrease in lattice parameter from 10 to 40 h is due to the formation of  $\text{Fe}_2\text{Mo}$ . To confirm the estimates of precipitate fraction, the precipitation kinetics studied from hardness measurements and shown in Fig. 5.1b is redrawn in Fig. 5.11 as black filled square. As discussed in §4.3.3 (p. 69), hardness based study of kinetics of the precipitation process would provide information in a normalized scale of 1. The hardness changes have been converted to precipitate fractions based on the results obtained from lattice parameter changes. Despite the presence of 3 different precipitates, the agreement between the fractional estimates based on the 2 different approaches is reasonable.

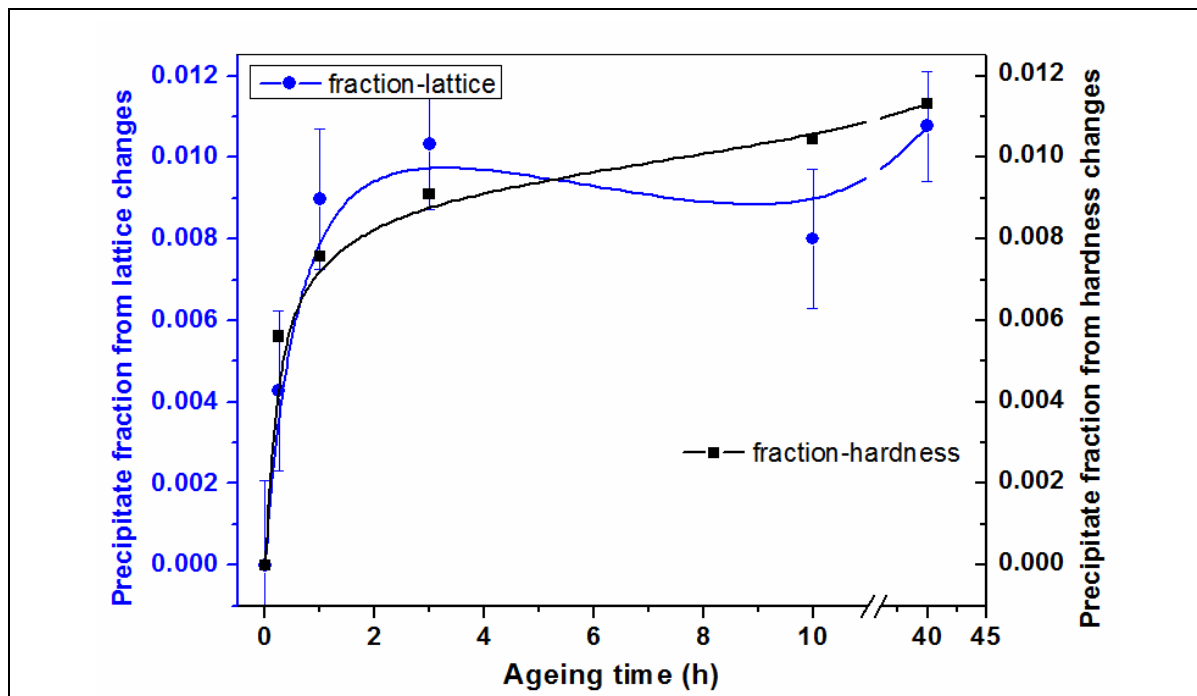


Fig. 5.11 Variation of precipitate fraction estimated from changes in lattice parameter (blue dots) and from hardness changes (black filled square)

### 5.3 Precipitate radius from activation energy

Similar to the approach followed in the studies on 17-4 PH steel, the estimate of precipitate radius can be carried out from activation energy §4.5 (p.74). Since the study carried out herein is limited to isothermal ageing at one temperature, activation energy for the precipitation process cannot be deduced from this data. Hence, the activation energy

of precipitation process of similar steels has been analyzed and accordingly chosen from literature. Peters and Cupp [43] had analyzed the kinetics of various 18% Ni maraging steels including the 250 grade with and without Co using hardness and resistivity measurements. Using the time to reach 80% of peak value of resistivity or hardness, the authors estimated an activation energy of 42.8 kcal per mole (180 kJ/mol) for the 3 alloys. Vasudevan et al. [29] estimated an activation energy by determining the time to reach a particular fraction which was arrived at from resistivity measurements. A value of 101 kJ/mol at a fraction of 25%, which increased to 181 kJ/ mole at a fraction of 75% was arrived at in T250 and C250 grade (T-250 grade steel has more of Ti and has very little Co) maraging steels. Guo et al. [26] studied the phase transformation kinetics of C250 grade maraging steel from differential scanning calorimetry measurements and compared the same with modeling and estimated an activation energy of 205 kJ/mol for the precipitation process. Hence this value of activation energy is used along with the diffusion coefficient of Ni [147] to estimate the radius of precipitates based on Zener's law. The estimated radius of precipitates and the normalized mean square strain with ageing condition are listed in Table 5.3. The estimated precipitate radius is 25 Å on ageing for 10 h. Similar to the observations made in 17-4 PH steel, the theoretical estimates are compared with the critical radius ( $R \approx \frac{b}{3|\epsilon|}$ ) of the precipitate above which the precipitates become incoherent [49]. For a peak microstrain of 0.026 (10 h), the critical radius is 32 Å. The estimated radius is below this value. Studies by Vasudevan et al. [29] had estimated the average precipitate diameter as ~ 4.5 nm after 3 h of ageing, from TEM evaluations. This value is close to the value estimated here. As the precipitate size grows to 50 Å, the microstrain decreases indicating that the precipitates are incoherent with the matrix.

The lattice mismatch between the close packed directions of the matrix and the Ni<sub>3</sub>Ti precipitates is 2.22 % [29]. The microstrain estimated herein is close to this value. This

misfit could be accommodated by an edge dislocation spaced 25 atomic planes apart. From this analysis, the authors [29] had suggested that precipitates with size less than 10 nm would be coherent, while larger ones become semicoherent. The geometric criterion for coherency to exist between the matrix and the precipitate is given by the condition  $\Delta t \cdot \epsilon \leq |\mathbf{b}|$  where  $\Delta t$ ,  $\epsilon$  and  $\mathbf{b}$  represent the precipitate-matrix interface length, misfit strain and Burgers vector respectively [102]. In M250 steel, for a  $b$  value of 2.5 Å, leads to an interface length of 10 nm and it is felt that, the critical radius is a better parameter for determining whether the precipitates are coherent or incoherent.

Table 5.3 Estimated radius of precipitates and normalized mean square strain under different ageing conditions

Ageing duration	Estimated radius from Zener's equation (Å)	Normalized mean square strain from mWH approach (eqn. 2.23) $\pm 0.001$ max
Solution annealed	Nil	0.0123
0.25 h	4	0.023
1 h	8	0.0237
3 h	14	0.0257
10 h	25	0.0258
40 h	50	0.0242

Viswanathan et al. [42], found that the average precipitate size was ~40 nm in length and 2.5 nm in thickness in samples of M350 grade maraging steel aged at 510 °C (783 K) for 3 h. These precipitates were identified as rod shaped. Yi He et al. [148] studied the microstructure of 2000 MPa Co-free maraging steel aged at 753 K using TEM investigations. They found Ni<sub>3</sub>Ti precipitates of diameter 5 nm, and length around 15 nm in 3 h aged specimens. The radii estimated in this study are similar to these observations,

though the grades are different. However, the theoretically estimated radius, microstrain and precipitate fraction arrived at from XRD profile analysis would be used to evaluate the various precipitate strengthening mechanisms in the following section.

#### **5.4 Strengthening in M250 grade maraging steel**

Vasudevan et al. [29] attempted to analyze the increase in strength of T250 grade steel by means of Orowan relationship by estimating the interparticle spacing from precipitate fraction and diameter. They found reasonable agreement between the measured (1723 MPa) and calculated value (1540 MPa) for samples aged at 482 °C (753 K) for 6 h. However, the authors further concluded that the increase in strength is governed by the coherency stresses and internal ordering of precipitates. It is to be noted that the Orowan relationship that was adapted by them is valid at longer ageing times. Similarly, Viswanathan et al. [42] suggested that under peak aged condition, order hardening and coherency strain hardening make significant contributions to strengthening and hence they need to be considered. Pereloma et al. [149] in their studies on Fe-20Ni-1.8Mn-1.5Ti-0.59Al maraging steels aged at 550 °C using 3D atom probe propose that the strengthening arises from the extra energy required for dislocation to cut a diffuse antiphase boundary formed by the pairing of solute species. Seetharaman et al. [102] analyzed the various precipitation strengthening mechanisms active in PH 13-8 Mo stainless steel. The NiAl precipitates which strengthen this material were having ordered structure. Hence, the strength increase on ageing was analyzed by including the coherency, modulus and order strengthening, but they found significant differences between the measured strength and calculated strength. Hence, it is proposed to evaluate theoretically, the strengthening contributions due to coherency, modulus and order strengthening.

### 5.4.1 Order strengthening

As the name implies, the ordered nature of the coherent precipitates causes order strengthening. An antiphase boundary (*apb*) forms on the slip plane of the precipitate phase, when a matrix dislocation shears an ordered precipitate. The energy contained in the *apb*  $\gamma_{apb}$ , leads to an increased resistance to dislocation motion. In materials with ordered precipitates, the dislocations move in pairs, as the dislocation which first created the *apb*, disturbs the order and a second dislocation is necessary to maintain order [50,150]. Hence the increase in yield stress due to order strengthening is given by

$$\Delta\tau_{ord} = \frac{\gamma_{apb}}{2b} \left[ \left( \frac{3\pi^2 \gamma_{apb} f r}{32T} \right)^{1/2} - f \right] \quad - - ( 5.4 )$$

where,  $f$  and  $r$  denote precipitate fraction and radius.  $T = 1/2Gb^2$ , where  $G$  and  $b$  are shear modulus and Burgers vector respectively [50,150].

### 5.4.2 Hardness and Yield strength

Based on the formalism explained in §4.6.1 (p.81), the hardness is converted to yield strength and both the values are given in Table 5.4. Rajkumar et al. [151] had estimated the yield strength of a few samples with similar heat treatment conditions studied here and these values are listed in the last column of Table 5.4. The converted yield strength and measured yield strength compare well with each other and the maximum deviation is 100 MPa. Hence, the converted yield strength is used further to compare with the values of the different strengthening mechanisms in the following section.

Table 5.4 Values of hardness, converted yield strength and measured yield strength [151] under different ageing conditions

Ageing condition	Hardness (VHN)	Converted YS (MPa)	Measured YS (MPa) <sup>[151]</sup>
SA	329	1053	920
0.25 h	481	1539	1433
1 h	503	1609	--
3 h	552	1766	1791
10 h	581	1859	1795
40 h	603	1929	--

#### 5.4.3 Estimation of strengthening contributions

Based on the literature presented on the active strengthening mechanisms in this class of steel, the coherency strengthening (§4.4.3.1, p. 73), modulus strengthening (§4.4.3.2, p. 74) and order strengthening (§5.4.1) contributions are estimated. The variables in these equations  $\varepsilon$ ,  $r$  and  $f$  have been estimated and were presented in Table 5.3 and in Fig. 5.11 of §5.2.4. Since the fraction of precipitates ( $f$ ) estimated was almost similar from both the approaches (based on hardness and changes in lattice parameter), the strengthening has been estimated using precipitate fraction estimated from changes in lattice parameter only. (It may be recalled that, in 17-4 PH steel, the precipitate fractions estimated from change in hardness and lattice parameter were different in a few of the ageing conditions as shown in Table 4.2, p. 70. Hence, the strengthening contribution was calculated using precipitate fractions estimated by both the approaches in 17-4 PH steel and compared.)

Towards estimating the various precipitate strengthening contributions, the shear modulus of the matrix in solution annealed condition and the precipitate modulus are required. For the maraging steel samples used in this study, Rajkumar et al. [30] had estimated a shear wave velocity ( $v_s$ ) of 2853 m/s in solutionized condition. A shear modulus ( $G$ ) of 65.5 GPa is estimated by using this velocity along with the measured density using the relation

$G = \rho v_s^2$  [152]. This value is in agreement with the shear modulus ( $G$ ) of 66 GPa estimated for 250 grade maraging steel [152]. The modulus of  $\text{Ni}_3\text{Ti}$ , reported in literature is 96 GPa [153,154]. This value is used for estimating the modulus strengthening using eqn. 4.5 in p. 74.

Similarly, another variable that is required is the energy of the *apb* formed in the ordered precipitate namely  $\text{Ni}_3\text{Ti}$ . The energy of the *apb* is [102,155] given as

$$\gamma_{apb} = \frac{8s^2RT_c}{2.18 \cdot 3\sqrt{3}a^2N} \quad - - (5.5)$$

where  $T_c$  is the critical temperature for the order-disorder transition,  $N$  is the Avogadro number,  $R$  is the gas constant,  $a$  is the lattice parameter and  $s$  is a constant close to unity. Seetharaman et al. [102], while considering  $\text{NiAl}$  precipitates in PH 13-8 Mo SS, assumed  $T_c$  to be the melting point of  $\text{NiAl}$  to estimate  $\gamma_{apb}$ . Similarly, assuming  $T_c$  as the melting point of  $\text{Ni}_3\text{Ti}$ , which is 1583 K as estimated by Nunomura et al. [156] yields a value of  $\gamma_{apb}$  as 186 mJ/m<sup>2</sup>. Due to the difficulties that exist in accurately determining  $\gamma_{apb}$ , Ardell [150] compared the  $\gamma_{apb}$  values used in various alloy systems. A value of 135 mJ/m<sup>2</sup> is reported for  $\text{Ni}_3\text{Al}$  precipitates by Ardell [150] in Ni-16%Al alloy. The author also concluded that  $\gamma_{apb}$  increases with increasing Ti content of these precipitates. In an iron based alloy strengthened by  $\text{Ni}_3\text{Ti}$  precipitates, a value of 190 mJ/m<sup>2</sup> has been arrived at by fitting the experimentally measured increase in strength with precipitate diameter [157]. Hence, the value of 186 mJ/m<sup>2</sup> is in agreement with this value and is used for estimating the order strengthening contribution.

As presented in §1.5.2 (p. 12), order and coherency strengthening play a key role in these class of steels. Hence, the strengthening contribution due to these two strengthening mechanisms in addition to the modulus strengthening are estimated and compared with the converted yield strength. Hence the yield strength  $YS$  is given by



$$YS = YS_o + k_1 \sqrt{(\Delta\tau_{mod}^2 + \Delta\tau_{coh}^2 + \Delta\tau_{ord}^2)} \quad \text{-- ( 5.6 )}$$

where  $YS_o$  corresponds to the yield strength when none of the strengthening mechanisms act and this value should be close to the  $YS$  of the solution annealed sample. The variation of calculated increase in strength (as given by term 2 on the RHS of eqn. 5.6) with measured strength is shown in Fig. 5.12. The observed linear fit in the ageing regime is shown in the figure. The intercept of the plot is  $\sim 1390 \pm 40$  MPa. This value is higher than the  $YS$  of the solution annealed sample. If coherency strengthening and order strengthening are only considered, the intercept is 1460 MPa. Hence, it is shown that modulus strengthening also plays a role in the strengthening behaviour of maraging steel.

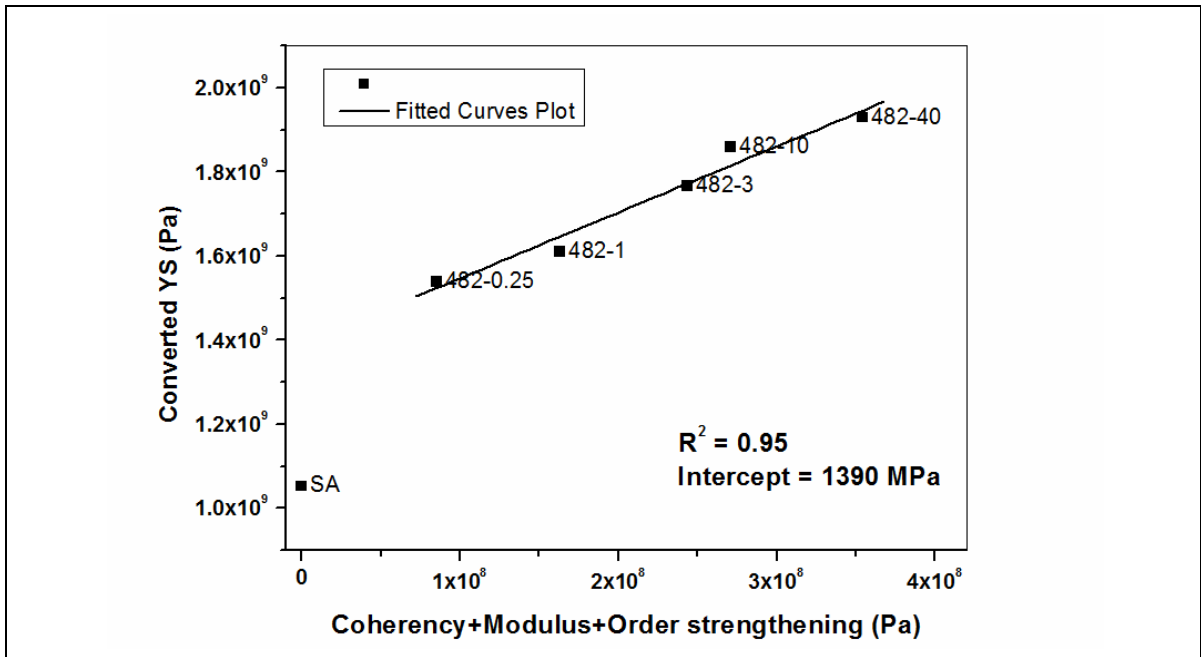


Fig. 5.12 Variation of converted yield strength (from hardness) with coherency + modulus + order strengthening

Similar to the observations made in 17-4 PH steel, microstructural changes take place in maraging steel during ageing. The microstructural changes were reflected by the changes in crystallite size (Table 5.1) and from the observed variation in dislocation density as presented in Table 5.2. Hence, in addition to the precipitate strengthening effects, the

effect of changes in dislocation density is considered and the change in yield strength is given as

$$YS = YS_o + k_1 \sqrt{(\Delta\tau_{mod}^2 + \Delta\tau_{coh}^2 + \Delta\tau_{ord}^2)} + (\alpha'Gb)\rho^{0.5} \quad - - (5.7).$$

The above equation is a planar equation, with the third term representing the Hall-Petch strengthening contribution due to changes in dislocation density.  $\alpha'$  is a constant with a value in the range of 0.15 to 0.5 [50]. The variation of yield strength with the precipitate strengthening and dislocation strengthening is shown in Fig. 5.13. The planar fit obtained is also shown in the figure. The plane deviates from the measured strength with a residue less than 20 MPa in all the ageing conditions except by 40 MPa in the 1 h aged condition. The adjusted  $\bar{R}^2$  value is 0.96 with an intercept of 998 MPa. The constant  $\alpha'Gb$  is estimated as 3.6 Pa.m.

By considering order and coherency strengthening contribution (excluding modulus strengthening) along with dislocation strengthening, the intercept obtained is 1126 MPa which is higher than the value obtained when modulus strengthening is considered.

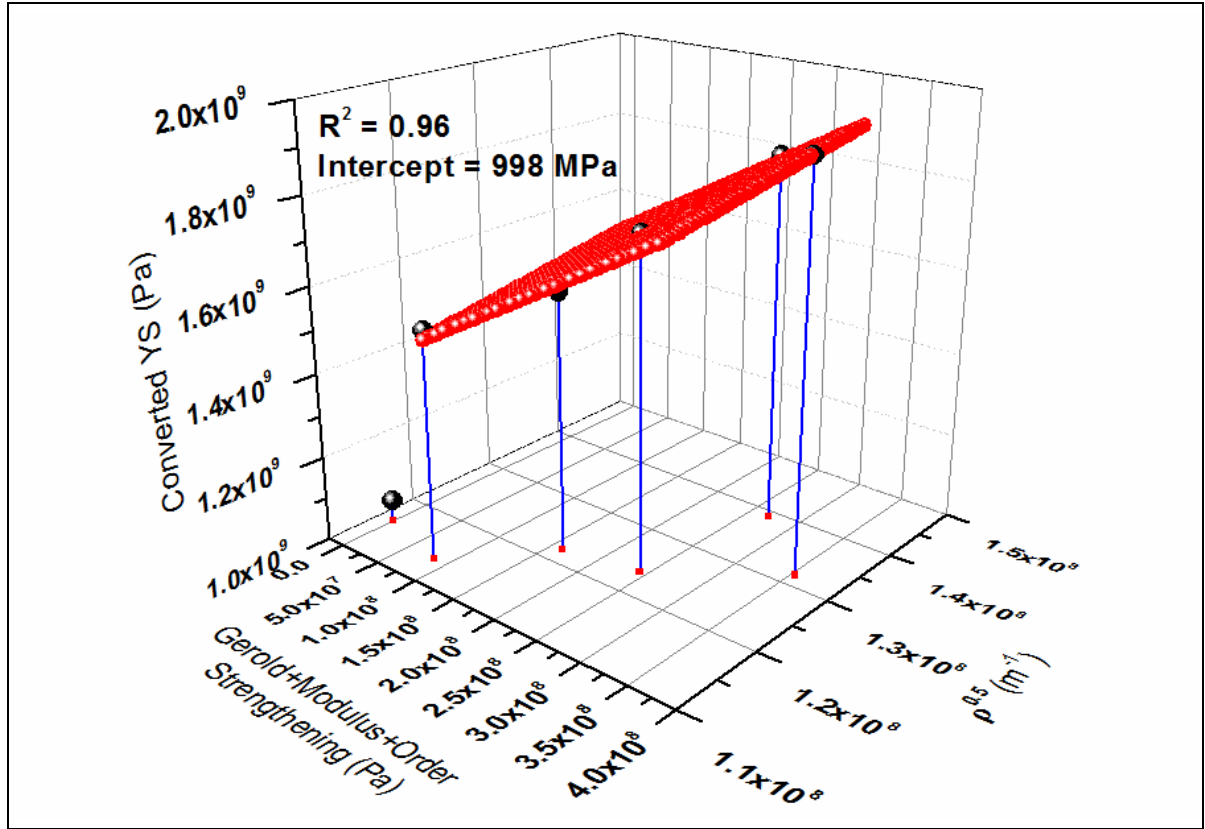


Fig. 5.13 Variation of yield strength with precipitate strengthening and dislocation strengthening based on eqn. 5.7. x and z axis in (Pa), y axis in ( $m^{-1}$ )

#### 5.4.4 Discussions on estimated constants

The intercept ( $YS_0$ ) value decreased from 1390 MPa to 998 MPa when the contribution from dislocations to strengthening is considered. This value is close to the YS obtained in the solution annealed condition. Hence it is clear that the change in microstructure of the matrix which occurs during ageing in addition to precipitation plays a significant role in strengthening of maraging steel. By substituting the  $G$  value of the matrix as 66 GPa (p. 109) and Burgers vector as  $2.5 \text{ \AA}$ , to the constant  $\alpha'Gb$  determined yields  $\alpha'$  as 0.21. An  $\alpha'$  value in the range of 0.1 to 0.3 has been arrived at for various alloy systems [126].

In 17-4 PH steel, the analysis included the solution annealed sample and an intercept lower than the strength of solution annealed sample was observed. In maraging steel, it is to be noted that the solution annealed sample is not included in the fit. Further, the higher value of intercept is analyzed from the literature available on order strengthened alloys. Martin

[50] has presented the order strengthening behaviour of Co-Ni-Cr superalloy based on studies carried out by Chaturvedi et al. [155] and had shown that a positive intercept is arrived at when order strengthening is considered based on eqn. 5.4 (p. 108). Fig. 5.14, reproduced from Chaturvedi et al [155], shows the variation of observed strengthening with theoretically estimated strengthening evaluated based on order strengthening. More clearly, the observed strength ( $\Delta$  symbols) is more than the theoretically estimated strength, similar to the behaviour observed here.

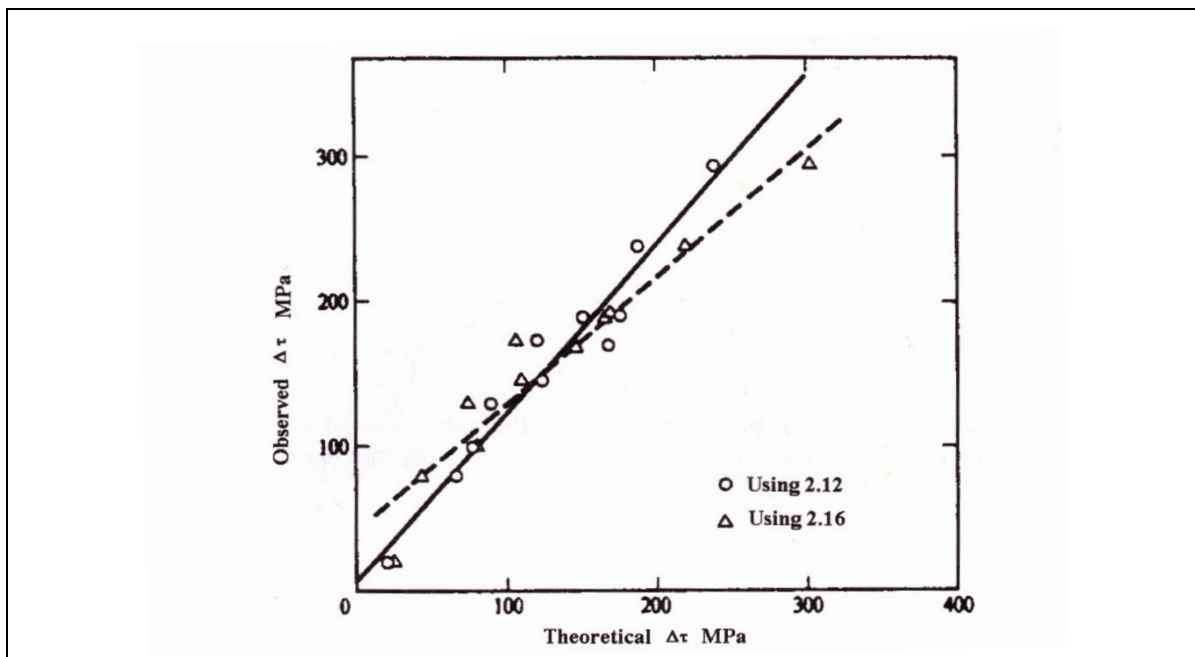


Fig. 5.14 Variation of observed vs. theoretical values of  $\Delta\tau$  during ageing of Co-Ni-Cr superalloy,  $\Delta$  (using 2.16) indicate order strengthening estimated based on eqn. 5.4 in p.108, while  $\circ$  (using 2.16) indicate coherency strengthening estimated based on eqn. 4.4 in p.73 (Figure 9 of Chaturvedi et al. [155])

Based on the analysis carried out herein, it is clear that the increase in strength of maraging steel during ageing is due to the combined effect of precipitation strengthening and dislocation strengthening or grain boundary strengthening. The contribution of precipitation strengthening arises from the coherency strain between the matrix and the precipitate, the ordered precipitates and due to the difference in modulus between precipitate and matrix.

## 5.5 Summary

- ✓ The Avrami exponent is determined as 0.34 from changes in hardness and from changes in microstrain which match well with the published value of 0.35 [29] and 0.39 [43].
- ✓ The anisotropic broadening observed in Williamson-Hall plot is addressed using the modified WH approach which is based on the contrast caused by dislocations. The slope of the modified WH plot is used to arrive at the normalized mean square strain and is found to be a better parameter to estimate the coherency strains arising due to precipitation. A drastic increase in microstrain by ~100% has been observed upon ageing to 0.25 h. This is attributed to the coherency strains caused by early precipitation of intermetallics. This observation assumes significance as early precipitation is reflected only as streaking in TEM up to 1 h of ageing [29] and clear XRD peaks of precipitates are observed only after 40 h of ageing. The small crystallite size estimated from intercept of modified WH plot in solution annealed condition is associated with the dislocation substructure.
- ✓ The average dislocation density determined based on the modified WA analysis is in agreement with the nonlinear ultrasonic (NLU) parameter ( $\beta$ ), which is the ratio of the amplitudes of the second and first harmonics of the ultrasonic wave. It is known that the  $\beta$  parameter is a strong function of dislocation density and coherency strains.
- ✓ The Wilkens parameter (M) and effective cut-off radius of dislocations ( $R_e$ ) have been determined and used to comment on the changing nature of the strain fields due to dislocations.

- ✓ The variation of mean square strain  $\langle \varepsilon^2(L) \rangle$  as a function of column length,  $L$  has been used to understand the strain fields due to dislocations and precipitates. The variation has been fitted to an equation of the form  $P_0 + P_1/L + P_2/L^2$  to determine the coefficients.
- ✓ The variation of long range strain ( $P_0$ ) estimated from the plot of  $\langle \varepsilon^2(L) \rangle$  vs  $L$  is shown to be analogous to the normalized mean square strain estimated from the mWH plot.
- ✓ The simple approach of determining precipitate fraction from changes in lattice parameter has been adapted to maraging steel where 3 different types of precipitates form. The precipitate fraction estimated matches with the estimation based on changes in hardness.
- ✓ Similar to the studies carried out in 17-4 PH steel, the strengthening contribution of the precipitates has been estimated by considering coherency strengthening, modulus strengthening and order strengthening. The important variables required for estimating these strengthening contributions have been arrived at from XRD/LPA. The theoretically estimated strength matches well with the measured strength when the effect of dislocations to strengthening the matrix is also taken into account.
- ✓ The constants to the strengthening terms are determined by the unique approach of correlating measured strength with calculated strength due to precipitates and the matrix strength that arises due to dislocations. The estimated constants agree well with published literature.

# Chapter – 6

## 6 Conclusions and future scope

The summary provided in §4.7 (p. 83), elucidates in detail the results obtained from this study on 17-4 PH steel. Similarly, §5.5 (p. 115) summarizes the key results obtained from the isothermal ageing studies carried out on M250 grade maraging steel. The following section brings out the salient points and tries to compare the results obtained in the two age hardenable materials using XRD line profile analysis.

### 6.1 Conclusions

The studies carried out on two precipitation hardenable systems clearly established that the changes in microstrain, crystallite size and lattice parameter derived from XRD profile analysis could gainfully be employed to understand the microstructural evolution and to correlate them with the hardness changes that occur during ageing of these two materials. The major conclusions from this study are:

- ✓ The Avrami exponent has been determined from changes in hardness in both the steels and agrees well with the published literature. In M250 grade maraging steel, the Avrami exponent determined from changes in microstrain agrees with the exponent determined based on hardness.
- ✓ It is shown that early precipitation can be inferred from increase in microstrain.
- ✓ A simple approach is presented for theoretically determining the lattice parameter and is used to estimate the precipitate fraction at volume fractions below 2%.
- ✓ Linking of Larson-Miller parameter with hardness and microstrain in the overageing and incoherent regime is consistent with the softening regime, in which this approach is adapted, for the first time.

- ✓ The radius of precipitates has been calculated from diffusion coefficient and activation energy.
- ✓ The increase in strength of two precipitation hardenable steels during ageing has been uniquely linked with a new 3-dimensional planar equation. The strengthening contributions from the precipitates and due to the microstructural changes in the matrix are added to compare with the experimentally measured strength. Theoretical estimates of increase in strength due to various precipitate strengthening mechanisms were evaluated using microstrain and precipitate fraction estimated from the XRD profile analysis. The change in strength due to microstructural changes were evaluated from crystallite size variations in 17-4 PH steel and dislocation density variations in maraging steel.
- ✓ The unique approach of adding the various precipitation strengthening mechanisms and comparing them with measured strength clearly shows that coherency and modulus strengthening act in tandem with grain boundary strengthening leading to the improved strength of 17-4 PH steel during ageing.
- ✓ In M250 grade maraging steel, order strengthening acts together with other precipitate strengthening mechanisms. This approach can be used to evaluate the strengthening mechanisms active in other precipitation hardenable steels.
- ✓ The study carried out clearly shows that XRD profile analysis can be used as a tool to investigate the microstructural changes that take place during early precipitation, coarsening and phase evolution. The parameters estimated from XRD profile analysis, like lattice parameter, microstrain, crystallite size and dislocation density have been used to understand the microstructural changes that occurs during ageing.



## 6.2 Future scope

The studies carried out in this work have clearly demonstrated the applicability of the modified WH and WA approaches to study ageing induced changes in precipitation hardenable materials, notwithstanding the approach being based on dislocation contrast as the cause of anisotropic broadening. It would be worthwhile to address the following issues for better understanding:

- The linking of strain and crystallite size estimated from XRD/LPA with hardness needs validation in materials where other strengthening mechanisms like work hardening and stacking fault strengthening play a key role and in materials with different crystal structures.
- In the age hardening regime, further studies with in-situ heat treatment and XRD data acquisition using Synchrotron radiation would enable estimating and understanding the fine microstructural changes that take place at shorter ageing durations.
- The variation of hardness with the tempering parameter in the age hardening regime (with a single value of material constant  $C$ ) needs to be investigated further by studying different precipitation hardenable systems.
- Studies on systems where dislocation density alone changes would further enhance the understanding of profile broadening due to dislocations and precipitation induced changes.
- Theoretical studies on the similarity of precipitation induced strain with that of the strain induced due to dislocations would improve the applicability of XRD/LPA in understanding the precipitation behaviour.



## References

- 1 Bragg WH, Bragg WL. The reflection of X-rays by crystals. *Proc. R. Soc. Lond. A.* 1913;88:428-438.
- 2 Debye P, Scherrer P. *Physik. Z.* 1916;17:277–283.
- 3 Rietveld HM. A profile refinement method for nuclear and magnetic structures. *J. Appl. Cryst.* 1969;2:65-71.
- 4 Young RA, Mackie PE, Dreele RBV. Application of the pattern-fitting structure-refinement method to X-ray powder diffractometer patterns. *J. Appl. Cryst.* 1977;10:262-269.
- 5 Borbély A, Ungár T. X-ray line profiles analysis of plastically deformed metals. *C. R. Physique.* 2012;13:293–306.
- 6 Scardi P. Recent advancements in whole powder pattern modelling. *Z. Kristallogr. Suppl.* 2008;27 :101-111.
- 7 Mittemeijer EJ, Welzel U. The “state of the art” of the diffraction analysis of crystallite size and lattice strain. *Z. Kristallogr.* 2008;223:552-560.
- 8 Ribárik G, Ungár T, Gubicza J. MWP-fit: a program for multiple whole-profile fitting of diffraction peak profiles by ab initio theoretical functions. *J. Appl. Cryst.* 2001;34:669-676.
- 9 Scherrer P. *Nachr. Ges. Wiss. Göttingen.* 1918;26:98-100.
- 10 Ungár T. Dislocation densities, arrangements and character from X-ray diffraction experiments. *Mater. Sci. Eng., A.* 2001;309-310:14-22.
- 11 Berkum JGMv, Delhez R, Keijser THD, Mittemeijer EJ. Characterization of deformation fields around misfitting inclusions in solids by means of diffraction line broadening. *Phys. Status Solidi A.* 1992;134:335-350.
- 12 Ungár T. Microstructural parameters from X-ray diffraction peak broadening. *Scripta Mater.* 2004;51:777–781.
- 13 Williamson GK, Hall WH. X-ray line broadening from fcc Aluminium and Wolfram. *Acta Metall.* 1953;1:22-31.
- 14 Warren BE, Averbach BL. The separation of cold-work distortion and particle size broadening in X-ray patterns. *J. Appl. Phys.* 1952;23:497.
- 15 Bertaut EF. *Acta Cryst.* 5. 1952 117-121.
- 16 Balzar D, Ledbetter H. Voigt-function modeling in Fourier analysis of size- and strain-broadened X-ray diffraction peaks. *J. Appl. Cryst.* 1993;26:97-103.
- 17 Ungár T, Borbély A. The effect of dislocation contrast on X-ray line broadening: A new approach to line profile analysis. *Appl. Phys. Lett.* 1996;69:3173-75.
- 18 Ungár T, Ott S, Sanders PG, Borbély A, Weertman JR. Dislocations, grain size and planar faults in nanostructured copper determined by high resolution X-ray diffraction

- and a new procedure of peak profile analysis. *Acta Mater.* 1998;46:3693-99.
- 19 Ungár T, Gubicza J, Ribárik G, Borbély A. Crystallite size distribution and dislocation structure determined by diffraction profile analysis: principles and practical application to cubic and hexagonal crystals. *J. Appl. Cryst.* 2001;34:298-310.
  - 20 Dey SN, Chatterjee P, Gupta SPS. Dislocation induced line-broadening in cold-worked Pb-Bi binary alloy system in the  $\alpha$ -phase using X-ray powder profile analysis. *Acta Mater.* 2003;51:4669-77.
  - 21 Scardi P, Leoni M, Delhez R. Line broadening analysis using integral breadth methods: a critical review. *J. Appl. Cryst.* 2004;37:381-390.
  - 22 Vermeulen AC, Delhez R. Line profile analysis (LPA) methods: Systematic ranking of the quality of their basic assumptions. *Mater. Sci. Forum.* 2004;443-444:127-130.
  - 23 Lubarda VA. On the effective lattice parameter of binary alloys. *Mech. Mater.* 2003;35:53-68.
  - 24 King HW. Quantitative size-factors for metallic solid solutions. *J. Mater. Sci.* 1966;1:79-90.
  - 25 Hume-Rothery W. Atomic diameters, atomic volumes, and solid solubility relations in alloys. *Acta Metall.* 1966;14:17-20.
  - 26 Guo Z, Li D, Sha W. Quantification of precipitate fraction in maraging steels by X-ray diffraction analysis. *Mater. Sci. Technol.* 2004 ;20:126-130.
  - 27 Viswanathan UK, Banerjee S, Krishnan R. Effects of aging on the microstructure of 17-4 PH stainless steel. *Mater. Sci. Eng., A.* 1988;104:181-189.
  - 28 Viswanathan UK, Nayar PKK, Krishnan R. Kinetics of precipitation in 17-4 PH stainless steel. *Mater. Sci. Technol.* 1989;5:346-349.
  - 29 Vasudevan VK, Kim SJ, Wayman CM. Precipitation reactions and strengthening behavior in 18 wt. pct nickel Maraging steels. *Metall. Trans. A.* 1990;21A:2655-2668.
  - 30 Rajkumar KV, Kumar A, Jayakumar T, Raj B, Ray KK. Characterization of aging behavior in M250 grade maraging steel using ultrasonic measurements. *Metall. Mater. Trans. A.* 2007;38A:236-243.
  - 31 Guo Z, Sha W, Li D. Quantification of phase transformation kinetics of 18 wt.% Ni C250 maraging steel. *Mater. Sci. Eng., A.* 2004;373:10-20.
  - 32 Mahadevan S, Jayakumar T, Rao BPC, Kumar A, Rajkumar KV, Raj B. X-ray diffraction profile analysis for characterizing isothermal aging behaviour of M250 grade maraging steel. *Metall. Mater. Trans. A.* 2008;39A:1978-1984.
  - 33 Rai SK, Kumar A, Shankar V, Jayakumar T, Rao KBS, Raj B. Characterization of microstructures in Inconel 625 using X-ray diffraction peak broadening and lattice parameter measurements. *Scripta Mater.* 2004;51:59-63.
  - 34 Viswanathan UK, Kutty TRG, Ganguly C. Dilatometric technique for evaluation of the kinetics of solid-state transformation of maraging Steel. *Metall. Trans. A.*

1993;24A:2653–2656.

- 35 Hsiao CN, Chiou CS, Yang JR. Aging reactions in a 17-4 PH stainless steel. *Mater. Chem. Phys.* 2002;74:134-142.
- 36 Bhattacharya DK, Jayakumar T, Moorthy V, Vaidyanathan S, Raj B. Characterization of microstructures in 17-4-PH stainless steel by magnetic Barkhausen noise analysis. *NDT & E Int.* 1993;26:141-148.
- 37 Miller MK, Burke MG. Characterization of copper precipitation in a 17/4 PH steel: A combined APFIM/TEM study. 1991 CONF-910808—2.
- 38 Wang J, Zou H, Li C, Zuo R, Qiu S, Shen B. Relationship of microstructure transformation and hardening behavior of type 17-4 PH stainless steel. *J. Univ. Sci. Technol. Beijing.* 2006;13:235-239.
- 39 Murayama M, Katayama Y, Hono K. Microstructural evolution in a 17-4 PH stainless steel after ageing at 400 °C. *Metall. Mater. Trans. A.* 1999;30A:345-353.
- 40 Miller GP, Mitchell WI. Structure and hardening mechanisms of 18 % Nickel-Cobalt-Molybdenum Maraging steels. *J. Iron Steel Inst.* 1965;203:899–904.
- 41 Floreen S, Decker RF. Heat Treatment of 18% Ni Maraging Steel. In: F. DR, editor. *Source Book on Maraging Steels.* ASM, Metals Park,; 1979. p. 20–32.
- 42 Viswanathan UK, Dey GK, Asundi MK. Precipitation hardening in 350 grade Maraging steel. *Metall. Trans. A.* 1993;24A:2429-2442.
- 43 Peters DT, Cupp CR. The kinetics of aging reactions in 18 Pct Ni Maraging Steels. *Trans. Metall. Soc. AIME.* 1966;236:1420-29.
- 44 Sha W. Quantification of age hardening in Maraging Steels and an Ni-base Superalloy. *Scripta Mater.* 2000;42:549–553.
- 45 Preston GD. The diffraction of X-rays by age-hardening aluminium copper alloys. *Proc. R. Soc. A.* 1938;167:526.
- 46 Guinier A. On the birth of GP zones. *Mater. Sci. Forum.* 1996;217-222:3-6.
- 47 Kuhn HA, Biermann H, Ungár T, Mughrabi H. An x-ray study of creep-deformation induced changes of the lattice mismatch in the  $\gamma'$ -hardened monocrystalline nickel-base superalloy SRR 9. *Acta Metall.* 1991;39:2783-2794.
- 48 Hollomon JH, Jaffe LD. *Trans. Amer. Inst. Min. Metall. Eng.* 1945;162:223-249.
- 49 Gerold V, Haberkorn H. On the critical resolved shear stress of solid solutions containing coherent precipitates. *Phys. Status Solidi.* 1966;16:675-684.
- 50 Martin JW. *Micromechanisms in particle-hardened alloys.* Cambridge University Press, New York, NY; 1980.
- 51 Russell KC, Brown LM. A dispersion strengthening model based on differing elastic moduli applied to the iron-copper system. *Acta Metall.* 1972;20:969-974.
- 52 Caglioti G, Paoletti A, Ricci FP. Choice of collimators for a crystal spectrometer for neutron diffraction. *Nucl. Instrum.* 1958;3:223-228.

- 53 Young RA, Wiles DB. Profile shape functions in Rietveld refinements. *J. Appl. Cryst.* 1982;15:430-438.
- 54 Howard SA, Snyder RL. The use of direct convolution products in profile and pattern fitting algorithms. I. Development of the algorithms. *J. Appl. Cryst.* 1989;22:238-243.
- 55 Klug HP, Alexander LE. X-ray diffraction procedures: For polycrystalline and amorphous materials. 2nd ed. Wiley Interscience; 1974.
- 56 Warren BE. X-ray studies of deformed metals. *Prog. Metal Physics.* 1959;8:147-202.
- 57 Langford JI. A rapid method for analysing the breadths of diffraction and spectral lines using the Voigt function. *J. Appl. Cryst.* 1978;11:10-14.
- 58 Wertheim GK, Butler MA, West KW, Buchanan DNE. Determination of the Gaussian and Lorentzian content of experimental line shapes. *Rev. Sci. Instrum.* 1974;45:1369-1371.
- 59 Thompson P, Cox DE, Hastings JB. Rietveld refinement of Debye-Scherrer synchrotron X-ray data from Al<sub>2</sub>O<sub>3</sub>. *J. Appl. Cryst.* 1987;20:79-83.
- 60 Sánchez-Bajo F, Ortiz AL, Cumbreira FL. Novel analytical model for the determination of grain size distributions in nanocrystalline materials with low lattice microstrains by X-ray diffractometry. *Acta Mater.* 2006;54:1–10.
- 61 Dasgupta P. On use of pseudo-Voigt profiles in diffraction line broadening analysis. *Fizika A.* 2000;9:61-66.
- 62 Enzo S, Fagherazzi G, Bendetti A, Polizzi S. A profile-fitting procedure for analysis of broadened X-ray diffraction peaks. I. Methodology. *J. Appl. Cryst.* 1988;21:536-542.
- 63 Scardi P, Leoni M. Diffraction line profiles from polydisperse crystalline systems. *Acta Cryst.* 2001;A57 :604-613.
- 64 Jones FW. The measurement of particle size by the X-ray method. *Proc. R. Soc. Lond. A.* 1938;166:16-43.
- 65 Langford JI, Wilson AJC. Scherrer after sixty years: A survey and some new results in the determination of crystallite size. *J. Appl. Cryst.* 1978;11:102-113.
- 66 Wilson AJC. On variance as a measure of line broadening in diffractometry - General theory and small particle size. *Proc. Phys. Soc.* 1962;80:286-294.
- 67 Langford JI. The variance as a measure of line broadening: Corrections for truncation, curvature and instrumental effects. *J. Appl. Cryst.* 1982;15:315-322.
- 68 Louër D, Auffrédic JP, Langford JI, Ciosmak D, Niepce JC. A precise determination of the shape, size and distribution of size of crystallites in zinc oxide by X-ray line-broadening analysis. *J. Appl. Cryst.* 1983;16:183-191.
- 69 Stokes AR, Wilson AJC. The diffraction of X rays by distorted crystal aggregates – I. *Phy. Soc.* 1944;56:174-181.
- 70 Berkum JGMv, Delhez R, Keijser THD, Mittemeijer EJ. Diffraction-line broadening due to strain fields in materials; Fundamental aspects and methods of analysis. *Acta*

Cryst. 1996;A52:730-747.

- 71 Warren BE, Averbach BL. The effect of cold-work distortion on X-ray patterns. *J. Appl. Phys.* 1950;21:595-599.
- 72 Krill CE, Birringer R. Estimating grain-size distributions in nanocrystalline materials from X-ray diffraction profile analysis. *Philos. Mag.* 1998;77:621-640.
- 73 Smith WL. Crystallite shape and the Fourier analysis of diffraction line profiles. *J. Appl. Cryst.* 1976;9:187-189.
- 74 Mahadevan S, Behera SP, Gnanaprakash G, Jayakumar T, Philip J, Rao BPC. Size distribution of magnetic iron oxide nanoparticles using Warren-Averbach XRD analysis. *J. Alloys Compd.* 2012;73:867-872.
- 75 Keijser THD, Langford JI, Mittemeijer EJ, Vogels ABP. Use of the Voigt function in a single-line method for the analysis of X-ray diffraction line broadening. *J. Appl. Cryst.* 1982;15:308-314.
- 76 Wilson AJC. On variance as a measure of line broadening in diffractometry II: Mistakes and strain. *Proc. Phys. Soc.* 1963;81:41-46.
- 77 Sanchez-Bajo F, Cumbreira FL. The use of the pseudo-Voigt function in the variance method of X-ray line-broadening analysis. *J. Appl. Cryst.* 1997;30:427-430.
- 78 Stephens PW. Phenomenological model of anisotropic peak broadening in powder diffraction. *J. Appl. Cryst.* 1999;32:281-289.
- 79 Krivoglaz MA. Theory of X-ray and thermal neutron scattering by real crystals. New York: Plenum Press.; 1969.
- 80 Ungár T, Tichy G. The effect of dislocation contrast on X-Ray line profiles in untextured polycrystals. *Phys. Status Solidi A.* 1999;171:425-434.
- 81 Ungár T, Dragomir I, Révész Á, Borbély A. The contrast factors of dislocations in cubic crystals: the dislocation model of strain anisotropy in practice. *J. Appl. Cryst.* 1999;32:992-1002.
- 82 Turunen MJ, Keijser THD, Delhez R, Pers NMvd. A method for the interpretation of the Warren-Averbach mean-squared strains and its application to recovery in Aluminium. *J. Appl. Cryst.* 1983;16:176-182.
- 83 Jayan V, Khan MY, Husain M. Coarsening of nano sized carbide particles in 2.25Cr-1Mo power plant steel after extended service. *Mater. Lett.* 2004;58:2569-2573.
- 84 Krasnowski M, Grabias A, Kulik T. Phase transformations during mechanical alloying of Fe-50% Al and subsequent heating of the milling product. *J. Alloys Compd.* 2006;424:119-127.
- 85 Mukherjee P, Sarkar A, Barat P, Bandyopadhyay SK, Sen P, Chattopadhyay SK, Chatterjee P, Chatterjee SK, Mitra MK. Deformation characteristics of rolled zirconium alloys: a study by X-ray diffraction line profile analysis. *Acta Mater.* 2004;52:5687-5696.
- 86 Ungár T, Révész Á, Borbély A. Dislocations and grain size in electrodeposited

- nanocrystalline Ni determined by the modified Williamson-Hall and Warren-Averbach procedures. *J. Appl. Cryst.* 1998;31:554-558.
- 87 Ungár T, Balogh L, Borbély A. Defect-related physical-profile-based X-ray and neutron line profile analysis. *Metall. Mater. Trans. A.* 2010;41:1202-1209.
  - 88 Nedjad SH, Nasab FH, Garabagh MRM, Damadi SR, Ahmadabadi MN. X-ray diffraction study on the strain anisotropy and dislocation structure of deformed lath martensite. *Metall. Mater. Trans. A.* 2011;42A:2493-2497.
  - 89 Avrami M. *J. Chem. Phys.* 1941;9:177-184.
  - 90 Robino CV, Hochanadel PW, Edwards GR, Cieslak MJ. Heat treatment of investment cast PH13-8 Mo strainless steel: Part II. Isothermal aging kinetics. *Metall. Mater. Trans. A.* 1994;25A:697-704.
  - 91 Wilson EA. Quantification of age hardening in an Fe-12Ni-6Mn alloy. *Scripta Mater.* 1997;36:1179-1185.
  - 92 Hornbogen E, Glenn RC. A metallographic study of precipitation of copper from alpha iron. *Trans. Met. Soc. of. AIME.* 1960;218:1064-1070.
  - 93 Ghosh SK, Haldar A, Chattopadhyay. PP. On the Cu precipitation behavior in thermomechanically processed low carbon microalloyed steels. *Mater. Sci. Eng., A.* 2009;519:88-93.
  - 94 Mirzadeh H, Najafizadeh A. Aging kinetics of 17-4 PH stainless steel. *Mater. Chem. Phys.* 2009;116:119-124.
  - 95 Gomes C, Kaiser AL, Bas JP, Aissaoui A, Piette M. Predicting the mechanical properties of a quenched and tempered steel thanks to a “tempering parameter”. *Revue de Métallurgie.* 2010;107:293-302.
  - 96 Virtanen E, Tyne CJV, Levy BS, Brada G. The tempering parameter for evaluating softening of hot and warm forging die-steels. *J. Mater. Process. Technol.* 2013;213:1364-69.
  - 97 Vasudevan M, Venkadesan S, Sivaprasad PV, Mannan SL. Use of the Larson-Miller parameter to study the influence of ageing on the hardness of cold-worked austenitic stainless steel. *J. Nucl. Mater.* 1994;211:251-255.
  - 98 Shin JH, Jeong J, Lee JW. Microstructural evolution and the variation of tensile behavior after aging heat treatment of precipitation hardened martensitic steel. *Mat. Char.* 2015;99:230-237.
  - 99 Bruno G, Schumacher G, Pinto HC, Schulze C. Measurement of the lattice misfit of the nickel-base superalloy SC16 by high-energy synchrotron radiation. *Metall. Mater. Trans. A.* 2003;34A:193-197.
  - 100 Thompson SW, Krauss G. Copper precipitation during continuous cooling and isothermal aging of A710-type steels. *Metall. Mater. Trans. A.* 1996;27A:1573-1588.
  - 101 Harry T, Bacon DJ. Computer simulation of the core structure of the screw dislocation in  $\alpha$ -iron containing copper precipitates: I. structure in the matrix and a precipitate. *Acta Mater.* 2002;50:195-208.



- 102 Seetharaman V, Sundararaman M, Krishnan R. Precipitation hardening in a PH 13-8 Mo stainless steel. *Mater. Sci. Eng.*. 1981;47:1-11.
- 103 Fine ME, Isheim D. Origin of copper precipitation strengthening in steel revisited. *Scripta Mater.* 2005;53:115–118.
- 104 Holzer I, Kozeschnik E. Computer simulation of the yield strength evolution in Cu-precipitation strengthened ferritic steel. *Mater. Sci. Eng., A.* 2010;527:3546–3551.
- 105 Isheim D, Gagliano MS, Fine ME, Seidman DN. Interfacial segregation at Cu-rich precipitates in a high-strength low-carbon steel studied on a sub-nanometer scale. *Acta Mater.* 2006;54:841–849.
- 106 Ungár T. The meaning of size obtained from broadened X-ray diffraction peaks. *Adv. Eng. Mater.* 2003;5:323-329.
- 107 Hwang GC, Lee S, Yoo JY, Choo WY. Effect of direct quenching on microstructure and mechanical properties of copper-bearing high-strength alloy steels. *Mater. Sci. Eng. A.* 1998;252:256–268.
- 108 Huang K, Wang N, Li Y, Marthinsen K. The influence of microchemistry on the softening behaviour of two cold-rolled Al–Mn–Fe–Si alloys. *Mater. Sci. Eng. A.* 2014;601:86-96.
- 109 Huang K, Zhao Q, Li Y, Marthinsen K. Two-stage annealing of a cold-rolled Al–Mn–Fe–Si alloy with different microchemistry states. *J. Mat. Proc. Tech.* 2015;221:87-99.
- 110 Rozenak P. Lattice distortion formations by low-energy Ar<sup>+</sup> bombardment of thin silicon films grown on Silicon. *Metall. Mater. Trans. A.* 2011;42A:41-48.
- 111 Rajkumar KV, Rajaraman R, Kumar A, Amarendra G, Jayakumar T, Sundar CS, Raj B, Ray KK. Investigation of microstructural changes in M250 grade Maraging steel using positron annihilation. *Philos. Mag.* 2009;89:1597–1610.
- 112 Teng ZK, Ghosh G, Miller MK, Huang S, Clausen B, Brown DW, Liaw PK. Neutron-diffraction study and modeling of the lattice parameters of a NiAl-precipitate-strengthened Fe-based alloy. *Acta Mater.* 2012;60:5362–5369.
- 113 Kobayashi S, Takeda T, Nakai K, Hamada J, Kanno N, Sakamoto T. Effect of Nb addition on Cu precipitation in ferritic stainless steel. *ISIJ Intl.* 2011;51 :657–662.
- 114 Ghosh A, Mishra B, Das S, Chatterjee S. An ultra low carbon Cu bearing steel: influence of thermomechanical processing and aging heat treatment on structure and properties. *Mater. Sci. Eng., A.* 2004;374:43–55.
- 115 Takahashi J, Kawakami K, Kobayashi Y. Consideration of particle-strengthening mechanism of copper-precipitation-strengthened steels by atom probe tomography analysis. *Mater. Sci. Eng., A.* 2012;535:144–152.
- 116 Harry T, Bacon DJ. Computer simulation of the core structure of the screw dislocation in  $\alpha$ -iron containing copper precipitates: II. dislocation–precipitate interaction and the strengthening effect. *Acta Mater.* 2002;50:209-222.
- 117 Knipling KE, Karnesky RA, Lee CP, Dunand DC, Seidman DN. Precipitation evolution in Al–0.1Sc, Al–0.1Zr and Al–0.1Sc–0.1Zr (at.%) alloys during isochronal

- aging. *Acta Mater.* 2010;58 :5184–5195.
- 118 Gerold V. On calculations of the CRSS of alloys containing coherent precipitates. *Acta Metall.* 1968;16:823-827.
  - 119 Dieter GE. *Mechanical metallurgy (SI metric edition)*. McGraw-Hill Book Company; 1988.
  - 120 Kelly PM. The quantitative relationship between microstructure and properties in two-phase alloys. *Int. Metall. Rev.* 1973;18:31-36.
  - 121 Jiang Z, Lian J, Baudalet B. A dislocation density approximation for the flow stress-grain size relation of polycrystals. *Acta Metall. Mater.* 1995;43:3349-3360.
  - 122 Zener C. Theory of growth of spherical precipitates from solid solution. *J. Appl. Phys.* 1949;20:950-953.
  - 123 Mahadevan S, Manojkumar R, Jayakumar T, Das CR, Rao BPC. Precipitation induced changes in microstrain and its relation with hardness and tempering parameter in 17-4 PH stainless steel. *Metall. Mater. Trans. A.* 2016;47A:DOI: 10.1007/s11661-016-3440-8.
  - 124 Tabor D. The hardness of solids. *Rev. Phys. Technol.* 1970;1:145-179.
  - 125 Clerc DG, Ledbetter HM. Mechanical hardness: a semiempirical theory based on screened electrostatics and elastic shear. *J. Phys. Chem. Solids.* 1998;59:1071-1095.
  - 126 Morris JW. The influence of grain size on the mechanical properties of steel. <http://dx.doi.org/10.2172/861397>.
  - 127 Ungár T, Tichy G, Gubicza J, Hellmig RJ. Correlation between subgrains and coherently scattering domains. *Powder Diffr.* 2005;20:366-375.
  - 128 Hansen N. Hall–Petch relation and boundary strengthening. *Scripta Mater.* 2004;51:801-806.
  - 129 Takaki S. Review on the Hall-Petch relation in ferritic steel. *Mater. Sci. Forum.* 2010;654-656:11-16.
  - 130 Zhang X, Hansen N, Gao Y, Huang X. Hall-Petch and dislocation strengthening in graded nanostructured steel. *Acta Mater.* 2012;60:5933–5943.
  - 131 Balogh L, Figueiredo RB, Ungár T, Langdon TG. The contributions of grain size, dislocation density and twinning to the strength of a magnesium alloy processed by ECAP. *Mater. Sci. Eng., A.* 2010;528:533-538.
  - 132 Schmauder S, Kohler C. Atomistic simulations of solid solution strengthening of alpha-iron. *Comput. Mater. Sci.* 2011;50:1238-1243.
  - 133 Rajkumar KV, Vaidyanathan S, Kumar A, Jayakumar T, Raj B, Ray KK. Characterization of aging-induced microstructural changes in M250 maraging steel using magnetic parameters. *J. Magn. Magn. Mater.* 2007;312:359-365.
  - 134 Novelo-Peralta O, González G, Lara-Rodríguez GA. Characterization of precipitation in Al–Mg–Cu alloys by X-ray diffraction peak broadening analysis. *Mater. Charact.*

2008;59:773-780.

- 135 Williamson GK, Smallman RE. Dislocation densities in some annealed and cold-worked metals from measurements on the X-ray Debye-Scherrer spectrum. *Philos. Mag.* 1956;1:34-46.
- 136 Pal H, Chanda A, De M. Characterisation of microstructure of isothermal martensite in Fe–23Ni–3.8Mn by Rietveld method. *J. Alloys Compd.* 1998;278:209–215.
- 137 Wilkens M. The determination of density and distribution of dislocations in deformed single crystals from broadening X-ray diffraction profiles. *Phys. Status Solidi A.* 1970;2:359-370.
- 138 Shin JH, Jeong J, Lee JW. Microstructural evolution and the variation of tensile behavior after aging heat treatment of precipitation hardened martensitic steel. *Mater. Charact.* 2015;99:230-237.
- 139 Viswanath A, Rao BPC, Mahadevan S, Jayakumar T, Raj B. Microstructural characterization of M250 grade maraging steel using nonlinear ultrasonic technique. *J. Mater. Sci.* 2010;45:6719–6726.
- 140 Hikata A, Chick BB, Elbaum C. Dislocation contribution to the second harmonic generation of ultrasonic waves. *J. Appl. Phys.* 1965;36:229-236.
- 141 Cantrell JH, Yost WT. Effect of precipitate coherency strains on acoustic harmonic generation. *J. Appl. Phys.* 1997;81:2957-2962.
- 142 Hurley DC, Blazar D, Purtscher PT, Hollman KW. Nonlinear ultrasonic parameter in quenched martensitic steels. *J. Appl. Phys.* 1998;83:4584-4588.
- 143 Garabagh MRM, Nedjad SH, Ahmadabadi MN. X-ray diffraction study on a nanostructured 18Ni maraging steel prepared by equal-channel angular pressing. *J Mater. Sci.* 2008;43:6840–6847.
- 144 Rothman RL, Cohen JB. X-Ray study of faulting in BCC metals and alloys. *J. Appl. Phys.* 1971;42:971-979.
- 145 Berkum JGMv, Vermeulen AC, Delhez R, Keijser HD, Mittemeijer EJ. Applicabilities of the Warren-Averbach analysis and an alternative analysis for separation of size and strain broadening. *J. Appl. Cryst.* 1994;27:345-357.
- 146 Sinha PP, Sivakumar D, Babu NS, Tharian KT, Natarajan A. Austenite reversion in 18 Ni Co-free maraging steel. *Steel Res.* 1995;66:490-494.
- 147 Hirano K, Cohen M, Averbach BL. Diffusion of Nickel into iron. *Acta Metall.* 1961;9:440-445.
- 148 He Y, Yang K, Sha W. Microstructure and mechanical properties of a 2000 MPa grade Co-free maraging steel after aging at 753 K. *Metall. Mat. Trans. A.* 2004;35A:2747-2755.
- 149 Pereloma EV, Shekhter A, Miller MK, Ringer SP. Ageing behaviour of an Fe–20Ni–1.8Mn–1.6Ti–0.59Al (wt%) maraging alloy: clustering, precipitation and hardening. *Acta Mater.* 2004;52:5589-5602.

- 150 Ardell AJ. Precipitation hardening. *Metall. Trans. A*. 1985;16A:2131-2165.
- 151 Rajkumar KV, Kumar A, Jayakumar T, Raj B, Ray KK. Comprehensive evaluation of ageing behaviour in M250 grade maraging steel using nondestructive parameters. *Mater. Eval.* 2010;68:69-75.
- 152 Ledbetter HM, Austin MW. Elastic constant versus temperature behavior of three hardened maraging steels. *Mater. Sci. Eng.* 1985;72:65-69.
- 153 Cao Y, Zhu J, Liu Y, Lai Z, Nong Z. First-principles studies of the structural, elastic, electronic and thermal properties of Ni<sub>3</sub>Ti. *Physica B*. 2013;412 :45–49.
- 154 Prikhodko SV, Isaak DG, Carnes JD, Moser S, Ma Y, Ardell AJ. Elastic constants of face-centered cubic and L12 Ni-Si alloys: composition and temperature dependence. *Metall. Mater. Trans. A*. 2003;34A:1863-68.
- 155 Chaturvedi MC, Lloyd DJ, Chung DW. Yielding behaviour of g' precipitation strengthened Co-Ni-Cr superalloys. *Metal Sci. J.* 1976;10:373.
- 156 Nunomura Y, Kaneno Y, Tsuda H, Takasugi T. Phase relation and microstructure in multi-phase intermetallic alloys based on Ni<sub>3</sub>Al–Ni<sub>3</sub>Ti–Ni<sub>3</sub>V pseudo-ternary alloy system. *Intermetallics*. 2004;12 :389–399.
- 157 Thompson AW, Brooks JA. The mechanism of precipitation strengthening in an iron-base superalloy. *Acta. Metall.* 1982;30:2197-2203.